Electrical impedance tomography: methods and applications

Duan, Xi

Award date:
2020

Awarding institution:
University of Bath

Electrical impedance tomography: methods and applications

submitted by

Xi Duan

for the degree of Doctor of Philosophy

of the

University of Bath

Department of Electronic and Electrical Engineering

Bath, Jan 2020

Declaration

I declare that I have read and understood the entry in the Student Handbook for the Department of Electronic and Electrical Engineering on Cheating and Plagiarism and that all material in this thesis is my own work, except where I have indicated with appropriate references. It is being submitted for in fulfilment of the requirements of the degree of Doctor of Philosophy in Electronic and Electrical Engineering. No portion of the work in this document has been submitted before for any degree or examination at any other university.

Signature of Author.....

Date.....

Abstract

Electrical impedance tomography (EIT) is an imaging technique for mapping the internal conductivity distribution of an object by taking voltage measurements from electrodes attached to the surface of the object, while an electrical current is injected to these boundary electrodes. EIT has been researched in many different application areas in the world as a simpler, cheaper and safer alternative to many other tomography techniques, while provider very useful and often unique functional information. The main aim of this PhD study is to extend the use of EIT by further improvements of our understanding of the EIT data and image analysis and its challenges. In each case the challenges are highlighted and some solutions are proposed.

EIT has great applications in area of industrial processes. We highlight a challenges associated with the EIT to simultaneously reconstruct the permittivity and conductivity, in particular, when there is a low contrast in permittivity values of samples but in high contrast with background. A good case study to highlight this challenge is a water dominate oil and gas flow with important application in process industry. The thesis is proposing a dual-modality EIT with transmission mode travel time ultrasound tomography for such an application.

Another potential area with the EIT is the use of EIT for artificial skin for robotics application. This is done using a soft material such as fabric and the skin can be developed by EIT with sensing the change in conductivity while pressure applied to the skin. We have identified two main issues with the application, one the need to extend the functionality of the skin to be dynamical. This will enable the EIT based skin to work as an interface allowing social interaction with the robot. Second is a well established issue in medical EIT, which also exists in robotics

EIT and that is the movement of electrodes which corrupted the EIT image. We have developed a spatially correlated total variation imaging algorithm so that the robot skin using EIT could work as dynamical imaging sensor allowing for interactive skin. The interaction of the EIT based skin through pressure sensing can be done like a movie rather than individual images, which resembles the human skin interaction. The movement of electrodes and electromechnaicl interpretation of pressure via EIT image are both very difficult problems to model and interpreter. For these issue we implemented a convolutional neural network deep learning algorithm. The imaging results shows very good performance of both spatially correlated TV algorithm together with the deep learning approach.

The working flow of this dissertation can be explained as the following sections. Firstly, the basic background of EIT, its applications and mathematical theories including the forward problem, inverse problem have been reviewed. Secondly, a complex impedance image reconstruction is developed. The complex EIT which is determining conductivity and permittivity distribution at the same time using the real and imaginary part of the voltage measurements are presented. A complex-valued forward model, Jacobian matrix, inverse solution and related simulation studies are developed as well, the results indicated there are still challenging in reconstructing both parameters simultaneously. And then, a novel EIT combined with ultrasound transmission mode tomography (UTT) dual-modality for three-phase material image is developed. Identification of three phase oil/gas/water in water dominated situation should be possible via complex EIT, but practicality this is challenging. Therefore, the EIT/UTT dual modality imaging can be deployed for such application, where EIT is used to identify non-conductive phase which either oil or gas phase and hence UTT is used to identify air phase. Both simulation and experimental studies are implemented and a image fusion method is proposed for producing three-phase images. Finally, a conductive fabric based EIT dynamical sensing system integrated with deep learning for improving image quality is proposed, a movie like denoised experimental results are presented using a spatiotemporal total variation algorithm and a convolutional neural network training. The deep learning method helps overcoming the imaging artefact's due to electrode movement which is a main issue in fabric based EIT.

Acknowledgements

I DEDICATED THIS THESIS TO MY LOVELY FAMILY

Foremost, I would like to express my sincere gratitude to my supervisor Prof. Manuchehr Soleimani for the continuous support of my PhD study and research, for his patience, motivation, enthusiasm and immense knowledge. His guidance helped me in all the time of the research and writing of this thesis. I could not have imagined having a better advisor and mentor for my PhD study.

Secondly I would like to thank my family for their infinite encouragement and support especially my parents and my husband. Thanks for their understanding and endless love.

Last but not the least, I would like to thank my group mates and my friends, for many scientific and non-scientific support during my journey.

LOVE PEACE

List of Figures

List of Tables

List of Symbols

Electrical impedance tomography

E – electric field (V/m)
ρ – electric charge density (Cm^{-3})
ε_0 – permittivity of free space (F/m)
ε – relative permittivity
B – magnetic flux density (T)
H – magnetic field intensity (A/m)
J – electric current density (Am^{-2})
J_c – electric current density of conduction (Am^{-2})
J_s – electric current density of source (Am^{-2})
D – electric displacement (m)
σ – conductivity (S/m)
γ – admittance (S)
u – electric potential (V)
V – voltage measurement (V)
V_R – real part of voltage measurement (V)
V_I – imaginary part of voltage measurement (V)
I – current (A)
Z – contact impedance (Ω)
J – Jacobian matrix
A – area (m^2)
ω – angular frequency (Hz)
f – frequency (Hz)

Ultrasound transmission tomography

S– computed average sound velocity (m/s)
D – distance (m)
V_m – sound speed (m/s)
v – measured sound speed (m/s)

Abbreviation

EIT – Electrical impedance tomography
ECT – Electrical capacitance tomography
MIT – Magnetic inductance tomography
MRI – Magnetic resonance imaging
TV – Total variation
FEM – the Finite element method
UTT – Ultrasound transmission tomography
GVF – Gas volume fraction
WLR – Water-to-liquid ratio
CT – Computed tomography
FPGA – Field programmable gate array
CNT – Integrated carbon nanotube
TFC – Technology foresight challenge
TUV NEL – National engineering laboratory Flow measurement
ERT – Electrical resistance tomography
ROI –Region of interest
CBCT – Cone beam computed tomography
THRs – Total hip replacements
CGLS – Conjugate gradient least squares
URT – Ultrasound reflection tomography
CEM – Complete electrode model
SVD – Singular value decomposition
BV – Bounded variation
PDIPM – Primal and dual interior point method
LBP – Linear back-projection

SB – Split Bregman method
ST-TV – Spatiotemporal total variation
AR – Amplitude ration
PE – Position error
RES – Resolution
SD – Shape deformation
CoG – Centre of gravity
TOF – Time-of-flight
MSE – Mean squared error

Contents

Chapter 1

Introduction

1.1 Background

Tomography is known as an imaging technique for mapping a cross-section in 2D or entire region in 3D of the object of interest, which applied for various aspects of science such as medicine, industry and geophysical applications. Tomography can be divided into 'hard field tomography' and 'soft field tomography'. Some well-known and mature imaging techniques such as $x-ray$ and $\gamma-ray$ tomography are classified as 'hard field tomography' whose transmitting signal follows a straight line pattern. They are fast and has been widely used in the medical field however the cost of such equipment is normally expensive and the radiation could be harmful to human body especially under long-term exposure.

The 'soft field tomography', mainly including electrical impedance tomography (EIT), electrical capacitance tomography (ECT) and magnetic inductance tomography (MIT), has also been used in medical and industrial fields. The different between 'hard' and 'soft field tomography' is that the transmitting signal of 'soft filed tomography' does not follow the straight line anymore and the signal distribution depends on the electrical excitation sources. The complex nature of electrical and magnetic field could bring a great difficulty in image reconstruction comparing to 'hard field tomography', but they can still benefit from the low capital cast, non-invasive and high speed [1].

EIT as a 'soft field tomography' measures the conductivity distribution of the region of interest. The region of interest normally should be conductive that allows injected current conducted over entire region. Such a medium can be presented in variety of materials like human tissue, pipelines, and conductive fabric. In a current driving EIT system, the current is injected while the voltage is measured, opposite, the potential is injected with the current being measured in a voltage driving EIT system. The measured data is then being used for image reconstruction.

There are three main applications fields in EIT: medical, industrial and geophysical. As early in 1907, the direct current resistivity imaging was used in geophysical studies for locating conductive anomalies in Sweden [2]. The method is based on injecting current into one electrode pair and measuring potential on another electrode pair. To acquire more potential measurements, they had to move the measuring electrode pair by hand [3]. A few decades later, tomography rapidly improved with the great birth of PC which provides the functions of modelling for solving the forward and inverse problems, as well as making effective calculations. In the early 1980s, EIT mainly focused on the clinical applications like thorax and gastric function monitoring [4], [5]. More recent, people were trying to detect various diseases such as cerebral hemorrhage [6] and breast cancer [7], [8] using EIT since it is non-invasive, radiation-free and low cost.

EIT also contributes to industrial applications since late the 1980s; it can be used for flow monitoring, visualization and measuring purposes. Especially in the petroleum industry, EIT can be applied for two-phase flow that has impedance contract between the main fluid and the second phase fluid or component clusters [9]. And for more complex flows such as oil-gas-water three-phase flow, they can be visualized and measured in most conditions using EIT involved dual-modalities [10], [11]. On the other hand, EIT based fabric sensors which can map local pressure were proposed in [12], [13] and [14], potentially became a good alternative artificial skin option, and benefit from light-weight, low-cost and stretchable.

1.2 EIT challenges

If we want to use EIT in real-life applications there are several critical challenges associated with it. This thesis aims to highlight a number of these challenges and provide some solutions or insights.

1.2.1 Complex EIT

In complex EIT, people trying to image the conductivity and permittivity distributions inside of human body at the same time using the real and imaginary part of voltage measurements since the biological tissues have different resistivity and permittivity response [15], [16], [17]. But in non-bio samples, there are only few researches considered the imaginary part of the admittance. Most of prior works are ERT which removes the effect of permittivity from measurements and models for simplicity.

In the most recent research [18], they present a simultaneous reconstruction for both conductivity and permittivity in three cases. However, the sample they used for showing conductivity changes also has the different permittivity setting, thus, the reconstruction images is confusing and couldn't determine the image reconstructed is due to the conductivity changes or permittivity changes. In other non-bio sample complex EIT research [19], the derivation of the Jacobian was wrong, the effect of frequency was not considered. The sensitivity matrix they used in image reconstruction was the Eidors default value which is not a complex-valued, and also the imaginary reconstruction images in different frequencies are confusing since there is no way to prove the changes in images are caused by the changes in permittivity or frequency. Therefore, further analysis of complex EIT for non-bio samples is needed with a proper mathematical modelling.

1.2.2 Water dominated three-phase imaging

In the oil and gas industry, companies are increasingly facing the need to find ways of improving oil and gas production techniques, establishing production facilities in a difficult location, reducing cost and transporting energy efficiently through pipelines. Clearly, to measure and visualise flow is one of the key developments in the petroleum industry [20]. Despite a long time research and development,

oil-gas-water three-phase flow is still a challenging problem. The complexity of measuring or visualization three-phase flow is mainly as follows: i) there are many characteristic parameters, gas-oil-ratio, water-cut, mass flow rate, slip velocity, etc [21]. ii) the gas volume fraction (GVF) and water-to-liquid ratio (WLR) change rapidly in the process of flow depending on the pressure and temperature. iii) the change of flow pattern is complex, there are more than 20 different flow regimes that have been observed [22], [23]. Açikgöz produced three-phase flow patterns for both oil-dominated and water-dominated conditions [24].

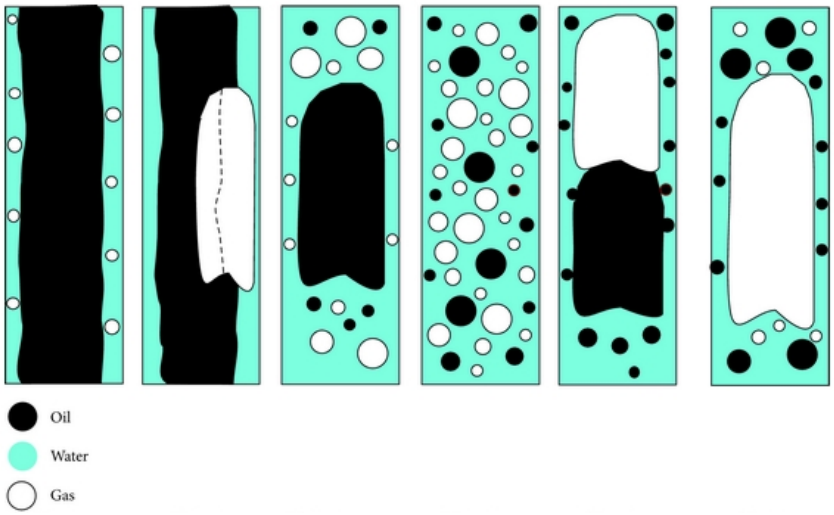

Figure 1-1: Flow patterns for vertical upward water-assisted with oil and gas flow [25]

As we all know, petroleum can be found in geological formations beneath the surface of the earth, surrounded by natural gas and often contain large amounts of water. Because water is more mobile than petroleum, some of the surrounding water is bound to be pumped up when crude oil and natural gas are produced through wells. That is a costly process and if it can be avoided by leaving the water at an earlier stage, it can make the processes more cost-effective. In addition, with the production of crude oil and natural gas, formation pressure gradually decreases. In order to maintain reservoir pressure and realize long-term high and stable production of the oil field, the development mode of formation water injection is widely used to improve oil recovery as in Fig 1-2. Therefore, in the early stage of oil field development, the water cut in crude oil is relatively low.

With the implementation of water injection scheme, a large amount of water is injected underground, and the water cut of crude oil will continue to rise, and the ratio of oil to water can reach more than 1:9. Therefore, the crude oil production often contains a lot of water [26].

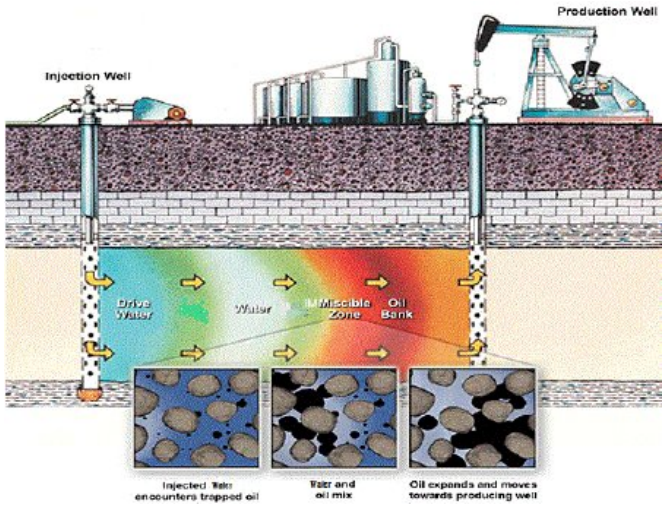

Figure 1-2: Water injection scheme during oil recovery [27]

EIT as an imaging technique, can visualise both interior conductivity and permittivity distribution inside the region of interest by only using measurements from electrodes placed on its boundary. It has been applied on the industry to identify gas and oil in water depending on their conductivity properties, currently it is a relatively mature technique in two-phase flow [9]. But three-phase is a more challenging task. In fact, a flow cannot be measured or visualised by a single tomography system; additional information is required in many industrial processes. The physical properties of each phase are listed in Table 1.1, bar plots clearly present the property difference between three phases. Conductivities states that there is in no separation for oil and gas in EIT since they are non-conductive. Tiny difference in relative permittivity of oil and gas suggests they can be distinguished by ECT theoretically with large precise computational calculation, but in real time, the separation can be extremely difficult. Depending on the different speed of sound, ultrasonic tomography seems can be used for three-phase flow, however, the contrast between water and oil is much smaller than them with air, measurement and reconstruction solution are not high enough

to meet the desired level. Therefore, single tomography systems are limited in oil-gas-water three-phase flow.

Table 1.1: Physical properties in room temperature (25° C) and bar plot of water, oil and gas

	Water	Oil(petroleum)	Gas(air)
Conductivity (mS/m)	35	0	0
Relative permittivity (ε)	80	2	1
Speed of sound (m/s)	1480	1290	343

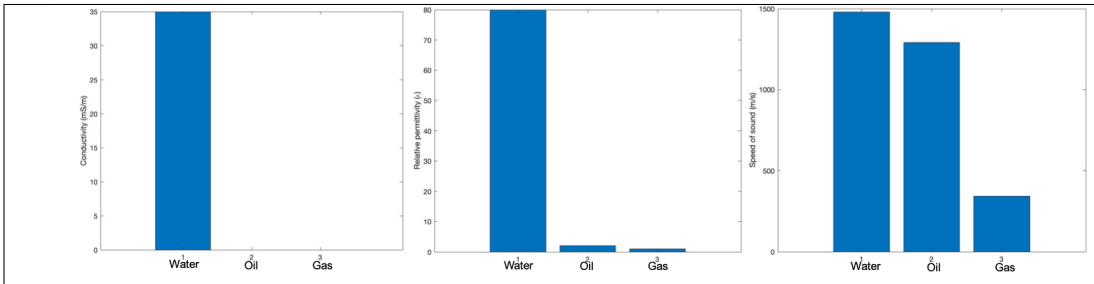

Conductivity, relative permittivity and speed of sound difference of three phases

To address as more three-phase flow patterns as possible, measuring/imaging more than two phases and flow monitoring purpose, various tomographic methods have been commercially applied and scientifically proposed for developing three-phase flow in the past few decades [20]. So far, dual-modality of electrical capacitance tomography (ECT) and electrical resistance tomography (ERT) is commonly used as a solution [28], [29], [30]. ERT can distinguish gas and oil (none or low conductivity) from water-dominated mixture (higher conductivity); meanwhile ECT can distinguish water (high permittivity) from gas-oil-dominated mixture (lower permittivity). In [31], dual-modality ECT and magnetic inductance tomography (MIT) was proposed, and successfully identified water and oil in air (simulated gas-dominated situation). Other modalities, such as combination of ECT and gamma-ray tomography was introduced in [32]. Gamma-ray tomography can distinguish gas from liquid, since these have different photon attenuation coefficients, which is closely proportional to the density of the flow. As a result, water and gas phases can be identified in oil-dominated flow. There is a growing interest in dual modality ultrasound (UT) and electrical tomography

since its original introduction in 2006 [33]. Yunus presented a simulation study on air-bubble detection using ERT UT dual-modality [34], and oil-water two phase flow was measured by Tan using UT and a conductance/ capacitance sensor [35]. Figure 1-3 presents a summary of current capability of dual-modalities in gas-oil-water three-phase flow against water to liquid ratio. However, all modalities can hardly distinguish oil and gas from water-dominated flow at the same time, leaving this situation as a blank space.

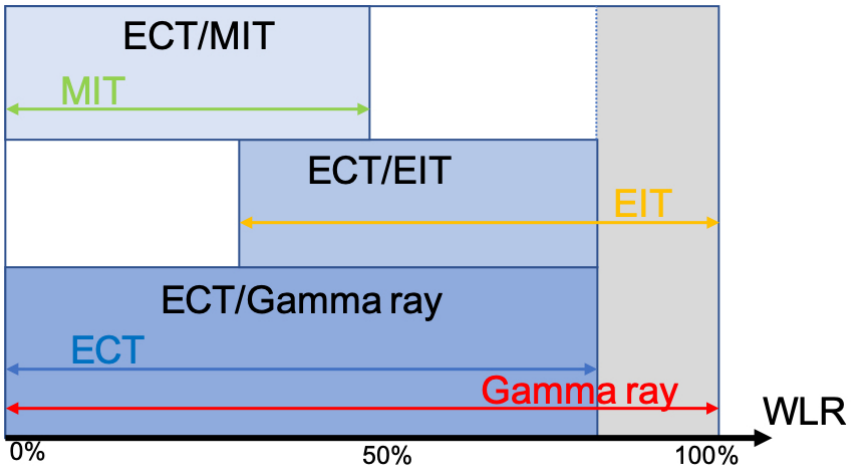

Figure 1-3: Capability of dual-modalities against WLR

1.2.3 Dynamical fabric EIT

Over the last two decades, there are various types of artificial skin based on different touch sensing techniques have been developed [36]. The piezoresistive sensor measures the resistance changes of the elastomer, foam, conductive carbon ink or other conductive material while the pressure force applied directly [37], [38]. This well-structured touch sensor is commonly used on robotic hands, gives high resolution and low cost [39], [40]. However, the high power consumption, low repeatability, and large hysteresis are some of the drawbacks of piezoresistive sensors. At the same time, capacitive sensors have been widely used in robotic since they have relatively high sensitivity and can give good spatial resolution, but the structure of the sensors is more complicated due to its sandwich design and the capacitors arrays, which easily causes noise and interference [41]. Optoelectronic sensors use optical technology, and the pressure can be detected by changes in

light intensity or spectrum. It has the advantages of large sensing range, high spatial resolution, immune to electromagnetic interference and fast response, but they are huge in size, required high power supply [42], [43]. Other tactile sensors using magnetic, piezoelectric, and ultrasonic are introduced and summarised in [39] and [44].

EIT as an imaging technique, the utilization of it have been successfully in biomedical, geophysical and industrial fields, it has been used for such as the brain and thorax monitor, liquid mixing and flow analysis because of the non-destructive property. Instead of the human body or other target, if a conductive material that will respond to local conductivity of permittivity changes is used, a pressure mapping imaging system or a touch sensing sensor can be created. Commonly, a large-scaled sensor array for robotic skin consists of numbers of interior wires or electrodes, which can easily cause electromagnetic noise and affect on the flexibility and stretchability of the skin. Where, the EIT based fabric sensor were introduced to overcome this issue. The first tactile sensor based on EIT without wire and sensing elements in its region was presented in [12], the rubber response to pressures with local changes in conductivity. To realise the light-weight, low-cost and stretchable artificial skin, single-layered conductive fabrics were used in [13] and [14] and a highly stretchable tactile distribution sensor was used for smooth-surfaced humanoids [45]. A tactile distribution sensor which enables stable measurement under high and dynamic stretch was also proposed in [46]. They demonstrated an improved EIT-based fabric sensor which can map local pressure.

However, the image resolution of fabric EIT is still experiencing a low quality problem. Since the beginning of EIT research, it is known that the shape mismatch and electrode position uncertainty are key sources of errors in imaging reconstruction [47]. In the most industrial applications and phantom simulations, the electrodes are stably mounted around boundary, reconstruction for these cases will not affected by the movement of electrode. However, in fabric EIT, the natural of fabric causes the shape mismatch when pressure applied.The arrows in Figure 1-4 indicated each electrode's movement. In the image of phantom data (a), there is no electrode movement which gives a fairy good reconstruction result. For the fabric data, reconstructed images are damaged by the noise caused

by electrode movement. The closer of the pressure point is to the boundary, the more the electrode will be affected around pressure point, the greater amplitude of the movement by these electrodes gives more collapse in image reconstruction. Also, the area around pressure point are blurred due to the net structure of the fabric, especially when there are more than one pressure points, the separation can be difficult like shown in Figure 1-4 (d). In addition, when pressure point is in central area, the reconstruction is challenging due to lower EIT sensitivity, but has potentially less effect on electrode movement. Same thing happens in medical EIT when trying to image the thorax, electrodes move with people breath, resulting a vague image.

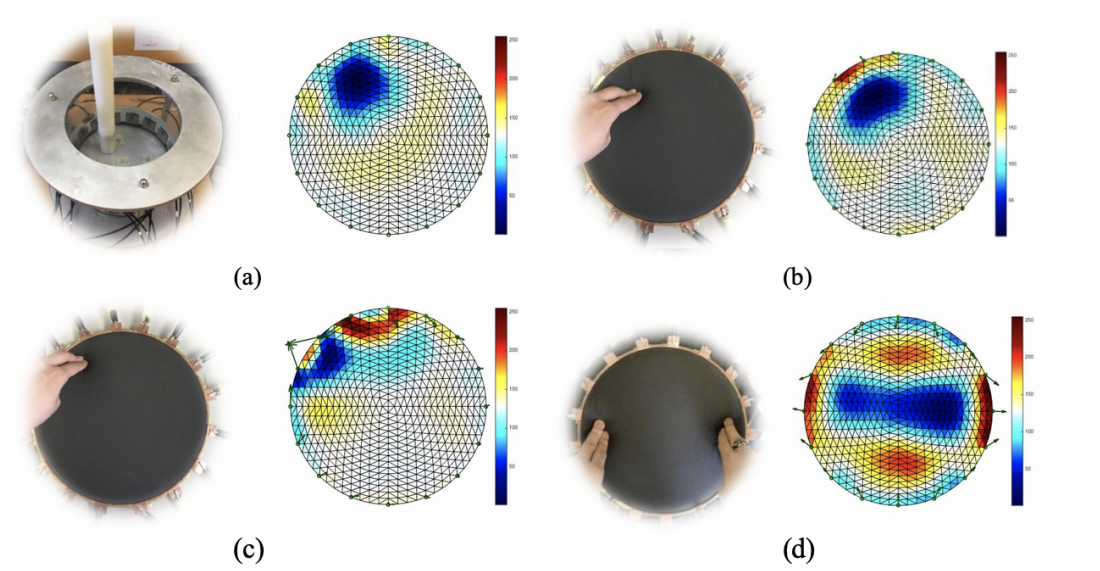

Figure 1-4: Top: reconstructed images for (a) phantom data with one non-conductive inclusion and (b) fabric data with one pressure point in top left. Bottom: reconstructed images for fabric data with (c) one pressure point close to boundary and (d) two pressure points.

There is no way to change the elastic structure of the fabric, and this is a great advantage in applications such as artificial skin and wearable monitoring. Therefore, implies post image processing is necessary to improve image quality and visibility caused by these inevitable physical phenomena.

1.3 Aim and objectives

The project aims to expand the feasibility of potential future applications of EIT. EIT is a new emerging tomography method that has been investigated for few decades. Although EIT suffers from low spatial resolution, it can still be applied for some monitor applications in clinical and process industry which does not require precise detection. Based on the challenges of EIT addressed above, there are three main objectives in this work.

- Based on the previous study by Yang [19] in complex fabric EIT, the appropriate mathematical modelling and sensitivity matrix should be obtained, then the proper conductivity and permittivity distributions should be determined. Further to achieve the purpose of using this complex EIT system for conductivity and permittivity imaging at the same time.

- Combining EIT with other tomography technique to create a novel dual-modality which can be used in solving the material distinguish problem in water dominated three-phase flow.

- To achieve dynamical imaging in fabric EIT, and eliminate the noise in reconstruction images. Which can be used for possible pressure mapping and robotic skin applications.

To achieve these objectives, several small tasks have been listed:

- Gain background knowledge of electrical impedance tomography and its practical applications in different fields. Investigate the current multi-modalities which involving EIT and its applications.

- Reviewing of the literature of EIT. Understand the basic mathematical formulation in EIT, including the forward problem, different image reconstruction algorithms in inverse problem especially the temporal TV algorithm. And the reconstruction method for dynamical electromechanical process.

- Develop several forward modeling and image reconstruction code, and improve lab skills which implement both simulation and experimental studies for different applications of EIT.

- Establishing the complex valued EIT modelling and the simulation studies.
- Establishing the dual-modality system, evaluating the performance of this system and investigating the feasibility of this system in water dominated three-phase distinguish by simulation and experiments.
- Implement laboratorial evaluation of EIT-based conductive fabric sensor and learn the basic knowledge of deep learning which can be used for improvement of image quality.

1.4 Thesis organization

This thesis has been divided into eight chapters that allowed readers to gain a better understanding of the project:

- **Chapter 1**: Introduction chapter regarding the background, objectives and the thesis structure to guide the reader gaining a clear picture of this thesis.
- **Chapter 2**: Introduction of the earlier EIT history and its development. Followed by the summarise of the evolution of EIT hardware systems depending on their current source. And the EIT applications are briefly described in the last section.
- **Chapter 3**: The basic theory of EIT is presented in this chapter. The most commonly used EIT current patterns are studied. The mathematical set-up of EIT and the boundary conditions are discussed. The FEM formulation is studied for solving forward problem and two different methods of driving Jacobian are introduced. Then, the inverse problem is illustrated where some algorithms of image reconstructions are reviewed including LBP, Tikhonov, SVD and ST-TV. Finally, the parameters for image quality are introduced.
- **Chapter 4**: A complex EIT with proper mathematical modelling is developed in this chapter. Complex admittance data for simultaneous reconstruction of both conductivity and permittivity is studied. A new method of deriving the complex-valued Jacobian matrix is created. The reconstruction images for different conductivity, permittivity and frequency are simulated and studied in three designed scenarios. Results show some good achieve-

ment but also indicated the difficulties of permittivity reconstruction in all cases.

- **Chapter 5**: A novel dual-modality including EIT and ultrasound transmission tomography (UTT) for imaging three-phase material is presented in this chapter. The concept is demonstrated using a simulation study and then shown with experimental lab tests using the system combining a 32-electrode EIT sensor array and a 32-transducer UTT sensor array. Five different three-phase flow scenarios are established in the lab, and the results show successful distinguishably for all three phases. This work has been published in [48].

- **Chapter 6**: A spatio-temporal based EIT imaging on a conductive fabric for pressure mapping or touch sensing with the aid of deep learning for denoising is developed in this chapter. Two set of dynamical experiments are carried out, and the results demonstrated the successful outcome by a combined deep learning with dynamical EIT imaging results in single and multiple points of touch. This work has been published in [49].

- **Chapter 7**: Conclusion and future work of three main outcomes on complex EIT, EIT dual-modality in three-phase material imaging and dynamical fabric EIT with deep learning.

Chapter 2

EIT applications

EIT is an imaging technique that can show the conductivity or permittivity map of an object. All measurements are taken from a number of electrodes set at the boundary of the object as voltage values, while a certain current pattern is injected into the object. The current flows through the object, and it changes direction when meets inclusion which has different conductivity. EIT problems include computational problems of image reconstruction, instrumentation, sensors design, data interpretation and applications. A simplified block diagram of an EIT system is shown in Figure 2-1, including a power resource to generate current, a multiplexer for switching the current injector and voltmeter among the different channels, a voltmeter for voltage measurement and a A/D for converting to digital signal to PC.

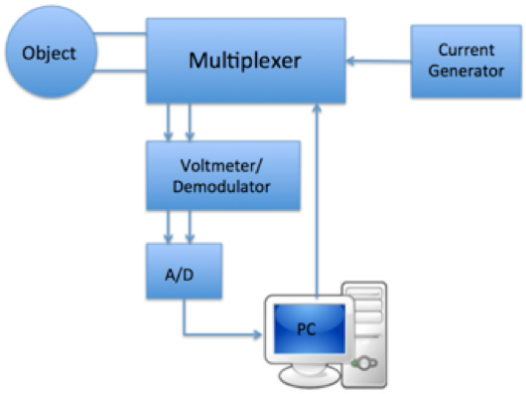

Figure 2-1: EIT system block diagram

2.1 Early medical EIT

In the 1980s, Electrical Impedance Tomography was known as a solution for in vivo images since the resistivity of different human tissue is various, and also called applied potential tomography [5]. During this period, researches around EIT was mainly focused on the medical field. The first impedance camera was built by RP Henderson and JG Webster in 1976, which produce a transmission image of the thorax. They used a single electrode on the front of the thorax and a 144 mutually guarding electrodes array on the back to produce 100 measurements [50], [51]. Later on, a 16 electrodes system was built to produce a tomographic image by Barber and Brown in 1987, it was a non-invasive system and the electrodes could attach to the human body directly.

Figure 2-2: A 16 electrodes system used for gastric imaging [4]

An alternating current of $1mA$ at $50kHz$ was injecting to an adjacent pair of electrodes while the potential measured at the remaining 13 pairs of electrodes [4], [5]. At the same year, Brown and Seagar published the first EIT hardware system called Sheffield data collection system [52]. It used 16 electrodes which addressed by 4 multiplexers and a drive current of 5mA at 51 kHz. A complete set data of 208 measurements collected in 79 ms.

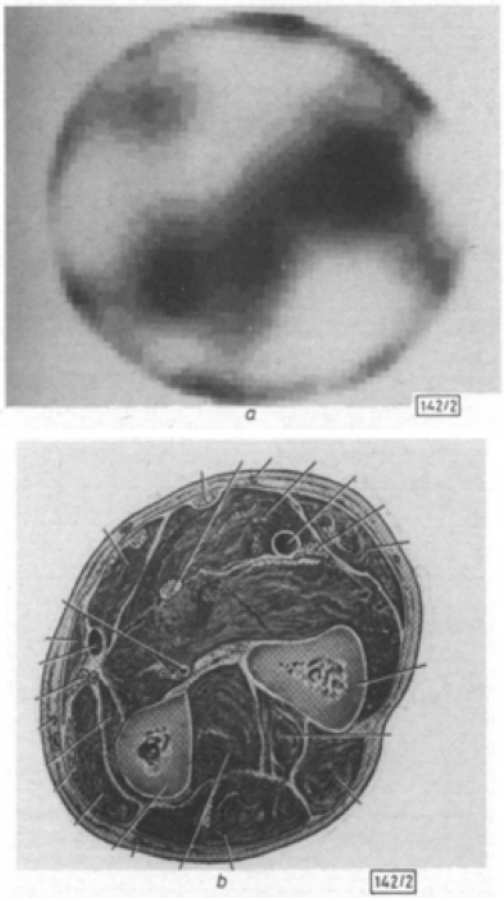

Figure 2-3: (a) Resistance image of a normal human forearm, darker indicated higher resistivity, (b) Cross-section image of a normal human forearm at the same level as in (a) [5].

Followed Barber and Brown, a large number of researches and studies on EIT were carried out. On one area, the poor spatial resolution of the image was been improve by development on the hardware design and computational image reconstructions. Multi-frequency EIT and parameterizations were introduced as a solution to increase the accuracy. Use a given set of measurements as a reference for all other measurements under different frequencies [53]. In the image reconstruction field, the back-projection[5], [54] and the sensitivity matrix are the most popular approaches. Cheney and Woo published the Newton- Raphson iterative method based on sensitivity matrix for solving the inverse problem in 1990 [55], [56]. Later on, Brown developed the Sheffield Mark 3 system, which can apply multi-frequency between 9.6 kHz to 1.2 MHz, based on his own previous

design [57].

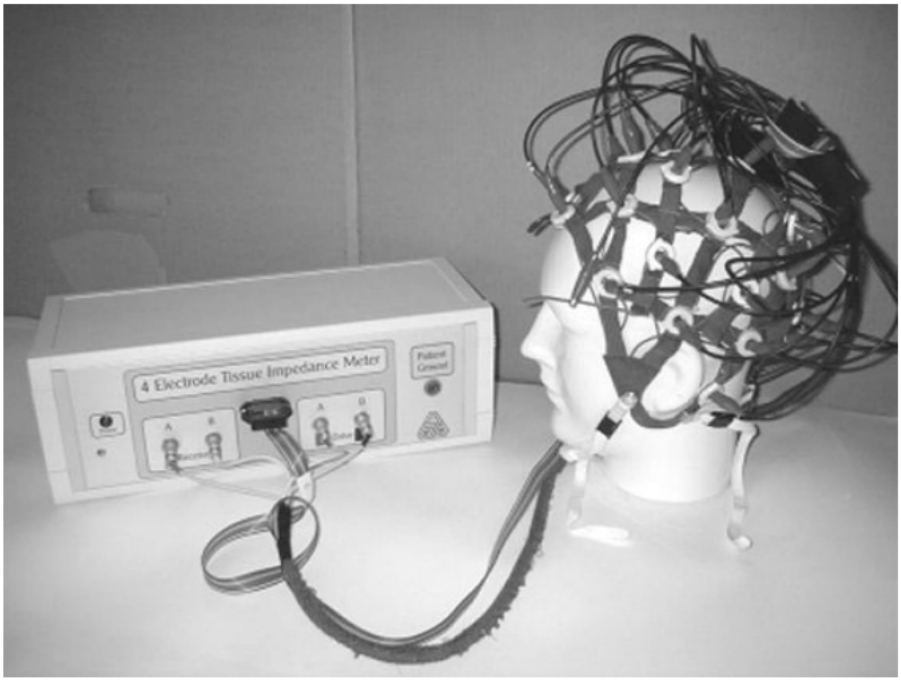

Figure 2-4: UCLH Mark 2 system designed to monitor stroke [58]

On the other area, the applications of EIT were implement to biomedicine, such as gastric function [59], [60], [61], pulmonary ventilation [62], [63], cardiac cycle [64], [65], [66], breast cancer [67], [68] and so on. A good review on EIT published by Boone in 1997 after three European Concerted Action programmes on Impedance Tomography from 1986 to 1997 [69].

2.2 EIT hardware system

So far, there are numerous EIT system designs for either researching proposes or commercial usage [70], [71]. They can be classified into two main types. The first type is injecting current to a pair of electrodes at a time from one current source. The second type uses multiple current sources, each current source is connected to a designed electrode and current injection is simultaneous to multiple electrodes.

2.2.1 Single current source systems

The first EIT system using a single current source was designed by Brown and Seagar in 1987 called Sheffield Mark 1 [52]. The system uses 16 electrodes which addressed through 4 multiplexers, a single operation frequency, one current source. Furthermore, both real and imaginary components of the measured voltage can be recorded. Several version of Sheffield systems were developed following Mark I, the latest Shellfield system Mark 3.5 uses only 8 electrodes with adjacent drive-and-receive combinations. The system is capable of measuring data at 30 frequencies between 2 kHz and 1.6 MHz at 25 frames per second [72]. University College London has been developing EIT systems for imaging the brain. The UCLH Mark 2.5 can operate in a wide frequency band up to 256 kHZ and the lowest frequency has been extended down to 20 Hz, as lower frequencies produce larger changes during brain activity, the pictures of the systems are shown in Figure 2-5 [73], [74], [75]. The other famous group who works on single current source EIT systems is Kyung Hee University. A 16-channel EIT system KHU Mark I was designed in 2007 [76]. The operational frequency expanded to between 10 Hz to 500 kHz. Later on, an updated version of KHU Mark II was created. New features include flexible electrode configurations to accommodate application-specific requirements, multiple independent current sources and voltmeters for fully parallel operations,improved data acquisition speeds for faster frame rates and compact mechanical design. Some of the experimental results in this thesis were produced by this system [77]. Table 2.1 provides a brief summary of these systems.

Table 2.1: A summary of single current source EIT systems

System	Time	Electrodes	Frequency	Technique
Sheffield MK1 [52]	1987	16	51 kHz	Analogue
Sheffield MK2 [78]	1990	16	20 kHz	Digital
Sheffield MK3 [53]	1994	16	9.6 kHz - 1.2 MHz	Analogue
Sheffield MK3.5 [72]	2001	8	2 kHz - 1.6 MHz	Digital
UCLH Mark 1a [73]	1999	16	225 Hz - 65 kHz	Digital
UCLH Mark 1b [74]	2002	up to 64	225 Hz - 77 kHz	Digital
UCLH Mark 2.5 [75]	2006	up to 64	20 Hz - 256 kHz	Digital
KHU Mark I [76]	2007	up to 64	10 Hz - 500 kHz	Digital
KHU Mark II [77]	2011	up to 64	10 Hz - 1 MHz	Digital

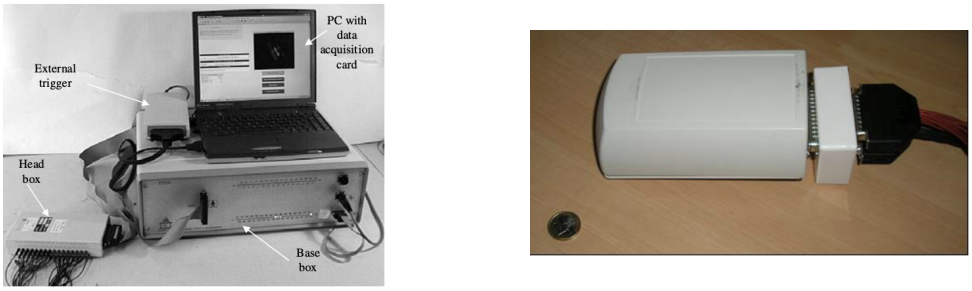

Figure 2-5: Photograph of the UCLH Mark 1b (left) [74] UCLH Mark 2.5 (right) [75] systems

2.2.2 Multiple current sources systems

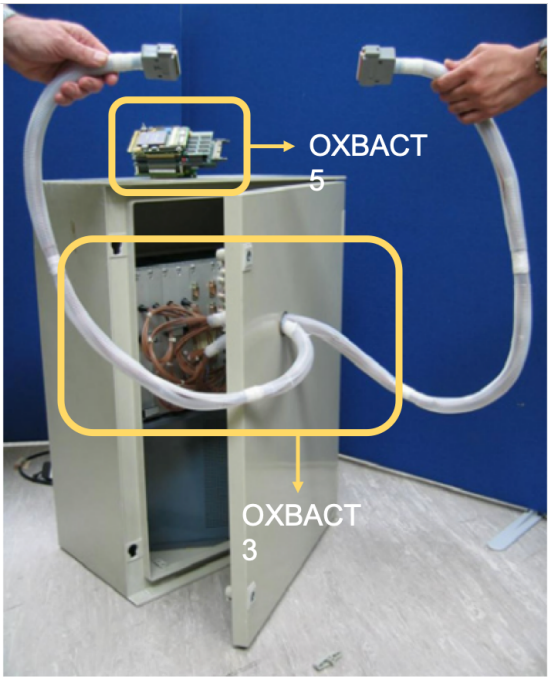

Figure 2-6: Photograph of the OXBACT systems

The most well known multi-source EIT system in early stage was OXPACT-II, it was built with voltage drivers and with measurement of both voltage and current at each electrode [79]. To overcome the low data acquisition speed and satisfy the need of clinical 'vivo study', OXBACT-III was created two years later. This system not only extended operational frequency, but also increased the speed of data collection which can be used for real-time clinical monitoring and measuremrnts [80]. The most recent Oxford system is OXBACT 5, as shown in the top of Figure 2-6, which is based on 16 current sources and 64 voltage measurements. They used FPGA (field programmable gate array) to reduce the system size and in the meantime to provide a better solution [81]. The Dartmouth group has been working on the breast imaging system, and their latest instrument was the first EIT system to be reported that is capable of imaging impedance distributions up to 10 MHz. The system is flexible allowing for high speed data collection from a four-plane electrode array configuration with 16 electrodes on each plane which can be used for providing 3D imaging [82], [83]. Other similar EIT systems are summarized in Table 2.2 with all multi-

source systems introduced above.

Table 2.2: A summary of multi-source EIT systems

System	Time	Electrodes	Frequency	Source
OXPACT II [79]	1992	32I+32V	9.6 kHz	Constant voltage
OXBACT III [80]	1994	32I+32V	10 - 160 kHz	Multi-voltage
OXBACT 5 [81]	2008	64	26 - 160 kHz	Multi-current
Dartmouth [83]	2008	64	10 kHz - 12.5 MHz	Voltage
ACT 3 [84]	1994	32	30 kHz	Multi-current
ACT 4 [85]	2007	72	300 Hz - 1 MHz	Multi-current/voltage

2.3 Further applications

The practical uses of EIT were most contributed to medical and clinical imaging in early times since EIT can image or monitor processes involving the movement of conductive fluids like blood and gases. Moreover, this modality is non-invasive, low cost, radiation-free and portable with relatively high temporal resolution. The book Clinical and Physiological Applications of Electrical Impedance Tomography was published in 1993 which contains major researches and outcomes in earlier EIT development [86]. More recent, medical EIT has also been actively investigated for pathological examination of maligant tumors like prostate [87] and breast cancer [88], [7], [8], nursing care of monitoring the bladder fullness [89], detecting acute cerebral stoke [6], imaging fast neuronal processing in the brain [90], etc..

In other fields, EIT also plays an important role, it has become a popular modality for nondestructive testing. In the process industry, EIT has been used for visualizing flows inside the pipes to achieve cost efficiency production since the conductivity is different for each phase [91], [11]. Similarly, reactor vessels can be monitored using electrical tomography in chemical engineering [92]. Several civil engineering applications and a number of research works have been reported such as detecting leaks from buried pipes [93], [94] and brick walls dampness testing [95], [96] as shown in Figure 2-7. Not like conventional EIT sensor, the sensor used for such applications was designed to be a linear electrode array. For dis-

tinguishing leaking pipes and intact pipes, [94] suggested the sensor array placed perpendicular to the axis of the pipe, both laboratory and field simulation was showing promising results. [93] was able to locate leak position down to 2 meters depth while the sensor array placed on the surface along the pipe. Moreover, the moisture inside walls was successfully imaged using EIT since the electrical resistance increases as the moisture content decreases. It is important for protecting and maintaining historical buildings with great architectural significance.

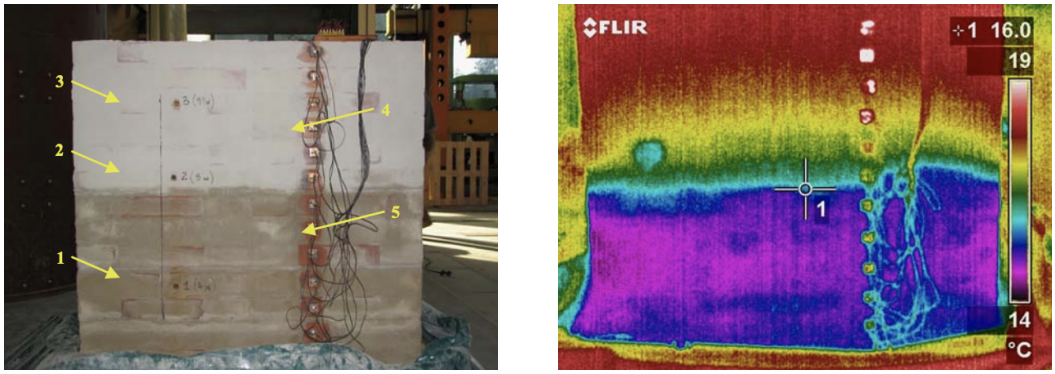

Figure 2-7: Dampness measurements of the wall using EIT [94]

Furthermore, sense of touch is a major part of human's communication with their environment, EIT as a pressure mapping system provides a low cost alternate solution for artificial sensitive robotic skin. The measurements are taken from the boundary of the conductive fabric and no needs of sensing elements inside the area. [45] created a sensor which made of two layers that combines a highly resistive conductive yarn on the top and a conductive sheet with low resistance on the bottom. Yao and Soleimani developed a prototype of EIT based single layer tactile fabric sensor in 2012. The experiments showed positive results of locating pressure on electro-conductive knitted fabrics using EIT [13]. For more precise applications, EIT integrated carbon nanotube (CNT) thin films was able to visualize the structural defects and responded to various pH environments, which potentially can be developed to the multi-functional CNT-based sensing skins [97].

2.4 Dual-modality EIT

Tomography is imaging any cross-section through the use of any kind of penetrating wave; the method is used widely in lots areas of science. The basic aim of tomography is to determine the distribution of materials in some region of interest by obtaining a set of measurements using sensors that are mounted around the periphery [98]. There are numbers of different types of tomography, Table 2.3 briefly summarised some common techniques and their source of data.

EIT as one of tomography modality which producing conductivity reconstruction has its own advantages of being non-invasive, low capital cost, radiation-free and portable. However, this modality does not have the capability to generate a high resolution image to meet certain high accuracy requirements. In general, almost all tomography modalities has both advantages and disadvantages, combining one modality with another is hence expected to cover the weaknesses of each other, also provides additional information that enhances a single system. Basically, single modality can only provide one physical property distribution, such as EIT is imaging conductivity and electrical capacitance tomography (ECT) is imaging permittivity. Sometimes different material has the same response to the same excitation, which leads to difficulties in identification. For example, in water-oil-air three phase flow, air and gas are both non-conductive, they will not be distinguished in an EIT image. Therefore, EIT combined with other tomography systems has been proposed in different applications for various purposes.

Table 2.3: list of common tomography techniques

Name	Reconstruction source	Data source	Applications
X-ray Computed tomography (CT)	X-ray	X-ray	Medical
Magnetic resonance imaging (MRI)	Magnetic field	Nuclear magnetic resonance	Medical
Ultrasound computer tomography	Time of flight (sound wave)	Ultrasound	Medical, industrial
Electrical capacitance tomography (ECT)	Permittivity	Capacitance	Industrial
Electrical impedance tomography (EIT)	Conductivity	Impedance	Medical, industrial
Magnetic induction tomography (MIT)	Conductivity	Magnetic induction	Industrial
Gamma ray emission tomography	Photon attenuation coefficients	Gamma ray	Nuclear industrial

Depending on the purposes, dual-modality involved with EIT can be concluded into two main categories: resolution improvement and complex inclusion imaging in industrial or biological processes. Most image resolution improvements are achieved by EIT combining with CT, for example to overcome the respiratory artefacts in lung image. More recently, the combination of EIT and UT is proposed to improve the speed and accuracy of image reconstruction. For inclusion imaging, specified dual-modalities are proposed depending on different applications. In this section, dual-modalities are introduced and summarised according to the tomography techniques.

2.4.1 EIT/ECT

Dual-modality, including EIT and ECT was first proposed by Technology Fore-

sight Challenge (TFC) research project for process tomography. A robust, reliable, industrialised and commercial instrument M3000 that supports dual-modal process tomography ERT and ECT was produced. Several experiments were carried out to verified that the sub-systems (an ERT sensor with16 electrodes and an ECT sensor with 12 electrodes) of this dual-modality could work contemporaneously, and oil-water-gas three-phase distribution can be imaged by data fusion [28]. Following, the system has been developed and been tested in the industrial-scale multi-phase flow facility at TUV NEL (National Engineering Laboratory Flow Measurement) [10]. The system is able to image oil-gas-water three-phase flow within the water to liquid ratio range between 40% to 90%. The ERT and ECT images were produced separately before applying to a pixel-by-pixel fusion algorithm.

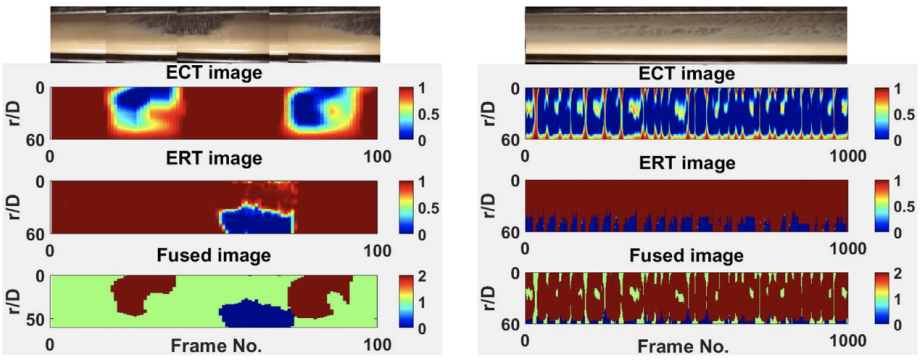

Figure 2-8: Visualisation of three-phase flow of 50% WLR in plug flow (left) and annular flow (right) [10]

For medical application, ECT/ERT dual-modality was proposed to provide real-time 3D images for revision total hip replacements (THRs) surgery in 2015. A single-plane ECT/ERT dual modality sensor was used in this study, with the prior knowledge, 2D cross-sectional images and 3D images of the femur and the drilling/milling tool was obtained. They simplified 3D imaging process to only estimate the cross-sectional position of the femoral bone and the drilling/milling tool, which showed a great potential of visualizing the surgery process using the ECT/ERT dual-modality [99].

2.4.2 EIT/CT

The EIT and Cone beam CT (CBCT) dual-modality of taking advantage of high temporal resolution of EIT and high spatial resolution of CBCT was proposed for lung image by Pengpan in 2010. As conventional medical diagnostic imaging, CBCT suffers from the respiratory artefacts, which makes the treatment planning inaccurate in lung cancer therapy. The simulation results successfully showed that the motion information extracted from EIT images can be used to compensate for the motion in CBCT images through their iterative image reconstruction for CBCT [100]. Further,a motion-compensated conjugate gradient least squares (CGLS) algorithm for CBCT was developed, they used the motion signal extracted from EIT images to compensate in CBCT image reconstruction which significantly reduced the motion artefacts in Figure 2-9 [101].

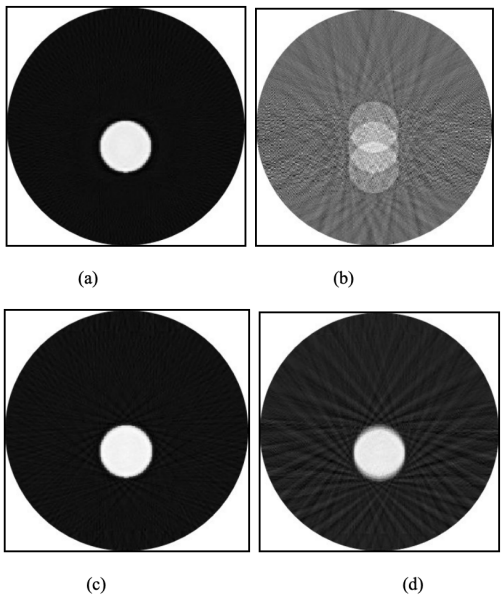

Figure 2-9: Simulation result of CBCT Images (a)no motion applied (b)60 mm peak-to-peak sinusoidal motion applied (c)motion compensation applied using true motion signal (d) motion compensation applied using motion signal extracted from EIT images [101]

In [102], Chen proposed an image fusion method to incorporate the EIT image with a CT slice. Experimental results verified that the proposed fusion method is feasible and the area where impedance changes exactly happene at the lungs

structural position. Later on, [103] demonstrated an EIT/CT fusion results using a biological Phantom with an improvement of detectability by 67% and structural similarity by 26%. To improve the potential utility of functional lung image in clinical applications, structural-functional lung imaging using a combined CT-EIT was proposed in 2016. A 'patient specific EIT imaging' superimposed with CT data to improve readability as shown in Figure 2-10 for clinicians using discrete cosine transformation reconstruction method was presented [104].

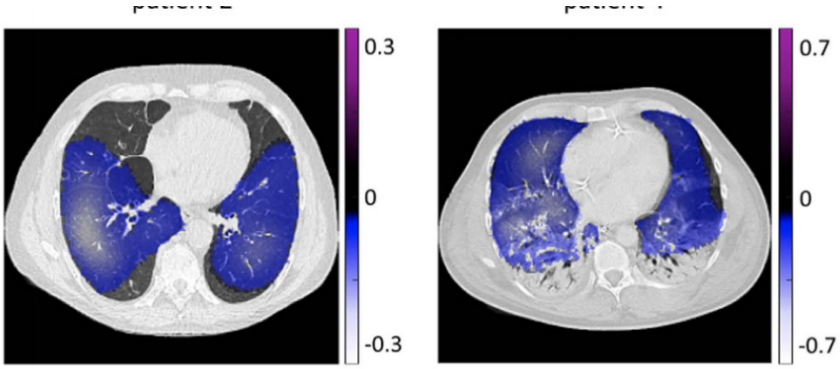

Figure 2-10: Superposition of changes in conductivity distribution (EIT images) and CT images in a patient with emphysema in the ventral lungs (left) and atelectasis in dorsal lungs (right) [104]

2.4.3 EIT/Ultrasound

The idea of EIT integrated with ultrasound was first proposed in [33], with the aid of ultrasound reflection signal measurement, the boundary reconstruction of the inclusion will be much sharper, the resolution of EIT images had been improved. Hence, this dual-modality revealed its potential in detecting small object such as breast tumours since the EIT is impedance-sensitive and ultrasound is boundary-sensitive [105], [106]. After that, a hybrid ultrasound ERT reconstruction method was developed in [107], which was using the result of ultrasound reflection tomography (URT) as a constrained term in ERT inverse problem. The results provided a significant enhancement in terms of spatial resolution and small lesions detection in simulation studies. Another approach of using ultrasound reflection results as a prior information to build non-uniform elements mesh in EIT reconstruction was proposed in [108], experimental results showed

an improvement in reducing spatial resolution from 3.9% to 2.4% for both linear and Newton-Raphson reconstruction methods.

More recently, Liang proposed a shape-based EIT and URT dual-modality imaging method, where some accurate boundaries information about the inclusions detected from URT are used to improve the speed and accuracy of EIT image reconstruction [109]. Soon, they developed a new dual-modality image reconstruction method, which background distribution determined by URT and UTT (ultrasound transmission tomography) is used as a hard constraint added into the EIT inverse problem through an equality constraint equation [110]. Both simulation and experimental results presented a better reconstruction performance with clearer targets edges and fewer artefacts in the background as shown in Figure 2-11.

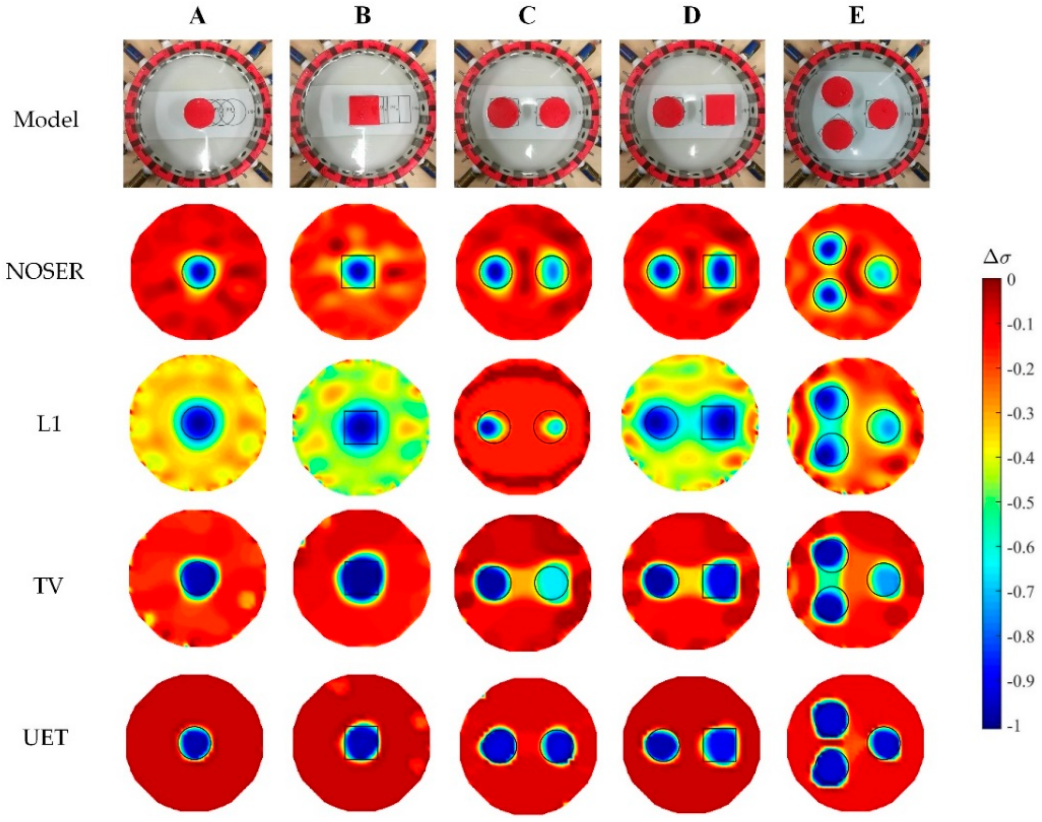

Figure 2-11: 5 experimental results using different reconstruction methods, UEIT is the proposed dual-modality method in [110]

In process tomography, [111] presented a simulation study using dual-modality of ERT and UTT to detect bubbles, they revealed possibilities of visualization bubble with a minimum radius of 5 mm located at the center of the acrylic vessel. And [35] proposed a method of combining ultrasonic transducer and electrical sensor to measure oil-water two phase flow. Based on the Doppler effect, the flow velocity is determined by ultrasonic transducers while the phase fraction is measured by the conductance/capacitance sensors.

Chapter 3

EIT principles

3.1 EIT data collection

In EIT, electrodes are attached on the boundary/surface of an object. In general, the conductivity is not directly measurable, but it can be calculated from boundary voltage measurements. For the same object, different current injection patterns give different voltage measurements. In general, they can be divided into two groups: optimal patterns and bipolar patterns [112]. Optimal patterns require more than one current sources that are simultaneously used for current injection to all electrodes while potential measurements are taken at all electrodes as well. It can produce better image reconstructions but also requires as many independent current sources as electrodes, which means more cost and complex instrument requirement. Bipolar patterns use only one current source and one independent current injector which is more practical in hardware built, injects to a single pair of electrodes at a time while the voltage measurements are taken at all other electrodes pairs. There are many ways to inject current. Three main methods are discussed below.

3.1.1 Adjacent method

The adjacent method is the most common injection patterns in EIT, it also called the neighboring method. In a 16-electrode EIT system, the first current injection

is applied to electrodes 1 and 2, while the voltage measurements are taken between electrodes 3 and 4, 4 and 5, and so on, but not in pair of electrodes 2 and 3, 16 and 1, like shown in Figure 3-1 (a) below. The second current injection is applied to adjacent electrodes 2 and 3. Moreover, the voltages are measured from the rest of 14 electrodes. Therefore, each current injection can give 13 different voltage measurements. The process is repeated until the current injected to all 16 adjacent electrodes, which will produce 16 x 13 = 208 measurements; only 104 are independent measurements.

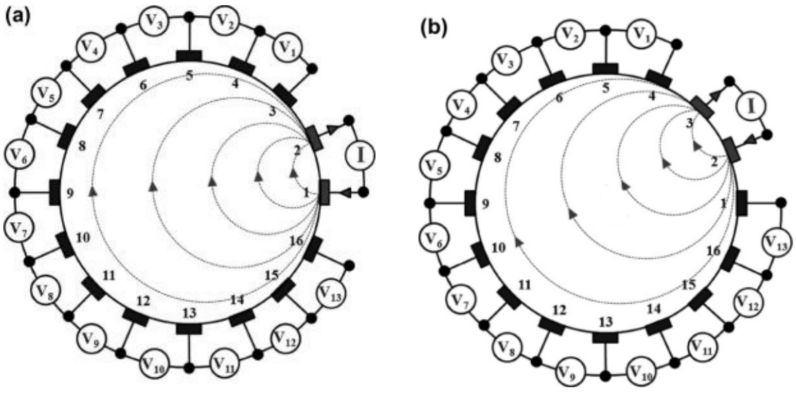

Figure 3-1: Adjacent current pattern (a) first injection (b) second injection [113]

In this method, the current density is highest between the injecting electrodes, and decreases rapidly as a function of distance. As a result, the sensitivity of conductivity is higher near to the boundary than the centre. The Figure 3-2 shows the simulation voltage measurements in one scan cycle.

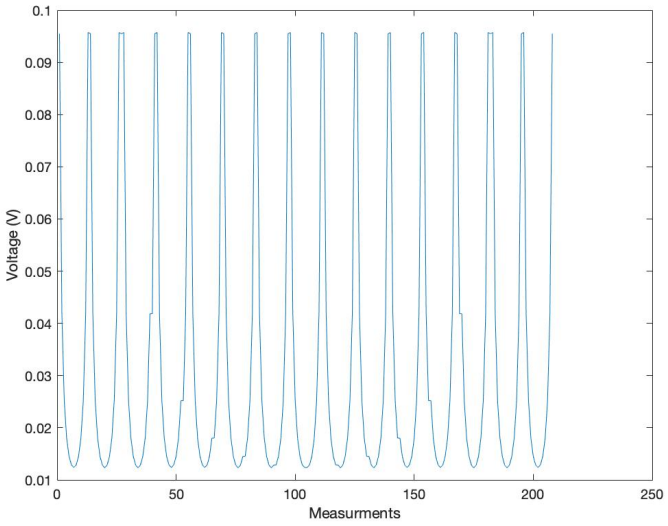

Figure 3-2: Voltage measurements simulation of the Adjacent current pattern

3.1.2 Opposite method

This opposite current method is commonly used in Brain EIT. The current applies to the electrodes that are 180 degree apart, while the voltage differences are measured on the remaining electrodes.

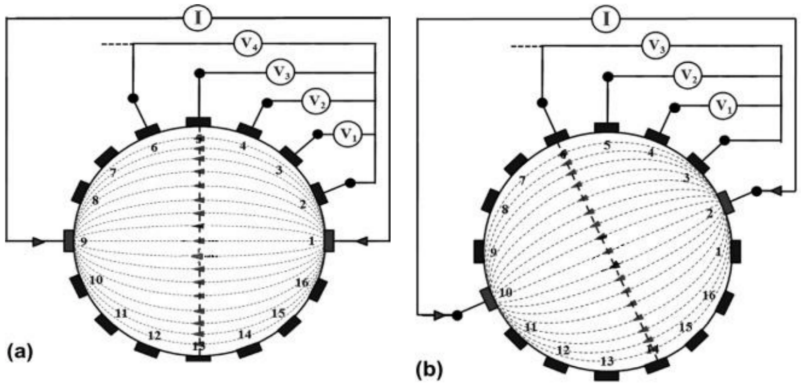

Figure 3-3: Opposite current pattern (a) first injection (b) second injection [113]

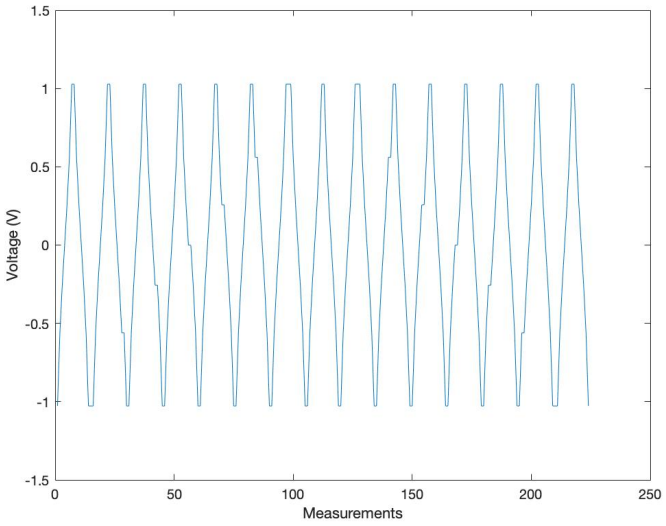

Figure 3-4: Voltage measurements simulation of the Opposite current pattern

In the first current injection of opposite method in a 16 electrodes EIT system, the current applies to electrodes 1 and 9 and the voltage differences are measured between all rest electrodes 2 and 3, 2 and 4 until 2 and 16, which gives 13 voltage measurements. The second injection through electrodes 2 and 10, and the same as the first injection, the voltage measured between electrode 3 and the rest. The whole process will finish when all 16 pairs of electrodes have been injected. Therefore in this method, 208 measurements will be provided after one complete scan, but only half of them are independent since the injection in electrodes 1, 9 gives the same measurements as the injection in electrodes 9, 1. Compare to the adjacent method, the opposite method produces less data but can provide a better distribution of the sensitivity in the centre of the object as the current travels through the object.

3.1.3 Cross method

This method is rarely used in EIT. The electrodes are selected as current and voltage references. The first injection applies to electrodes 16 and 2 as shown in the figure 3.11 below, which the electrode 16 is the current reference electrode, while the electrode 1 as the reference electrode to take voltage differences against the rest of 13 electrodes. And then the current injects to electrodes 16 and 4,

the voltage differences are measured as before. This should repeat for current injection between electrodes 16 and 6, 16 and 8, 16 and 10, 16 and 12, 16 and 14. Therefore the entire scan produces 7x13 = 91 measurements.

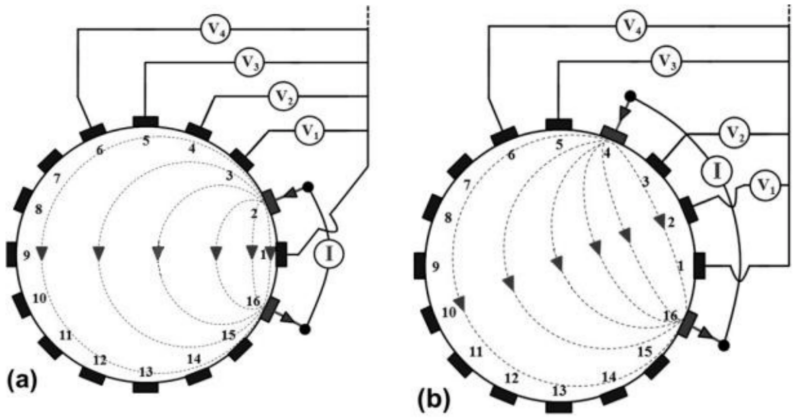

Figure 3-5: Cross current pattern (a) first injection (b) second injection [113]

Then, measurement is repeated with electrodes 3 and 2 as current and voltage reference respectively. The procedure is just repeated by connecting the positive current source to electrode 5, 7, 9, 11...1. Therefore another set of 91 measurements is made to make the total measurements 182. However, only 104 data sets are independent of each other.[114]

3.2 Forward problem

In general, there are two main problems in EIT image reconstruction, the Forward problem and the Inverse problem. The forward problem is to determine voltage distribution when the excitation current and conductivity are given under certain boundary conditions. Then the relationship between changes of voltages and changes of conductivity can be determined, which is the system matrix. Using the system matrix, the current applied and the measured voltage at the boundary to determine the real conductivity of the object is the Inverse problem.

3.2.1 Mathematical set-up of EIT and the boundary conditions

The problem of determining the voltage distribution of a known domain by applying a current and a specific conductivity is called Forward problem. The physical description of the propagation of the currents inside a known domain can be obtained from Maxwell's equations [115]. The Gauss's Law (first Maxwell's equation) states that:

$$\nabla \cdot E = \frac{\rho}{\varepsilon_0} \tag{3.1}$$

where E is the electric field, ρ is the electric charge density and the ε_0 is the permittivity of free space. Hence, the Faraday's Law of induction (second Maxwell's equation) states that the voltage accumulated around a closed circuit is proportional to the time rate of change of the magnetic flux it encloses,

$$\nabla \times E = -\frac{\partial B}{\partial t} \tag{3.2}$$

where B is the magnetic flux. Finally the Coulomb's law (fourth Maxwell's equation) shows that the currents and changes in electric fields are proportional to the magnetic field circulating about the area they pierce,

$$\nabla \times H = J + \frac{\partial D}{\partial t} \tag{3.3}$$

where H is the magnetic field, J is the electric current density and D is the electric displacement. The current density J is the sum of conduction current and source current, $J = J_c + J_s$, where $J_c = \sigma E$ and the J_s is typically zero because of the quasi-static approximation in EIT. Therefore the fourth Maxwell's equation can be rearranged as:

$$\nabla \times H = (\sigma E) + \frac{\partial(\varepsilon E)}{\partial t} \tag{3.4}$$

The electric field E is a complex vector function of space can written as $Re(E(x)e^{i\omega t})$. Furthermore, if the current is sinusoidal (time harmonic), E can be simplified as $Ee^{i\omega t}$. Then the previous equation now is:

$$\nabla \times H = (\sigma E) + \varepsilon i\omega E \tag{3.5}$$

$$\nabla \times H = (\sigma + i\omega\varepsilon)E \tag{3.6}$$

If the divergence of both sides is applied, then:

$$0 = \nabla \cdot ((\sigma + i\omega\varepsilon)E) \tag{3.7}$$

Since $\gamma = \sigma + i\omega\varepsilon$, the equation can be written as:

$$0 = \nabla \cdot (\gamma E) \tag{3.8}$$

and $E = -\nabla u$, where u is the scalar potential. Finally, the electric voltage (potential) in a given boundary conductivity in EIT is:

$$\nabla \cdot (\gamma \nabla u) = 0 \tag{3.9}$$

To solve an EIT problem, appropriate boundary conditions need to be enforced. Because the current injection and voltage measurements are all performed in the electrodes. This is where the Complete Electrode Model (CEM) should be introduced, which considers both the shunting effect of the electrodes and the contact impedance [116], [117]. The equation above describes the electric field inside of the domain Ω, the Neumann Boundary Condition describes how the voltages on the electrodes measured (Equation 3.11) and the Dirichlet Boundary condition describes the injected currents I_1 (Equation 3.12). Moreover, there is no current flow on the non-electrodes boundary (Equation 3.13). All of them can be expressed as:

$$\nabla \cdot (\gamma \nabla u) = 0 \qquad x \in \Omega \tag{3.10}$$

$$u + Z_l \gamma \frac{\partial u}{\partial n} = V_l \qquad x \in z_l, \quad l = 1, 2, 3 \dots L \tag{3.11}$$

$$\int_{e_l} \gamma \frac{\partial u}{\partial n} dS = I_l \qquad x \in e_l, \quad l = 1, 2, 3 \dots L \tag{3.12}$$

$$\gamma \frac{\partial u}{\partial n} = 0 \qquad x \in \partial\Omega \backslash \bigcup_{l=1}^{L} e_l \tag{3.13}$$

In order to make sure the existence and the uniqueness of the solution, two more conditions are applied:

i the law of the conservation of the charge: $\sum_{l=1}^{L} I_l = 0$

ii define a reference point: $\sum_{l=1}^{L} v_l = 0$

3.2.2 The Finite Element Method

The Finite Element Method is a numerical technique for solving practical differential equations [118], finite element meshing is utilized to discrete the domain and to calculate the voltage as a forward solver [119]. In EIT, the domain Ω is discretized into small triangular elements. The electric potential is expressed as a linear combination of nodal basis functions, the support of each nodal basis function is limited to the elements sharing a common node i. And we assume the value of 1 at the node i and they decay to 0 on each other nodes. Then the approximated potential is,

$$u = \sum_{i=1}^{N} u_i w_i \tag{3.14}$$

where w_i is the nodal basis functions, u_i is the nodal value assumed by the solution and the N is the number of the nodes. Since the nodal basis function is not differentiable equation (3.9) cannot be satisfied directly. Instead the weak form of the equation can be derived by multiplying some function v and integrating over Ω.

$$\int_{\Omega} v \nabla \cdot (\gamma \nabla u) dV = 0 \qquad in \Omega \tag{3.15}$$

Using Green's second identity and vector identity $\nabla \cdot (\psi A) = A \cdot \nabla \psi + \psi \nabla \cdot A$ the equation above can be derived to:

$$\int_{\Omega} \nabla \cdot (v \gamma \nabla u) dV - \int_{\Omega} \gamma \nabla u \cdot \nabla v dV = 0 \tag{3.16}$$

Apply divergence theorem($\int_{\Omega} \nabla \cdot F d\Omega = \oint F \hat{n} dS$),gives:

$$\int_{\Omega} \nabla \cdot (v \gamma \nabla u) dV = \int_{\partial \Omega} v \gamma \nabla u \cdot \hat{n} dS \tag{3.17}$$

and

$$\int_{\Omega} \gamma \nabla u \cdot \nabla v dV = \int_{\partial \Omega} \gamma \nabla u \cdot \hat{n} v dS = \int_{\Gamma} \gamma \nabla u \cdot \hat{n} v dS \tag{3.18}$$

where $\Gamma = \bigcup_l E_l$ is the union of the electrodes and the current density is zero off the electrodes.

The boundary condition mentioned in last section (equation 3.11) can be rearranged to: $\gamma \nabla u \cdot \hat{n} = \frac{1}{Z_l}(V_l - u)$, therefore,

$$\int_\Omega \gamma \nabla u \cdot \nabla v dV = \sum_{l=1}^{L} \int_{E_l} \frac{1}{Z_l}(V_l - u) v dS \tag{3.19}$$

$$\int_\Omega \gamma \nabla u \cdot \nabla v dV - \sum_{l=1}^{L} \int_{E_l} \frac{1}{Z_l} V_l v dS + \sum_{l=1}^{L} \int_{E_l} \frac{1}{Z_l} u v dS = 0 \tag{3.20}$$

The basis functions v and the test function to approximate potentials for each i in the finite element method are suggested to be the same, $v = \sum_{i=0}^{N} u_i w_i$. Then substitute this into the equation,

$$\sum_{j=1}^{N} \left\{ \int_\Omega \gamma \nabla w_i \cdot \nabla w_j dV \right\} u_j + \sum_{l=1}^{L} \left\{ \int_{E_l} \frac{1}{Z_l} w_i w_j dS \right\} u_j - \sum_{l=1}^{L} \left\{ \int_{E_l} \frac{1}{Z_l} w_i dS \right\} V_l = 0 \tag{3.21}$$

Also, the Dirichlet boundary condition states total current $I_l = \int_{e_l} \gamma \frac{\partial u}{\partial n} dS$,therefore:

$$I_l = \int_{e_l} \frac{1}{Z_l}(V_l - u) dS = \int_{E_l} \frac{1}{Z_l} V_l - \sum_{i}^{N} \left\{ \int_{E_l} \frac{1}{Z_l} w_i dS \right\} u_i \tag{3.22}$$

and if we assume contact impedance Z_l is constant on electrodes, then:

$$I_l = \frac{1}{Z_l} \left| E_l \right| V_l - \frac{1}{Z_l} \sum_{i}^{n} \left\{ \int_{E_l} w_i dS \right\} u_i \tag{3.23}$$

where $\left| E_l \right|$ is the area(3D) or length(2D) of the lth eletrode.

The entire FEM system equations now take the form:

$$\begin{bmatrix} A & B \\ B' & C \end{bmatrix} \begin{bmatrix} u \\ V \end{bmatrix} = \begin{bmatrix} 0 \\ L \end{bmatrix} \tag{3.24}$$

where

$$A = \sum_{j=1}^{N} \int_{\Omega} \gamma \nabla w_i \cdot \nabla w_j dV + \sum_{l=1}^{L} \int_{E_l} \frac{1}{Z_l} w_i w_j dS \tag{3.25}$$

$$B = -\frac{1}{Z_l} \int_{E_l} w_i dS \tag{3.26}$$

$$C = diag\left(\frac{|E_l|}{z_l}\right) \tag{3.27}$$

3.2.3 Jacobian calculation

The complete matrix of partial derivatives of voltages with respected admittance parameters is the Jacobian matrix, sometimes called the sensitivity matrix. Jacobian matrix is widely used for solving optimization problems, and introduced in various algorithms. Two methods of driving the Jacobian matrix are introduced here.

Reciprocity theorem

The domain Ω in Figure 3-6, where a current I_ϕ flows into the region Ω with admittivity γ at point A and leaves at point B. Inside the region, the current I_ϕ leads to a potential distribution V_ϕ. And voltage measured between points C and D. Hence, the voltage U_{AB} is measured between points A, B due to the current I_ψ. Thus, the potential distribution will be V_ψ. When current apply to point C, D, the potential distribution V_ψ will be different to V_ϕ [120].

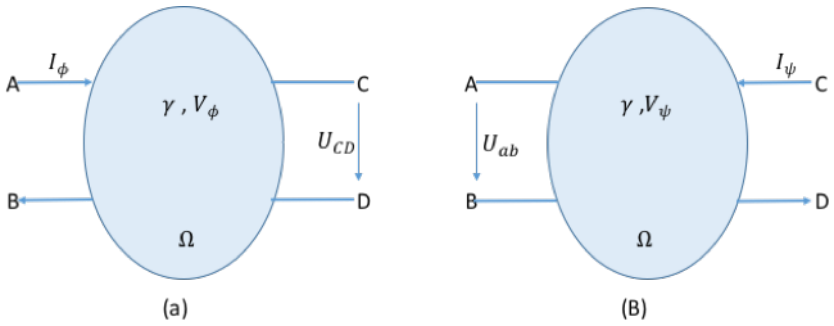

Figure 3-6: (a) Current apply to point AB (b) Current apply to point CD

Ohm's Law states that,

$$J = -\gamma \nabla V_\phi \tag{3.28}$$

where J is the current density of the domain.

Multiplication of Equation 3.28 with V_ψ and integrating the resulting equation over the boundary of the domain.

$$\int_{\partial\Omega} J V_\psi d\Gamma = -\int_{\partial\Omega} V_\psi \gamma \nabla V_\phi d\Gamma \tag{3.29}$$

Apply Divergence theorem to above equation,

$$\int_{\partial\Omega} V_\psi \gamma \nabla V_\phi d\Gamma = \int_\Omega \nabla \cdot (V_\psi \gamma \nabla V_\phi) d\Omega \tag{3.30}$$

And using Green's second identity and vector identity $\nabla \cdot (\psi A) = A \cdot \nabla\psi + \psi \nabla \cdot A$, the equation 3.30 can be derived to

$$\int_\Omega \nabla \cdot (V_\psi \gamma \nabla V_\phi) d\Omega = \int_\Omega \gamma \nabla V_\psi \cdot \nabla V_\phi d\Omega + \int_\Omega V_\psi \nabla \cdot \gamma(\nabla V_\phi) d\Omega \tag{3.31}$$

Since $\nabla \cdot \gamma(\nabla V_\phi) = 0$(Equation 3.9),the last term in above Equation is zero. Therefor,

$$U_{AB} I_\phi = -\int_\Omega \gamma \nabla V_\psi \cdot \nabla V_\phi d\Omega \tag{3.32}$$

$$U_{CD} I_\psi = -\int_\Omega \gamma \nabla V_\phi \cdot \nabla V_\psi d\Omega \tag{3.33}$$

And it can be determined immediately if $I_\phi = I_\psi = I$, then:

$$U_{AB} = U_{CD} = -\frac{1}{I} \int_\Omega \gamma \nabla V_\psi \cdot \nabla V_\phi d\Omega \tag{3.34}$$

When the domain is discretized with N finite elements, Equation 3.34 then becomes:

$$U_{AB} = -\frac{1}{I} \sum_{i=1}^{N} \gamma_i \int_{\Omega_i} \nabla V_\psi^i \cdot \nabla V_\phi^i d\Omega \tag{3.35}$$

Where Ω_i is the area of finite element i, and V_ψ^i and V_ϕ^i are the potential distributions in the finite element i. Generated duo to acting a current I on the point AB and CD. Hence the derivative of the voltage with respect to the i^{th} admittivity

yields:

$$\frac{\partial U_{CD}}{\partial \gamma_i} = -\frac{1}{I}\int_{\Omega_i} \nabla V_\phi(\gamma)^i \cdot \nabla V_\psi(\gamma)^i d\Omega \tag{3.36}$$

Perturbation theorem

A common Jacobian calculation is perturbation method, [121] and [122] described derivation of Jacobian based on perturbations in power. We take perturbations admittivity γ to $\gamma + \delta\gamma$, potential u to $u + \delta u$ and measurement voltage V_l to $V_l + \delta V_l$, with the current in each electrode I_l remained constant. Therefore, the total changes in power is:

$$\sum_l \bar{I}_l \delta V_l = -\int_\Omega \delta\gamma |\nabla u|^2 dV \tag{3.37}$$

The detail of the calculation is given for the complete electrode model case in [117].
Hence, for k^{th} element with a fixed current pattern, Jacobian is given by:

$$J_k = \frac{\partial V_{dm}}{\partial \gamma_k} = -\int_{\Omega_k} \nabla u(I^d) \cdot \nabla u(I^m) dV \tag{3.38}$$

where $u(I^d)$ is the potential for d^{th} drive pattern and $u(I^m)$ is the assumed measurement potential.

3.3 Inverse problem

The inverse problem, which also is the image reconstruction problem. Determining conductivity distribution use measured boundary data. To solve the inverse problem, the matrix described the mapping between boundary data distribution and the conductivity changes distribution in the interior is required, which is the Jacobian J. If distribution of admittance change $\partial\gamma$ expressed as x (a vector $x \in C^N$), and voltage change ∂V as b (a vector $b \in C^M$),the problem becomes to :

$$Ax = b \tag{3.39}$$

where A is the Jacobian (a matrix $A \in C^{M\times N}$) and we want to find x. In real case, the noise in images is unavoidable, it may come from data collection, image

formation process and so on. The standard approach for estimate true admittance distribution in noise $J\Delta\gamma + noise = \Delta V$ is given by least squares solutions to minimizes the difference between Ax and b. Residual error is minimized in order to make the solution to be closed to the true case.

$$x = argmin_x \|Ax - b\|^2 \tag{3.40}$$

However, the solution is not unique since the number of unknown variables N (the number of pixels) is much larger than the number of measurements M. Secondly, the small perturbation in measurement voltage data could be amplified so much, the solution is useless. So in practice EIT inverse problem is ill-posed. A common approach to solve ill-posed inverse problem is regularization, many algorithms have been used to approach the real admittance distribution.

3.3.1 Linear back-projection (LBP)

The linear back-projection [123] was a popular method in early medical EIT, in eqution 3.39, x can be solved directly by:

$$x = A^{-1}b \tag{3.41}$$

However, the inverse of Jacobian does not exist. The most direct and simple way to solve it is to replace J^{-1} with J^T (the transpose of Jacobian J), thus, giving the approximated solution:

$$\hat{x} = A^T b \tag{3.42}$$

Hence, a normalized or weighted form can be expressed as:

$$\hat{\Delta\gamma} = \frac{J^T \Delta V}{J^T \Delta u_\lambda} \qquad u_\lambda = [1, 1, ..., 1] \tag{3.43}$$

where u_λ is an identity vector. [124] Mathematically, the LBP algorithm is not accurate to provide a solution for the ill-posed problem, but a qualitative result can be yielded to obtain general view about the conductivity distribution. With the advantages of fast process and simplicity, the LBP was widely used in early on-line medical tomography.

3.3.2 Tikhonov regularization

Tiknonov regularization is used for solving ill-posed inverse problem by implanting additional information, a penalty function is introduced for optimisation. [125] In this thesis, image reconstruction which does not involve dynamical movement is contributed by Tiknonov regularization. A general form of Tikhonov regularization can be written as:

$$x = argmin_x \|J\Delta\gamma - \Delta V\|^2 + \|\Gamma\Delta\gamma\|^2 \tag{3.44}$$

where Γ is called the Tikhonov matrix, normally chosen as identity matrix in the most cases. In other cases, high pass operators may be used to enforce smoothness if the underlying vector is believed to be mostly continuous. This regularization improves the conditioning of the problem, thus enabling a numerical solution. An explicit solution, denoted by $\Delta\gamma$, is given by:

$$\Delta\gamma = (J^T J + \Gamma^T\Gamma)^{-1} J^T \Delta V \tag{3.45}$$

For $\Gamma = I$, $\Gamma^T = \alpha^2$, the equation can be rewritten as:

$$\Delta\gamma = (J^T J + \alpha^2 I)^{-1} J^T \Delta V \tag{3.46}$$

where α^2 is the regularization parameter dependent on the noise level and I is the identity matrix.

3.3.3 Singular value decomposition

The singular value decomposition (SVD) is the generalization of the eigendecomposition of a positive semidefinite normal matrix to any $m \times n$ matrix. It provides a means to obtain the solution of equation 3.39 directly, A can be decomposed as:

$$A = U\Sigma V^* \tag{3.47}$$

where $U = [u_1, u_2, ..., u_M]$, is an $M \times M$ orthogonal matrix, u_i are the eignvectors of AA^*; $V = [v_1, v_2, ..., v_N]$ is an $N \times N$ orthogonal matrix, v_i are the eigenvectors of A^*A and Σ is the diagonal matrix of singular values padded with zero to make an $M \times N$ matrix.

Once the SVD is known ,the solution of equation 3.39 can be written as: [126]

$$\hat{x} = V\Sigma^{-1}U^{*}b \tag{3.48}$$

3.3.4 Total variation

The total variation (TV) regularization method has been very attractive since it was first introduced in [127],it shows a good contribution to image quality and noise removal. Since the TV measures the total amplitude of the oscillations of a function, the regularization term or L_1-norm (sum of absolute values) in EIT imaging is defined as [128] :

$$G_{TV}(\Delta\gamma) = \|\nabla\Delta\gamma\|_1 \tag{3.49}$$

The regularization functional in a form of bounded variation (BV) also includes discontinuous functions, which makes the TV popular for the regularization non-smooth cases. Different approaches have been proposed for application of TV to EIT, a good review [129] was published which includes the comparison of TV algorithms based on primal and dual interior point method (PDIPM), the split Bregman (SB) method and linearised alternating direction method of multipliers (LADMM).

Spatiotemporal total variation(ST-TV)

A spatiotemporal total variation algorithm based on the Split Bregman method [130] has been successfully applied for imaging moving object in ERT [131], [132]. As in dynamic EIT, consecutively images are expected to show a strong correlation, where spatial and temporal gradient domains are involved based on the total variation [133]. In this thesis, a movie like reconstruction images in Chapter 6 was produced using ST-TV.

The spatiotemporal total variation problem can be expressed as:

$$arg\min_{\Delta\sigma} ||\nabla_{x,y}\Delta\sigma||_1 + ||\nabla_t\Delta\sigma||_1 \qquad s.t.||\tilde{A}\Delta\sigma - \Delta u||_2^2 \leq \delta \tag{3.50}$$

where two terms of the function represent spatial and temporal behaviour, and

where $\Delta\sigma$ represents a 3D (x, y, t) conductivity distribution and $\tilde{A}$ is an augmented Jacobain operating on an act in a frame-by-frame basis.

This constrained problem can be converted to an unconstrained problem by introducing a penalty function [130].

$$\Delta\sigma^{k+1} = \min_{\Delta\sigma} ||\nabla_{x,y}\Delta\sigma||_1 + ||\nabla_t\Delta\sigma||_1 + \frac{\mu}{2}||\tilde{A}\Delta\sigma - \Delta u||_2^2 \tag{3.51}$$

$$D(\Delta\sigma, \Delta\sigma^k) = \nabla\Delta\sigma - \nabla\Delta\sigma^k - < p^k, \Delta\sigma - \Delta\sigma^k > \tag{3.52}$$

where μ is a penalty weighting parameter in 3.51, $D(\Delta\sigma, \Delta\sigma^k)$ is the Bregman distance between optimal conductivity difference $\Delta\sigma$ and $\Delta\sigma^k$, p^k is the sub gradient at k in 3.52, and in each iteration:

$$p^{k+1} = p^k - \lambda\tilde{A}^T(\tilde{A}\Delta\sigma^{k+1} - \Delta u) \tag{3.53}$$

Since $\tilde{A}$ is linear, this complicated iteration constraint is equivalent to the simplified form:

$$\Delta u^{k+1} = \Delta u^k - \tilde{A}\Delta\sigma^{k+1} + \Delta u \tag{3.54}$$

Secondly, we can expand the Split Bregman formulation to both spatial and temporal domains by introducing the new complex-valued variables d_x, d_y, and d_t to replace $\nabla_x\Delta\sigma$, $\nabla_y\Delta\sigma$ and $\nabla_t\Delta\sigma$,the equation 4.1 is now reformulated as a new constrained problem:

$$\begin{aligned} \min_{d_x,d_y,d_t,\Delta\sigma} ||(d_x, d_y)||_1 + ||d_t||_1 + \frac{\mu}{2}||\tilde{A}\Delta\sigma - \Delta u||_2^2 \\ s.t \quad d_i = \nabla_i\Delta\sigma \quad i = x, y, t \end{aligned} \tag{3.55}$$

Then this constrained problem can be converted to an unconstrained form based on Bregman iterations [130] using penalty functions with properly valued b^k.

$$\begin{aligned} &\min_{d_x,d_y,d_t,\Delta\sigma} ||(d_x, d_y)||_1 + ||d_t||_1 + \frac{\mu}{2}||\tilde{A}\Delta\sigma - \Delta u^k||_2^2 \\ &+ \frac{\lambda}{2}||d_x^k - \nabla_x\Delta\sigma - b_x^k||_2^2 + \frac{\lambda}{2}||d_y^k - \nabla_y\Delta\sigma - b_y^k||_2^2 + \frac{\lambda}{2}||d_t^k - \nabla_t\Delta\sigma - b_t^k||_2^2 \end{aligned} \tag{3.56}$$

where λ is a constant penalty weighting parameter for the TV constraints. To

solve this minimization problem, we can apply generalized split Bregman which can be split into two subproblems and solved separately.

$$\begin{aligned}\Delta\sigma^{k+1} = &\min_{\Delta\sigma} \frac{\mu}{2}||\tilde{A}\Delta\sigma - \Delta u^k||_2^2 + \frac{\lambda}{2}||d_x^k - \nabla_x\Delta\sigma - b_x^k||_2^2 \\ &+ \frac{\lambda}{2}||d_y^k - \nabla_y\Delta\sigma - b_y^k||_2^2 + \frac{\lambda}{2}||d_t^k - \nabla_t\Delta\sigma - b_t^k||_2^2\end{aligned} \tag{3.57}$$

$$\begin{aligned}d_{x,y}^{k+1} = \min_{d_{x,y}} ||(d_x, d_y)||_2 + \frac{\lambda}{2}||d_x^k - \nabla_x\Delta\sigma^{k+1} - b_x^k||_2^2 \\ + \frac{\lambda}{2}||d_y^k - \nabla_y\Delta\sigma^{k+1} - b_y^k||_2^2\end{aligned} \tag{3.58}$$

$$d_t^{k+1} = \min_{d_t} ||d_t||_1 + \frac{\lambda}{2}||d_t^k - \nabla_t\Delta\sigma^{k+1} - b_t^k||_2^2 \tag{3.59}$$

In each iteration, new valued $\Delta\sigma^k$ and d_i^k are used to define a new problem, and constraints are imposed in each iteration:

$$\Delta u^{k+1} = \Delta u^k - \tilde{A}\Delta\sigma^{k+1} + \Delta u \tag{3.60}$$

$$b_i^{k+1} = b_i^k - d_i^{k+1} + \nabla_i\Delta\sigma^{k+1} \tag{3.61}$$

Further, splitting variables d_i can be solved using generalized shrink-age formulas [134], [135]:

$$d_t^{k+1} = shrink(\nabla_t\Delta\sigma^{k+1} + b_t^k, 1/\lambda) \tag{3.62}$$

$$d_{x,y}^{k+1} = max(s^k - 1/\lambda)\frac{\nabla_{x,y}\Delta\sigma^{k+1} + b_{x,y}^k}{s^k} \tag{3.63}$$

and

$$s^k = \sqrt{|\nabla_x\Delta\sigma^{k+1} + b_x^k|^2 + |\nabla_y\Delta\sigma^{k+1} + b_y^k|^2} \tag{3.64}$$

3.4 Image quality

It is important to evaluate the performance of reconstructed EIT images. A lot of reconstruction approaches have not been widely used because there was no criteria for judging the results on which approaches were best. To address this problem, [136] suggests a set of parameters which characterize the image qualities based on GREIT.

Amplitude response (AR)

AR measures the ratio of image pixel amplitudes in the target to that in the reconstructed images. It should be constant for any target and considered as the most important figure of merit in image quality. The AR can be calculated:

$$AR = \frac{\sum_k [\hat{x}]_k}{V_t \frac{\Delta\sigma}{\sigma_r}} \tag{3.65}$$

where V_t is the volume of the target in the electrode plane. $\Delta\sigma = \sigma_t - \sigma_r$, σ_t is the conductivity of target and σ_r is the reference conductivity.

Position error (PE)

PE describes whether reconstructed images faithfully represent the position of the target. The PE is defined by:

$$PE = r_t - r_q \tag{3.66}$$

where r_t is the distance from medium centre to CoG(centre of gravity) of the true target, and r_q is the distance from medium centre to CoG of the target which has one-fourth of the maximum amplitude. Therefore, PE is desired to be as small as possible.

Resolution (RES)

RES is defined as the radius ratio of the target and the medium, it is expected to be uniform and small.

$$RES = \sqrt{\frac{A_q}{A_0}} \tag{3.67}$$

where A_q and A_0 are the areas of one-fourth amplitude target and the entire reconstructed medium in pixels.

Shape deformation (SD)

SD represents the difference between reconstructed image shape and the true shape. Typically, the reconstruction algorithm will create circular images of

targets. SD calculates the fraction of the reconstructed one-fourth amplitude target which does not fit the circle of an equal area.

$$SD = \sum_{k \notin C} [\hat{X}_q] \Big/ \sum_{k} [\hat{x}_q]_k \tag{3.68}$$

where C is a circle centred at the CoG of one-fourth amplitude set with an equivalent area.

3.5 Conclusion

The basic EIT principles are discussed in this chapter. Different current patterns are reviewed first and followed by the forward problem including the mathematical set up of EIT, the finite element method and Jacobian calculations. Moreover, the inverse problem of EIT is illustrated, where some algorithms for image reconstructions are reviewed especially the spatiotemporal total variation. Quantitative parameters for image quality evaluation is demonstrated in the last section.

Chapter 4

Complex valued EIT

4.1 Introduction

In previous complex EIT research, people were focusing on the medical field as the biological tissue has different relative permittivity and also it is a frequency depended property. However, in other filed, EIT is normally ERT which is the resitivity been image using the real part of the voltage measurement, the permittivity of the object is not considered. In my work, I want to investigate the ability of the complex EIT system in imaging the conductivity and the permittivity distribution simultaneously, and to see the effect in reconstruction images of the three main properties: conductivity, relative permittivity and excitation frequency.

In previous complex study proposed by Yang [19], the derivation of Jacobian was wrong, since the contribution of imaginary part was not only the relative permittivity, but also the angular frequency. Also, the images they produced was not using the complex Jacobian, instead, they were using the EIDORS default one. And in the most recent research [18], simulation samples they selected were in different conductivity and relative permittivity at the same time, which lead to confusion of effect in the reconstruction images.

Hence, as introduced in Chapter 2.4, most ECT/ERC dual-modalities are required two independent sensing systems mounted in the same cross-section and

intended to obtain conductivity and permittivity distribution for the same cross-section. Instead of dual-modality, complex EIT which contains both resistive and capacitive impedance has the potential to determine conductivity and permittivity distribution using only one measuring system. This Chapter presents an in depth and systematic analysis of complex admittance data for simultaneous reconstruction of both conductivity and permittivity. A complex-valued forward model, Jacobian matrix and inverse solution are developed in the adjacent current excitation mode. The effects of different conductivity, realtive permittivity and frequency in reconstruction images are studied. Hence, a real life case simulation is established to test the ability of this complex EIT system. The work flow of this chapter conducted by myself can be expressed in the Figure 4-1.

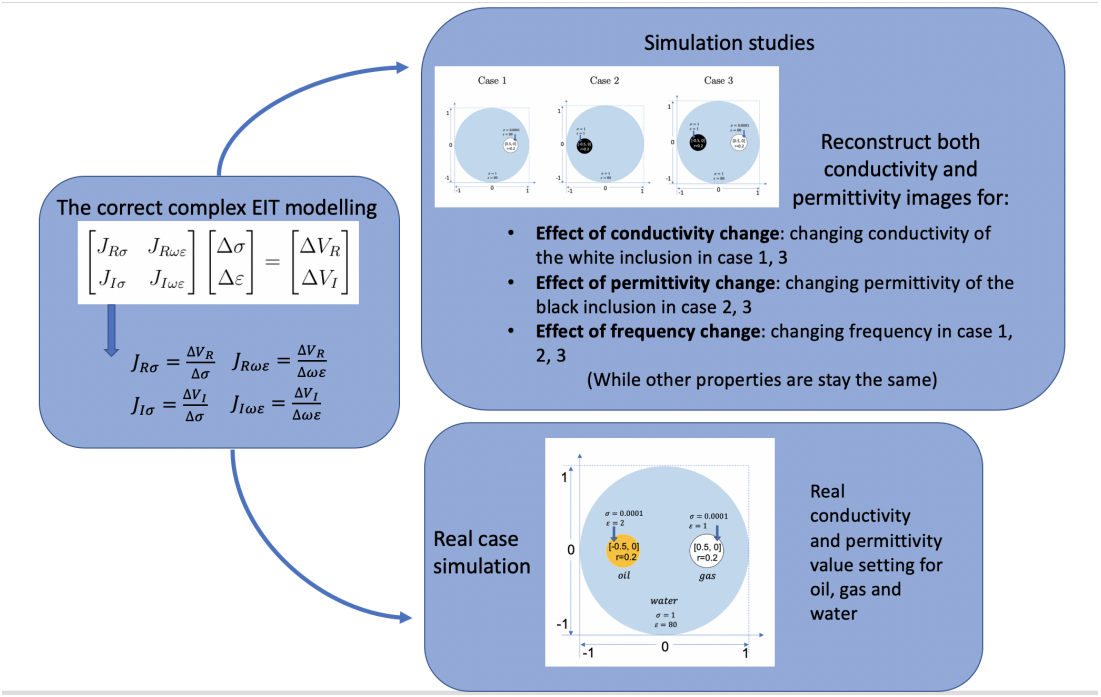

Figure 4-1: The work flow of the complex EIT

4.2 Method

The same as normal EIT algorithm approach introduced in Chapter 3, complex EIT reconstruction focuses on the relationship between the complex admittivity and the complex voltage measurements. The fundamental mathematical mod-

elling is based on previous study [19], but the derivation of the complex Jacobian in this study has been corrected and improved. As in his work, the permittivity perturbations did not consider the effect of the frequency, it had been simplified to $J_{II} = \frac{\Delta V_I}{\Delta \varepsilon}$. And there were three equations that were related to the imaginary part of voltage changes, the combination of the Jacobian matrix is inconsistent with the equations. Therefore, a clear and complete complex mathematical modelling is presented here.

The electrical impedance is the inverse of admittance γ , and it measures the ratio between the electric field and the electric current at location $x \in \Omega$.

$$\gamma(x) = \sigma(x) + i\omega\varepsilon(x) \tag{4.1}$$

$\sigma(x)$ and $\varepsilon(x)$ are the conductivity and permittivity. For an object occupy a two-dimensional region Ω with its boundary $\partial\Omega$, electrodes $el, l = 1, 2, 3, \ldots, L$ on the boundary. A current I with an angular frequency ω is applied to an adjacent electrodes pair, by calculating the divergence of both sides of the Maxwell equations, the equation 3.9 from last Chapter can be written as:

$$\nabla \cdot ((\sigma + i\omega\varepsilon)\nabla\hat{u}) = 0 \tag{4.2}$$

where $\hat{u}$ is complex electric potential.

To solve forward problem and Jacobian in complex EIT are the same as conventional EIT which introduced in chapter 3, but complex valued electric potential are considered instead of the scalar potential in this chapter. EIT imaging is generally a time-difference based method, which means that the difference between two measurements at different time is used to calculate the change in conductivity and permittivity distribution. Therefore, the inverse problem can be expressed as:

$$J_{complex}(\Delta\gamma_{complex}) = \Delta V_{complex} \tag{4.3}$$

which is:

$$J_{complex}(\Delta\sigma + i\omega\Delta\varepsilon) = \Delta V_R + i\Delta V_I \tag{4.4}$$

If σ and V_R are the real parts of the admittivity and the voltage, respectively, while ε and V_I are the imaginary parts, the complex voltage measurements are

formed by:

$$\begin{aligned} J_{R\sigma}\Delta\sigma + J_{R\omega\varepsilon}\Delta\varepsilon &= \Delta V_R \\ J_{I\sigma}\Delta\sigma + J_{I\omega\varepsilon}\Delta\varepsilon &= \Delta V_I \end{aligned} \tag{4.5}$$

And the equation above can be expressed in a form of matrix as:

$$\begin{bmatrix} J_{R\sigma} & J_{R\omega\varepsilon} \\ J_{I\sigma} & J_{I\omega\varepsilon} \end{bmatrix} \begin{bmatrix} \Delta\sigma \\ \Delta\varepsilon \end{bmatrix} = \begin{bmatrix} \Delta V_R \\ \Delta V_I \end{bmatrix} \tag{4.6}$$

The Jacobian which corresponds to the effect of perturbations in the conductivity on the real part of the measurements can be expressed as:

$$J_{R\sigma} = \frac{\Delta V_R}{\Delta\sigma} \tag{4.7}$$

And the Jacobian corresponding to the effect of the permittivity perturbations on the real part of the measurements is:

$$J_{R\omega\varepsilon} = \frac{\Delta V_R}{\Delta\omega\varepsilon} \tag{4.8}$$

Therefore, the remaining two combinations would be:

$$J_{I\sigma} = \frac{\Delta V_I}{\Delta\sigma} \tag{4.9}$$

$$J_{I\omega\varepsilon} = \frac{\Delta V_I}{\Delta\omega\varepsilon} \tag{4.10}$$

Then the standard Tikhonov regularization algorithm is adopted to solve this problem, and substitute complex format value to equation 3.46 where discussed in Chapter 3:

$$\begin{bmatrix} \Delta\sigma \\ \Delta\varepsilon \end{bmatrix} = \left(\begin{bmatrix} J_{R\sigma} & J_{R\omega\varepsilon} \\ J_{I\sigma} & J_{I\omega\varepsilon} \end{bmatrix}^T \begin{bmatrix} J_{R\sigma} & J_{R\omega\varepsilon} \\ J_{I\sigma} & J_{I\omega\varepsilon} \end{bmatrix} + \alpha^2 L \right)^{-1} \begin{bmatrix} J_{R\sigma} & J_{R\omega\varepsilon} \\ J_{I\sigma} & J_{I\omega\varepsilon} \end{bmatrix}^T \begin{bmatrix} \Delta V_R \\ \Delta V_I \end{bmatrix} \tag{4.11}$$

where α is the regularization parameter and L is the regularization matrix.

4.3 Simulation of the complex measurements

EIDORS (http://eidors3d.sourceforge.net/) is a software algorithm for image reconstruction of EIT based on MATLAB. It provides sets of code which can be used directly to produce reconstruction images and it is a open resource for EIT research. As a time difference imaging method, EIT needs two sets of measurement: a background scenarios with conductivity and relative permittivity set as $\sigma = 1S/m$ and $\varepsilon = 80$ as a reference to simulate the water, and a sample scenario which inclusions with different properties are added. To obtain an accurate EIT model for my work, a uniform dense mesh of 1024 elements is created using EIDORS for the forward model, and the value of each element is set to be $\sigma + i\omega\varepsilon_0\varepsilon$, after solving the forward problem, the complex valued voltage measurement V_h can be calculated for the background. And then, to obtain the true complex Jacobian matrix, the perturbation method is used based on Equation 4.7 to 4.10: perturbing all 1024 elements with $\sigma + \Delta\sigma$ or $\varepsilon + \Delta\varepsilon$, the detail has explained following:

i After the background V_h been determined, the value of all 1024 elements are ready to perturb, and set to be $(\sigma + \Delta\sigma) + i\omega\varepsilon_0\varepsilon$. Which is increasing the conductivity of all elements by $\Delta\sigma$

ii Solving the new forward problem to get the new complex valued voltage measurement V_i for after perturbation.

iii Using the real part of changes of V_i and V_h, divided by $\Delta\sigma$ to get the $J_{R\sigma}$ as in Equation 4.7: $J_{R\sigma} = \frac{\Delta V_R}{\Delta\sigma}$, where $\Delta V_R = real(V_i - V_h)$.

iv Using the imaginary part of changes of V_i and V_h, divided by $\Delta\sigma$ to get the $J_{I\sigma}$ as in Equation 4.9: $J_{I\sigma} = \frac{\Delta V_I}{\Delta\sigma}$, where $\Delta V_I = imaginary(V_i - V_h)$.

The derivations of rest components $J_{R\omega\varepsilon}$ and $J_{I\omega\varepsilon}$ in the complex valued Jacobian matrix are the same as above, just change the perturbation to permittivity, the complete code can be seen in Appendix B.

And the real and imaginary voltage measurements of background are plotted in Figure 4-2.

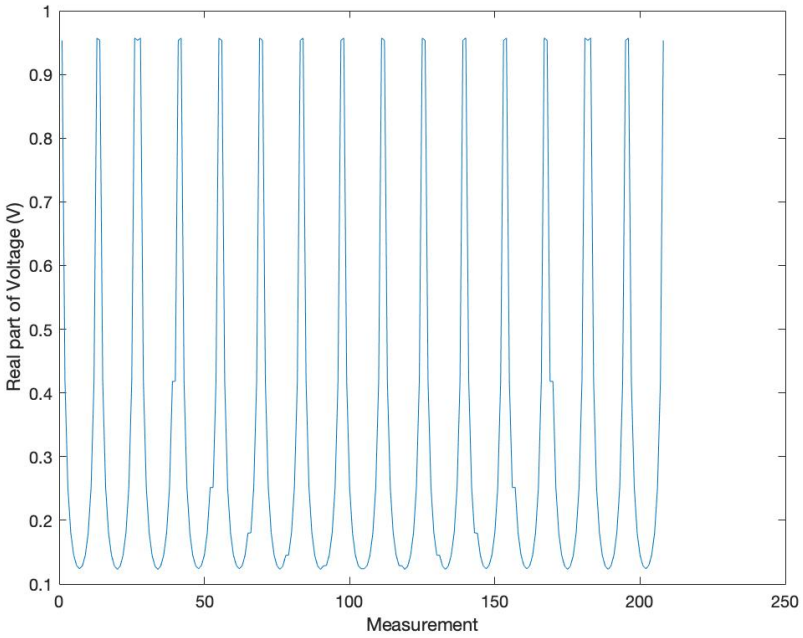

(a) Real part of the Voltage

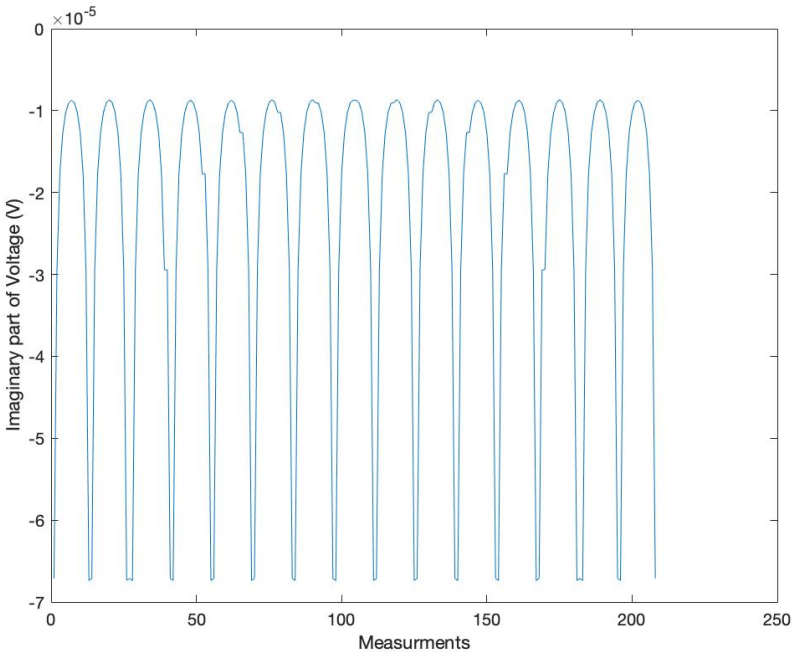

(b) Imaginary part of the Voltage

Figure 4-2: Voltage measurements of the background

Three cases are designed as in Table 4.1 to compare the conductivity and permittivity reconstruction. The radius of the circular phantom is normalised to 1. In case 1, a white circular inclusion of 0.2 radius added at the coordinate (0.5, 0), the conductivity set to be $0.00001 S/m$ and the relative permittivity keeps the same as the background. In case 2, a black circular inclusion of 0.2 radius added at the coordinate (-0.5, 0) and the relative permittivity set to be 1 while the conductivity is the same as background. In case 3, inclusions in case 1 and 2 are added at the same coordinate simultaneously.

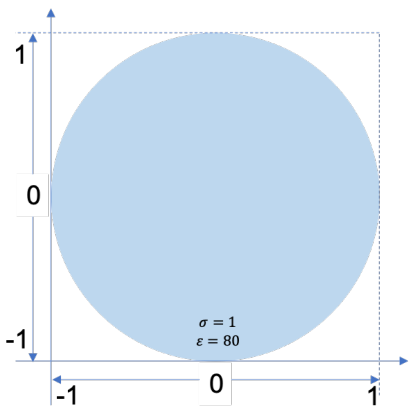

Background

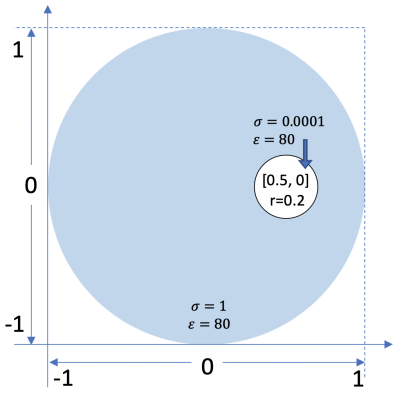

Case 1

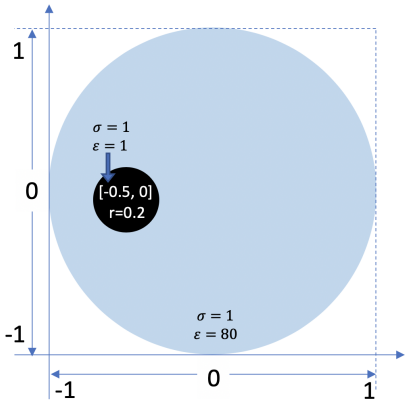

Case 2

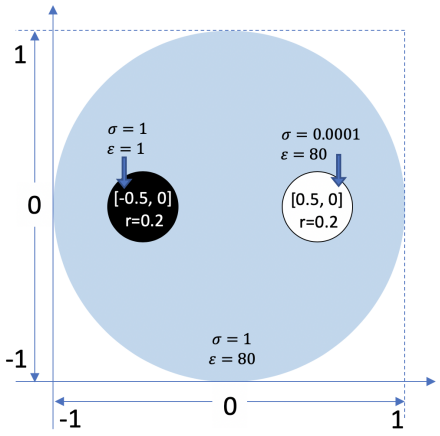

Case 3

Table 4.1: Three cases of different electric properties and positions for simulations.

The excitation frequency is set as $100kHz$, Jacobian is calculated using proposed method in last section, therefore, the size of complex Jacobian is $[416 \times 2048]$. And in the inverse problem, the conductivity reconstruction is solved using the real part of the voltage measurement changes and correspondingly the permittivity reconstruction is using the imaginary part. The reconstruction images of conductivity changes and permittivity changes for three cases are plot in Table 4.2 .

Case 1	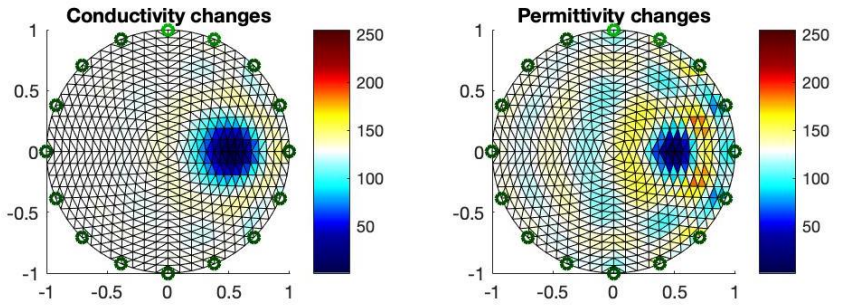
Case 2	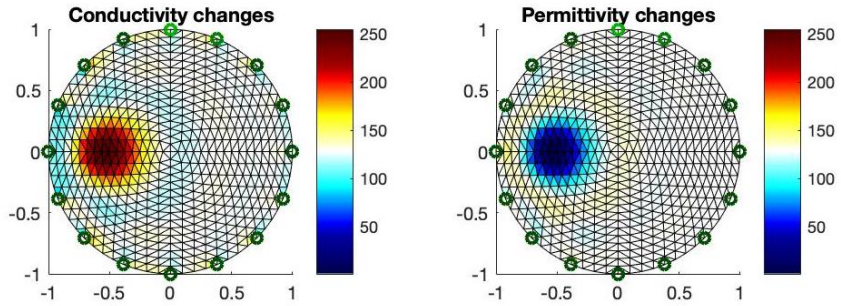
Case 3	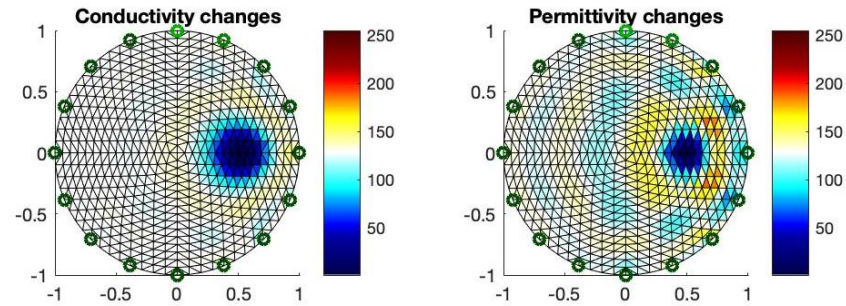

Table 4.2: Image reconstruction for conductivity changes and permittivity changes using complex Jacobian

Discussion

For case 1, the conductivity change is plotted using the real part of voltage measurement changes, the non-conductive inclusion is imaged as expected and blue indicates the conductivity of the inclusion is lower than the background. In permittivity reconstruction image, there are still a small circle in the corrected position of the inclusion. However, in theory, the permittivity reconstruction image should not show anything since the permittivity of the inclusion does not change, it is the same as the background, which can be found that the conductivity changes do affect the imaginary part of voltage measurement. In this case, the conductivity changes can be determined by $\Delta V_R = J_{R\sigma}\Delta\sigma$ and the permittivity changes is obtained by $\Delta V_I = J_{I\sigma}\Delta\sigma$ from equation 4.5.

For case 2, the conductivity changes should not be imaged theoretically since the conductivity of the inclusion does not change. However, the conductivity reconstruction image still show the inclusion in red which indicates that the relative permittivity does affect the real part of the voltage changes as in equation 4.5 $\Delta V_R = J_{R\omega\varepsilon}\Delta\varepsilon$. And for the permittivity reconstruction image, the inclusion is plotted in blue as the permittivity is lower than the background which consists with the true case.

In case 3, only the inclusion with changing conductivity is imaged for both conductivity and permittivity distribution. I think the reason for that is the permittivity changes are too small to be taken account in as the $\varepsilon_0 = 8.85 \times 10^{-12} F/m$. Thus the equations 4.5 are dominated by the $\Delta\sigma$ for both real and imaginary parts of voltage changes and only the inclusion with changing conductivity can be imaged.

4.3.1 The effect of conductivity change

To further analysis the effect of conductivity of inclusions to complex EIT image reconstruction, the physical setup for case 1 and 3 are selected. The white inclusion's conductivity is increasing from $0.00001 S/m$ to $1000 S/m$ while all other properties including the relative permittivity and the excitation frequency stay the same. The reconstruction images for Case 1 and 3 are shown in Table 4.3 and Table 4.4 respectively.

Conductivity (S/m)	Reconstruction
$\sigma = 0.00001$	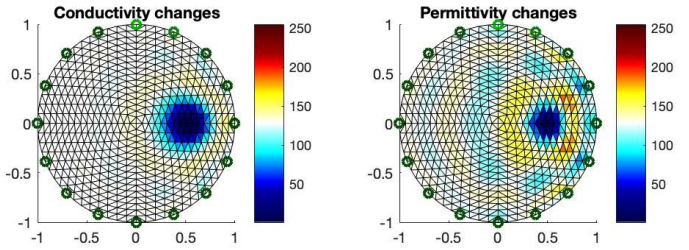
$\sigma = 10$	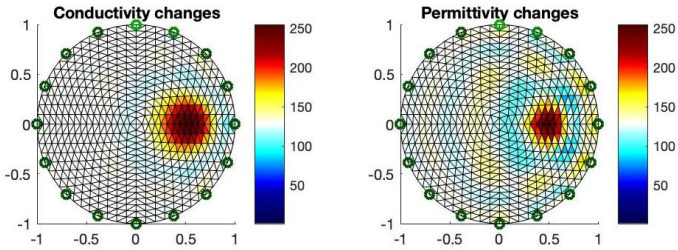
$\sigma = 100$	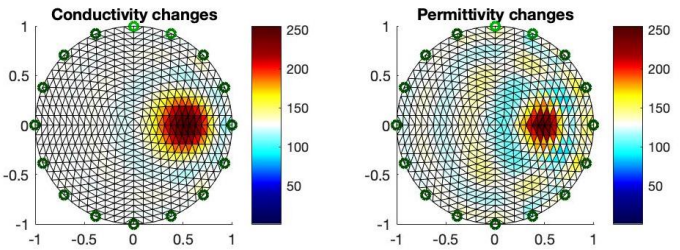
$\sigma = 1000$	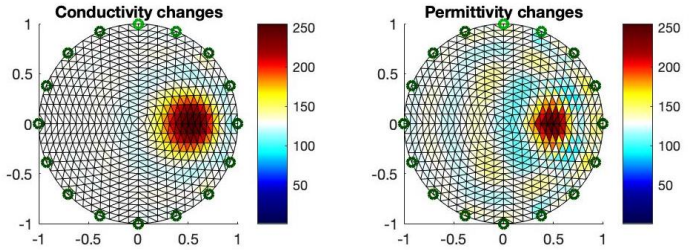

Table 4.3: Image reconstruction for Case 1 with changing conductivity

Conductivity (S/m)	Reconstruction
$\sigma = 0.00001$	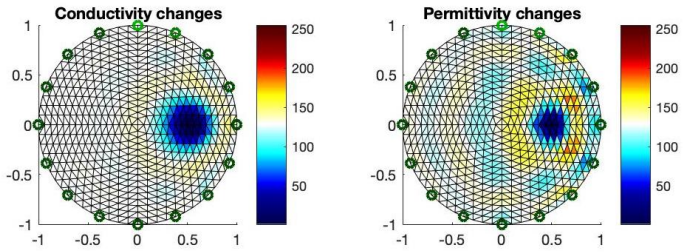
$\sigma = 10$	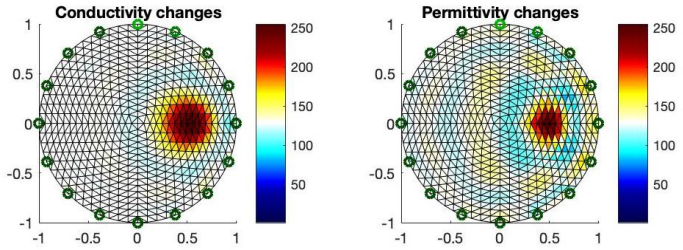
$\sigma = 100$	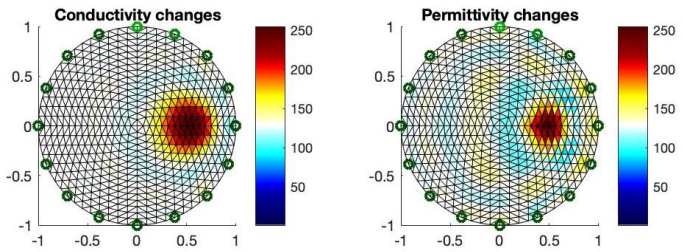
$\sigma = 1000$	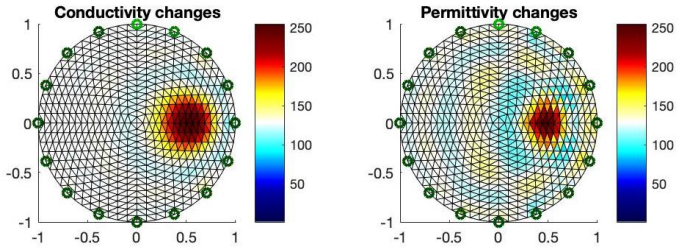

Table 4.4: Image reconstruction for Case 3 with changing conductivity

Discussion

The results of the changing conductivity are the same as expected for all reconstructed images in Case 1, the inclusion shows in red when the conductivity is bigger than the background. Again, the permittivity images obtained from the imaginary part of the voltage change showed some conductivity information as

$J_{I\sigma}\Delta\sigma + J_{I\omega\varepsilon}\Delta\varepsilon = \Delta V_I$, where the $\Delta\varepsilon = 0$.

For Case 3, only one inclusion can be seen in the conductivity reconstruction images for all conductance since the permittivity is too small, the real part of voltage change is dominated by $J_{R\sigma}\Delta\sigma$. Also the permittivity reconstruction images obtained from ΔV_I are dominated by $J_{I\sigma}\Delta\sigma$ as well.

4.3.2 The effect of permittivity change

The same multi-conductivity approach, to further analysis the effect of relative permittivity of inclusions to complex EIT image reconstruction, case 2 and 3 are selected. The black inclusion's relative permittivity is increasing from 1 to 80000 since the relative permittivity of the calcium copper titanate can reach to 250000 in real life case [137]. And all other properties including the conductivity and the excitation frequency stay the same. The reconstruction images for Case 2 and 3 are shown in Table 4.5 and Table 4.6 respectively.

Relative permittivity	Reconstruction
$\varepsilon = 1$	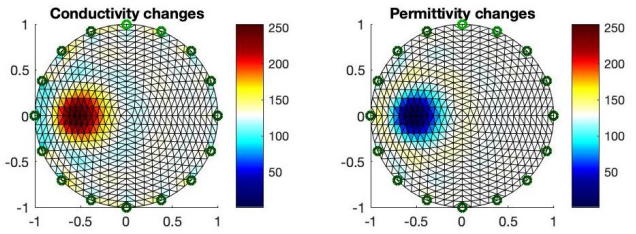
$\varepsilon = 800$	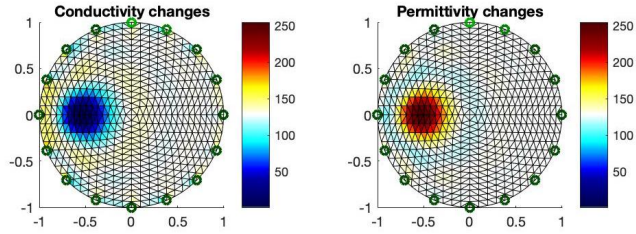
$\varepsilon = 8000$	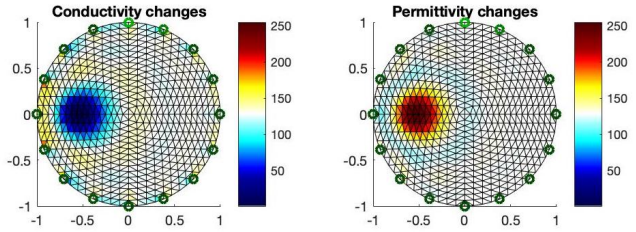
$\varepsilon = 80000$	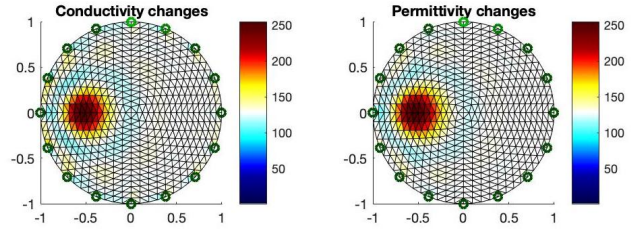

Table 4.5: Image reconstruction for Case 2 with changing permittivity

Relative permittivity	Reconstruction
$\varepsilon = 1$	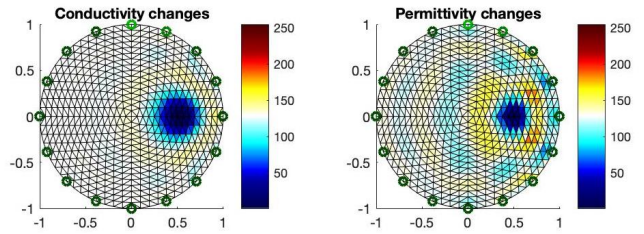
$\varepsilon = 800$	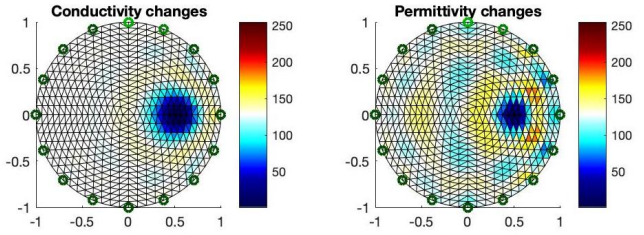
$\varepsilon = 8000$	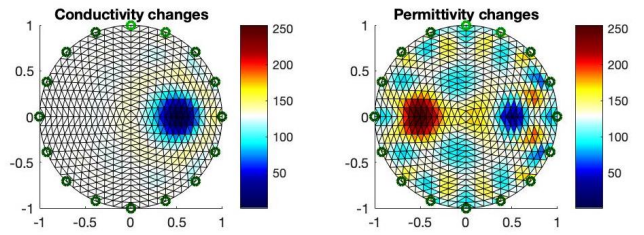
$\varepsilon = 80000$	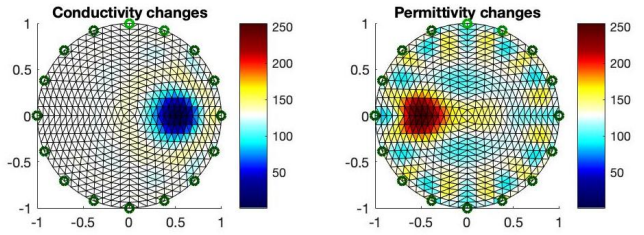

Table 4.6: Image reconstruction for Case 3 with changing permittivity

Discussion

The color reflection in reconstruction images of the permittivity changes are correct as expected for case 2. The reconstructed images of the conductivity changes shows the right position of the inclusion, but the color is not making any sense and the size of the inclusion is bigger when $\varepsilon = 800$ and 8000. For case 3, the permittivity changes start to show both inclusion when the relative permittiv-

ity starts increasing. Which means the contrast of $J_{I\sigma}\Delta\sigma$ and $J_{I\omega\varepsilon}\Delta\varepsilon$ is getting smaller. When $\varepsilon = 80000$, the inclusion with changing permittivity becomes dominated and the inclusion with different conductivity fades out in the image. From this we can see that the permittivity reconstruction can image the conductivity and the permittivity change simultaneously when the absolute value of $J_{I\sigma}\Delta$ and $J_{I\omega\varepsilon}\Delta\varepsilon$ is balanced. On the other hand, the reconstructed images of conductivity changes show the inclusion with different conductivity in blue at right position as expected without any effect from the other inclusion.

4.3.3 The effect of frequency change

Since the permittivity changes are highly connected with frequency, the imaginary part of the voltage measurements are not effected by the relative permittivity only, but also the frequency. To further analysis the effect of the excitation frequency to complex EIT image reconstruction, all three cases are selected. The setting of all properties are the same as in Table 4.1, but the excitation frequency is increasing. Also the Jacobian is updated every time with corresponding frequency.

Frequency	Reconstruction
$f = 100kHz$	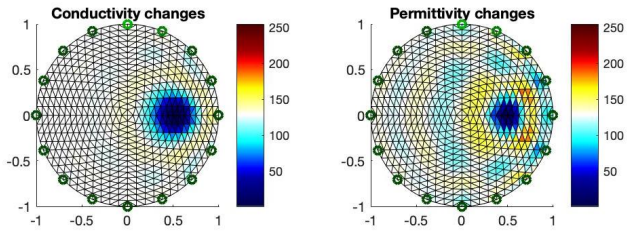
$f = 500kHz$	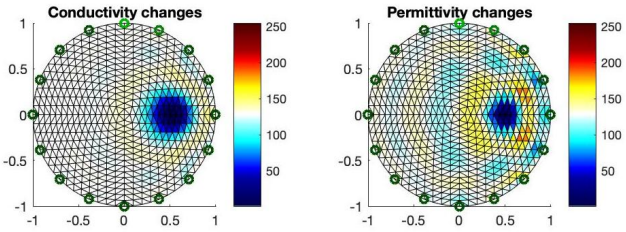
$f = 1MHz$	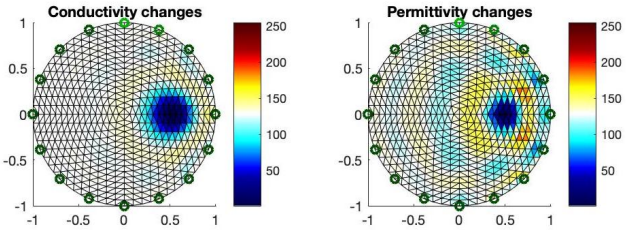
$f = 5MHz$	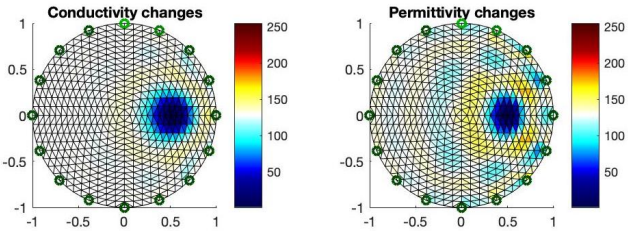
$f = 10MHz$	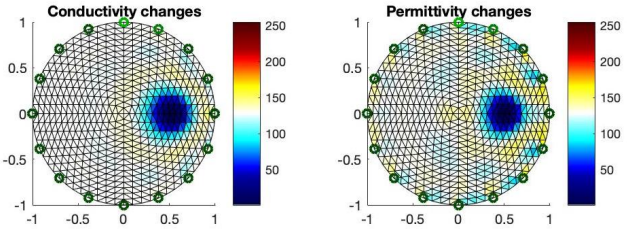

Table 4.7: Image reconstruction for Case 1 with different excitation frequency

Frequency	Reconstruction
$f = 100kHz$	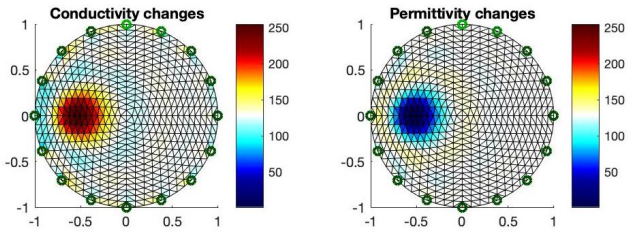
$f = 500kHz$	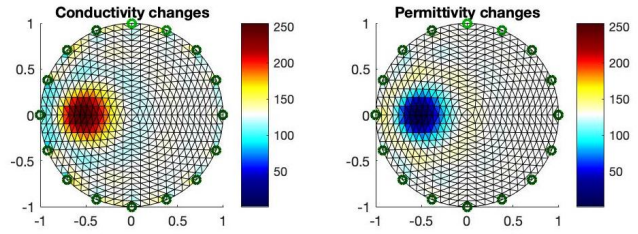
$f = 1MHz$	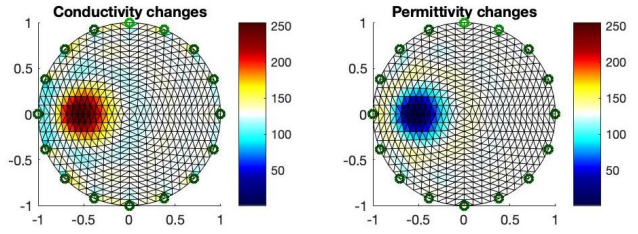
$f = 5MHz$	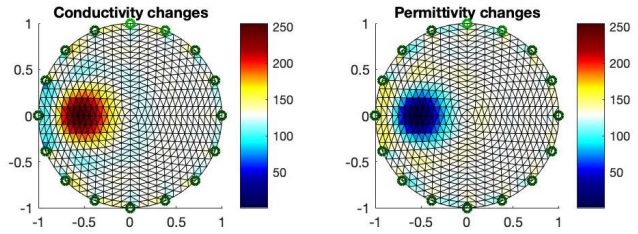
$f = 10MHz$	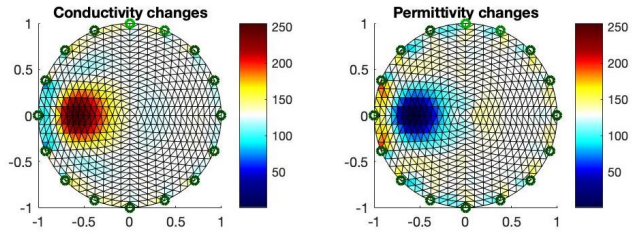

Table 4.8: Image reconstruction for Case 2 with different excitation frequency

Frequency	Reconstruction
$f = 100kHz$	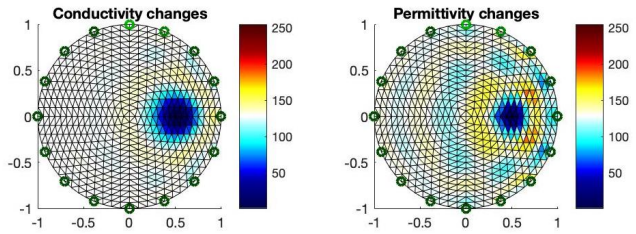
$f = 500kHz$	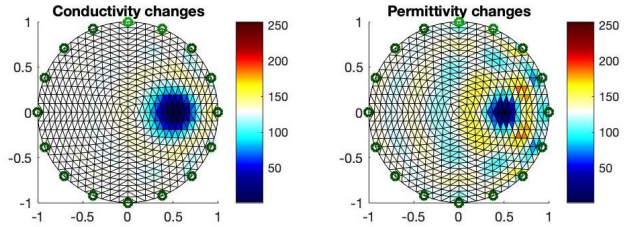
$f = 1MHz$	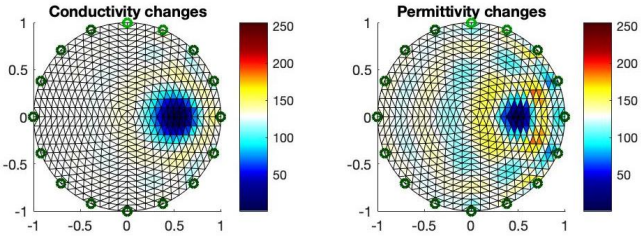
$f = 5MHz$	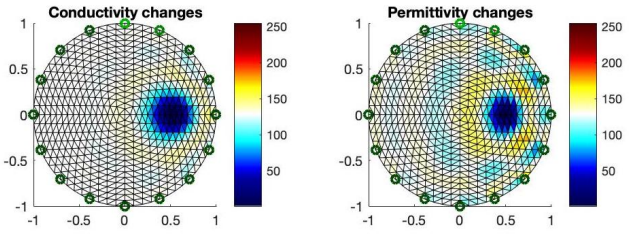
$f = 10MHz$	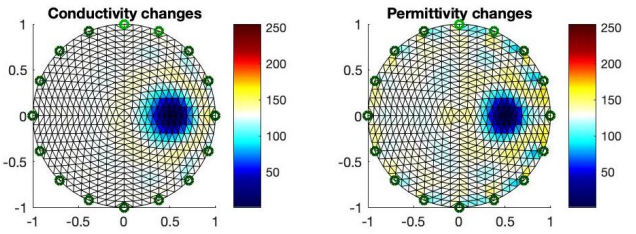

Table 4.9: Image reconstruction for Case 3 with different excitation frequency

Discussion

In case 1, the inclusion with different conductivity does not affect by the frequency since it is not a bio-sample. Therefore, all reconstruction images should be the same for any excitation frequency. In case 2, the permittivity reconstruction images are showing the right position of the inclusion in blue in all frequencies, and the conductivity reconstruction images are showing the consistent behavior as in Table 4.5 when $\varepsilon = 1$. Finally in case 3, the conductivity reconstruction image can only shows the inclusion with changing conductivity, which indicates that the contrast between $J_{R\sigma}\Delta\sigma$ and $J_{R\omega\varepsilon}\Delta\varepsilon$ is still big. At the same time, in the permittivity reconstruction image, the ΔV_I is still dominated by $J_{I\sigma}\Delta\sigma$ and only the inclusion with changing conductivity is shown. Therefore, we can assume that when the contrast between $J_{R\sigma}\Delta\sigma$ and $J_{R\omega\varepsilon}\Delta\varepsilon$ becomes small, which means the frequency is high enough, the reconstruction image will show both inclusions. But technically, any excitation frequency above $10MHz$ will not be considered as a EIT problem anymore, the higher frequency simulation will not be necessary. And another interesting observation is that the inclusion with changed conductivity in permittivity reconstruction images of Case 1 and 3 are getting clearer when the frequency is increasing.

4.3.4 Simulation for three-phase material

To illustrate this complex EIT system in real life application, a further case is designed to present the three-phase water/gas/oil scenario in process industry as shown in Fig 4-3a. Hopefully, the permittivity reconstruction image can be used in distinguishing the oil and air phase if this complex EIT works. The position of the inclusions is the same as in Case 3, but the conductivity and the permittivity value is set as in Table 1.1, where the left inclusion presents the oil phase with conductivity = 0.0001 mS/m, relative permittivity = 2 and the right one presents gas with conductivity = 0.0001 mS/m, relative permittivity = 1. The excitation frequency is $50kHz$ and the corresponded Jacobian is applied.

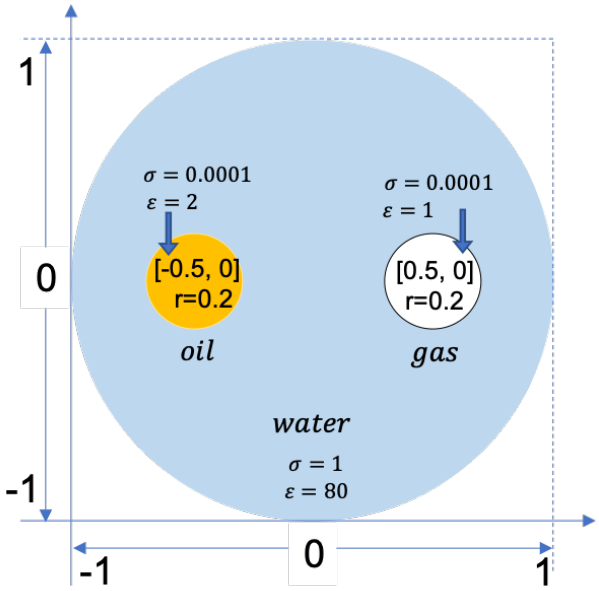

(a) True case of three-phase material imaging

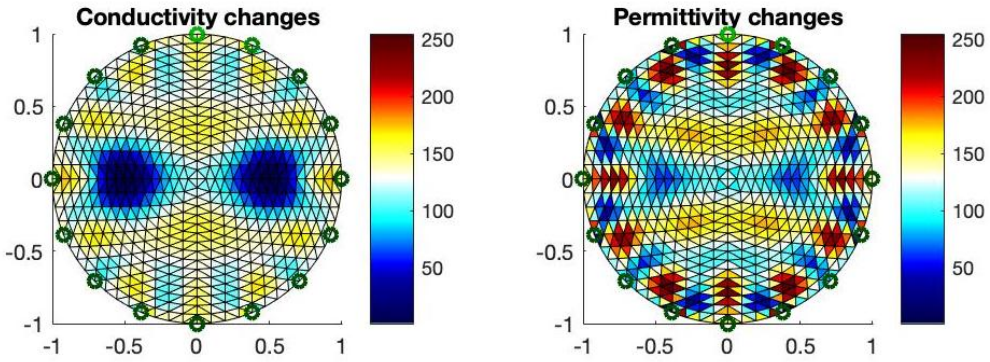

(b) Reconstruction images for conductivity and permittivity change

Figure 4-3: Simulation of three-phase material using complex EIT

The result of reconstruction images are shown in Fig 4-3b. The conductivity image successfully presents the two non-conducting phases in correct position, however, there is no distinguishing in which is oil or gas for now. In permittivity image, there are two shallow and blurry shadows in correct position, but the noise at the boundary seriously destroys the result. If the inclusions are placed near the boundary, the reconstruction image would fail to present them. Therefore, current resolution of the EIT permittivity reconstruction image has

not reach the level of distinguishing the material with such small contrast in relative permittivity, this complex system fails in three-phase material imaging and still critical.

To further analysis why the permittivity reconstruction is so hard, the voltage measurement against changing conductivity and permittivity has been plotted.

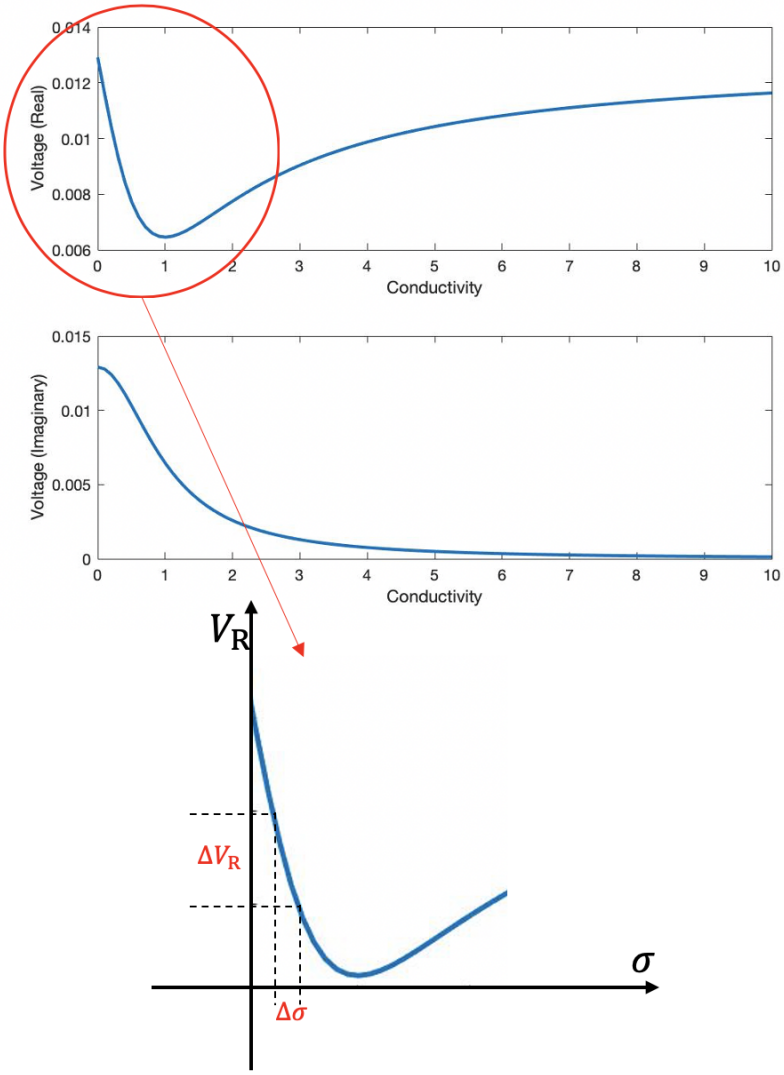

Figure 4-4: Voltage measurements against changing conductivity

Normally, we are using the real part of the voltage measurement to determine the conductivity changes since a small conductivity change can reflect in a large real part voltage changes as shown in Figure 4-4. When it comes to permittivity changes, only a small change can be reflected in the imaginary part voltage measurement as shown in Figure 4-5. And to be noticed that the value of imaginary part voltage in this case goes to $\times 10^{-3}$, which is way smaller. This is why makes the permittivity imaging so hard.

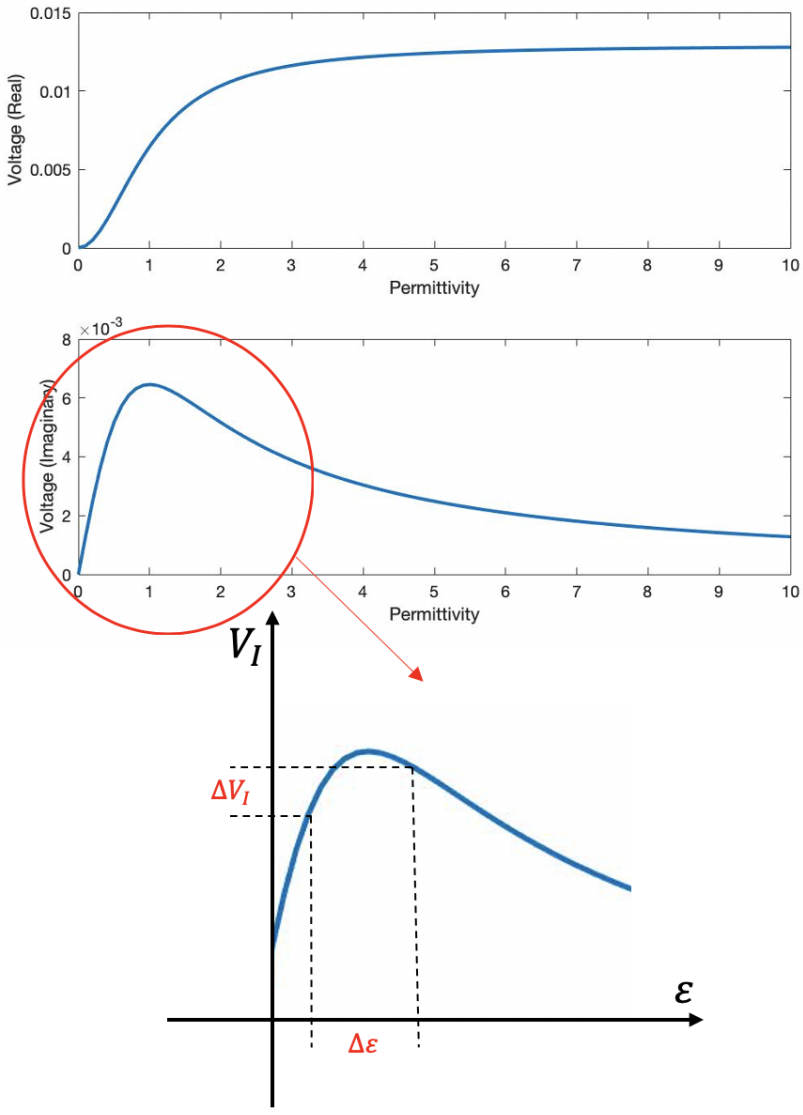

Figure 4-5: Voltage measurements against changing permittivity

4.4 Conclusion

Simulation result fails in detecting two inclusions (Case 3) in conductivity reconstruction images for all cases, but the permittivity reconstruction images are able to show the two inclusions at the same image if the relative permittivity of one inclusion is high enough. At this point, we cannot simply say that the conductivity distribution of ROI can be produced by the real part of voltage measurement, or the imaginary part of voltages measurement reflected the permittivity distribution. It is really hard to separate the conductivity and the permittivity distributions just from the real or imaginary component of the measurements. Therefore, the reconstructed images of the conductivity distribution do contain the information of the permittivity, and the same for the permittivity distribution. Hence, the real case application simulation in three-phase material imaging fails. It is still difficult for complex EIT to generate both pure conductivity and permittivity distributions so far, which means the application of using the complex EIT for imaging both the conductivity and permittivity distribution is critical and needs further investigation.

Chapter 5

Water dominated three-phase material imaging

5.1 Introduction

Three-phase material imaging such as oil, gas and water is a critical problem in many processes. Monitoring and separation of each phase before corresponding process can be a key to realise cost efficiency production. In the oil and gas industry such a tool can generate great environmental benefits. In recent years, several multi-modality imaging systems are being adapted for such an application. It is not possible to gain information on three phase flow using a single imaging modality that can be deployed in production field. For a three-phase flow dominated by water phase, this is more challenging. The capability of the majority of current dual-modality systems was only demonstrated under limited flow regime conditions, and mostly are oil based. In such condition, a technique which is able to distinguish gas from liquid and merged with EIT can be a solution. A quantitative ultrasonic travel-time tomography [138] developed by my colleague is an good option which able to determine air from liquid depending on the sound velocity. Such combination, providing the answer to the challenge of the water dominate mode: the EIT is able to image the non-conductive phases of oil and gas, but not able to separate them. The EIT two-phase imaging then complimented with the speed of sound imaging of the ultrasound transmission

tomography (UTT), which can separate liquid (oil and water) and gas.

This chapter presents a novel combined imaging system including EIT, and UTT for distinguishing three-phase material. A dual modality EIT-UTT system combining a 32-electrode EIT array and a 32-transducer UTT sensor array is developed to demonstrate this novel three-phase material imaging. The concept was demonstrated using simulation study and then shown with experimental lab tests. Measurement principles, method and a image fusion strategy are described, experiment based on several three-phase scenarios are established, and the results show successful distinguishable for all three phases. This chapter is based on the published journal paper [48]. And the work flow of this chapter conducted independently is in Figure 5-1.

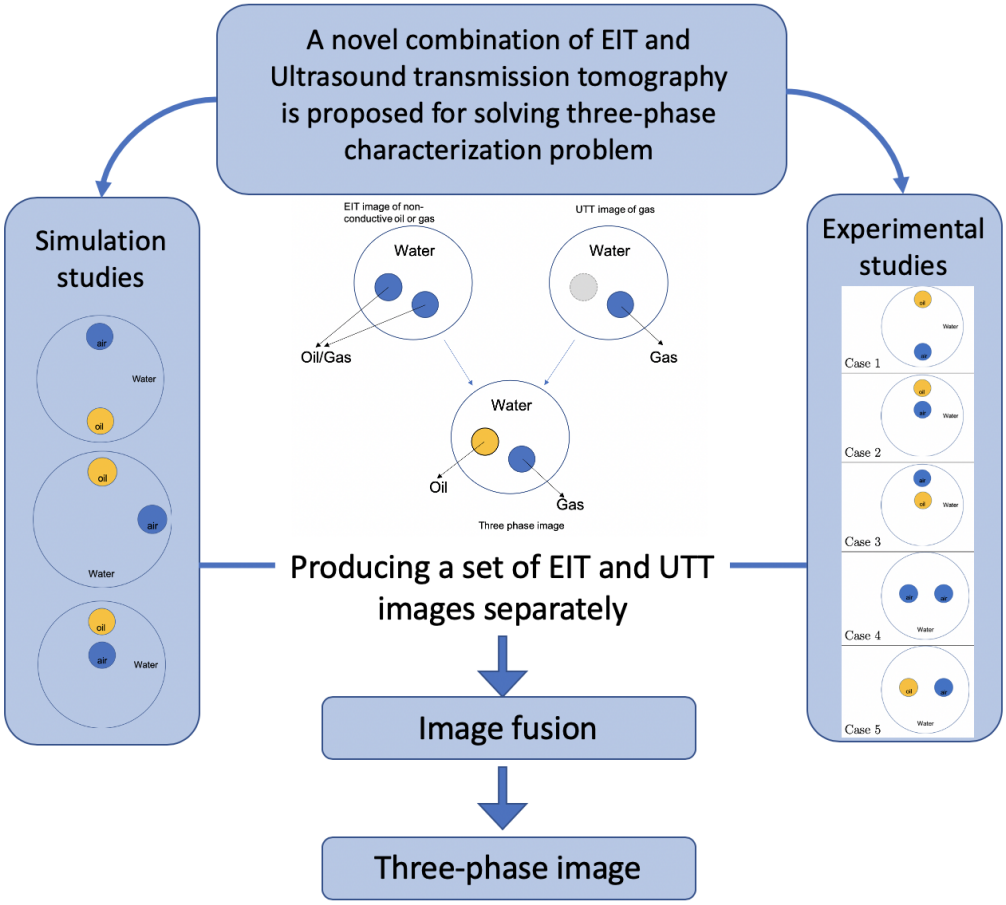

Figure 5-1: The work flow of three-phase material imaging

5.2 Ultrasound transmission tomography

Ultrasonic has been widely used for imaging and online monitoring of industrial processes. Ultrasounds have a non-destructive and non-invasive property and they can provide quality information as it travels with varying speeds in different media. Working on the concept of the ultrasonic tomography forward problem, someone must be based on the physics of the acoustics. In the meanwhile, acoustics can have a too wide extensive behaviour to be modelled directly, if someone tries to reconstruct all the full- wave information. Therefore, reconstruction methodologies are based on single attributes of the big amplitude waveforms captured by sensors. Such reconstruction is the transmission or reflection method which both of them are based on specific values of the full signal that is recorded by the sensors.

Traditionally, the propagation of the ultrasonic wave is considered as a straight line from the transmitter to receiver in the UTT mode. Therefore, a spherical wave (cone-beam) could be considered as an infinite sum of plane waves (fan-beam). Each spherical wave can be approximated by a cone of rays and subsequently, every plane wave by a fan of rays. In an ultrasonic annular array of 32-transducer, the transducers work as both transmitter and receiver, mounted at the outer boundary of the phantom. When one transducer works as transmitter, the ultrasonic signal is sent across the phantom, and other transducers work as receivers and can record the transmitted or reflected/scattered ultrasonic signals from various directions.

The ultrasonic wave can be reflected between materials with different acoustic impedance; therefore, only the transmission signal will be used in this work since the enclosed phantom wall can cause strong reflections. Based on the assumption of straight-line propagation, the ultrasonic wave propagates in different materials with different speeds, time-of-flight (TOF) inside of the phantom can be influenced by the material distribution [139]. Hence, the material distribution inside the phantom can be imaged by measuring the TOF of the ultrasonic signal between transducers. Meanwhile, the fan-shaped beam projection allows simultaneous interrogation of a large area, ensuring the maximum number of sensors receive the directly transmitted signal in every beam projection. The transducers

adjacent to the transmitter are disabled during measurement because the limitation of the ultrasonic beam angle and no meaningful transmission signal will be received by them. Therefore, transducer 1 emits ultrasonic signal and transducer 9 to 25 can simultaneously detect the transmission signals. Then transducer 2 is excited and transducer 10 to 27 are used for detection at the same time. The process is repeated until all transducers have worked as a transmitter, and a set of TOF measurements can be used for image reconstruction.

5.3 Method

This section describes the basic principle of operation and computational models of the EIT as well as UTT. Some main properties and characteristics of the forward and inverse problem for imaging electrical conductivity in EIT is discussed in Chapter 3. The dual modality scenario for characterisation of the three phase flow is then presented.

5.3.1 EIT

Figure 5-2 shows a 32-electrode EIT phantom. Electrodes are attached inside the phantom and directly contact with background. Normally, current injected to a pair of electrodes, in this chapter, adjacent method is applied. Voltages are measured at the rest of electrodes, therefore, one current injection can give 29 valid voltage measurements. The process is repeated until current injected to all adjacent electrode pairs. And then, the measurement is used for image processing.

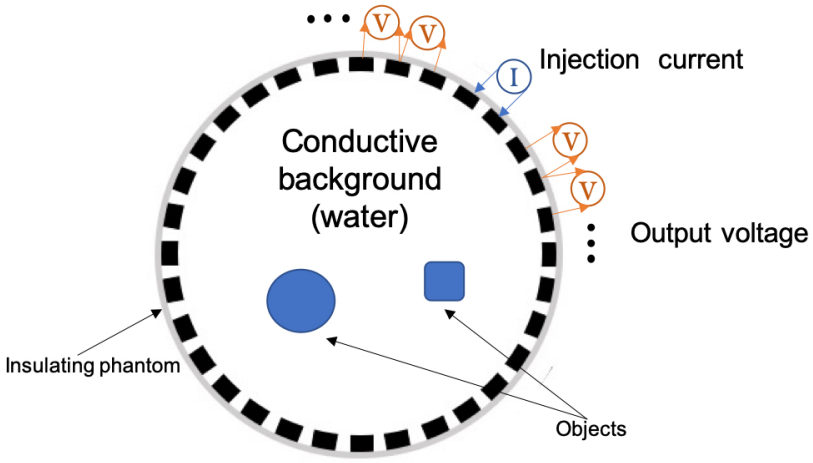

Figure 5-2: Measurement principle of a 32-electrode EIT system

5.3.2 UTT

In this study we applied an optimized linear inversion method for UTT, which is based on TOF signals.

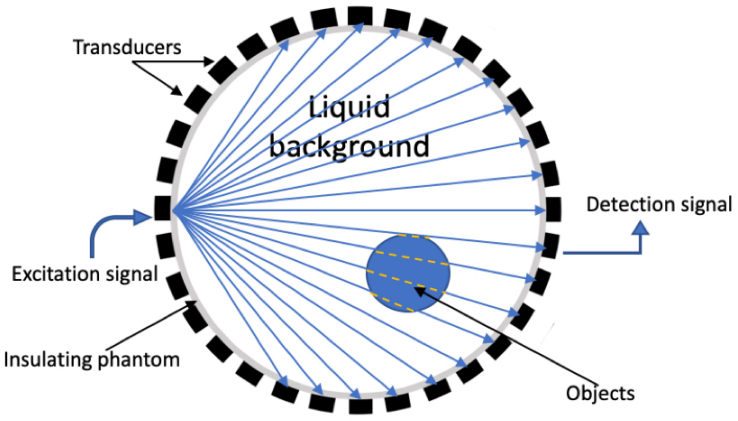

Figure 5-3: Measurement principle of a 32-electrode UTT system

TOF values are calculated by measuring the time of the first received most powerful pulse of the captured waveform. By enveloping the received signals and detecting the waveform's point of the maximum peak of amplitude, one can figure out the time that took to the biggest transmitted pulse to travel through the ray-path. Using the raw TOF data to compute sound-speed data, we conclude

getting the average sound velocity of every each one of the wave-rays. We use the formula [138]:

$$S = \frac{D}{TOF} \tag{5.1}$$

Where D is the distance of the travel-path of each ray and S is the computed average sound velocity. The sound speed of the m_{th} ray, $v_m (1 < m < M)$ of an acoustic wave that travels through the path l, between an emitter and a receiver can be expressed by the following path of a line. This line is expressed by the integral of the spatial distribution of the sound-speed of the domain:

$$v_m = \int_l V(l) dl \tag{5.2}$$

To algebraic reconstruct data, first of all, one need to discretize the domain. The equation below describes the reconstruction problem:

$$v_m = \sum_{n=1}^{N} W_{m,n} v_n \tag{5.3}$$

Where v_n is the sound speed that produced the n^{th} cell, $1 < n < N$ and $w_{m,n}$ is the weighted value that describes how much every specific wave-ray affects the domain, namely the pixels. These weighting values have been computed by an algorithm which checks the distance of the ray to the centre of the pixel. By treating the pixel as a circle, we achieved to reduce dramatically the computation costs of the process of assigning thee values [140].

A tomographic approach consists of many of these rays, whose amount depends on the angle of emission beam. All these equations of rays form a system of linear equations, the so-called forward problem. The measurement includes subtraction between reference and inclusion data for sound speed leading to the image of change of sound speed:

$$\Delta m = S \Delta v \tag{5.4}$$

5.3.3 Image reconstruction

To overcome some sparsity problems that can be occurred with the above method in UTT, a thicker wave rays are used for the sensitivity kernels to the width of the transducer (19mm). It is commonly known that the specific tomographic method is not capable of detecting and reconstructing objects lower in dimensions than the actual receivers' dimensions. Therefore a more uniform distribution of sensitivity values can be achieved. In Figure 5-4 at left, we present a sensitivity kernel and at right two full sensitivity maps. The middle one was computed by using a fan-beam angle of 90 degrees and the right one a full fan-beam angle of 170 degrees. We choose for our reconstructions the 90 degrees sensitivity matrix as it offers a better sensitivity over the centre of the domain. Figure 5-5 shows the sensitivity maps in EIT, which gives a high sensitivity near the boundary. Generally, UTT has uniform sensitivity as compared to the EIT which is very non-uniform with central area with weaker sensitivity.

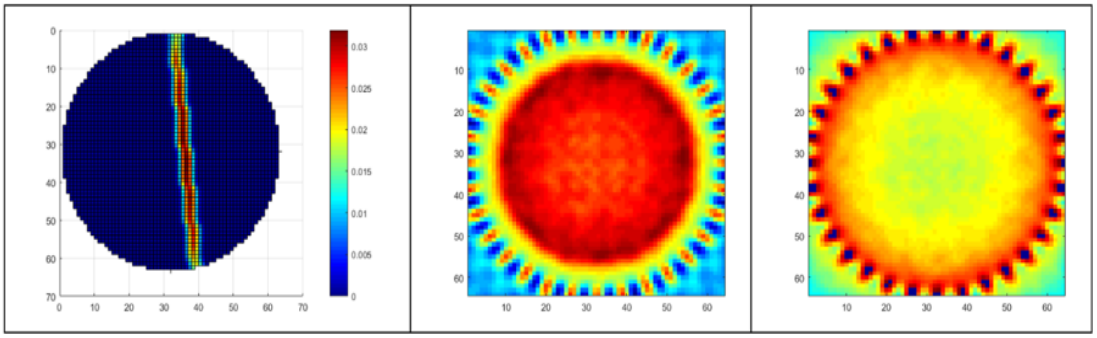

Figure 5-4: Left: UTT sensitivity map. Middle: Sensitivity matrix of 90 degrees of angle beam. Right: Sensitivity matrix of 170 degrees of angle beam.

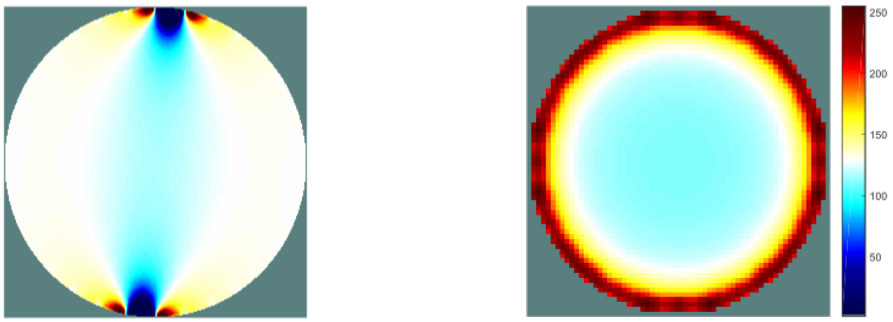

Figure 5-5: EIT sensitivity maps. Left: single injection. Right: full injection.

The singular value decomposition of the sensitivity matrix in UTT and EIT will help to understand the level of ill-posedness in each case and hence the level of regularization. Figure 5-6 shows the singular value distribution for the EIT and UTT, it is clear that EIT is severely ill-posed while the UTT has some level of ill-posedness. The need for sophisticated regularization in EIT is far more important than it is for UTT.

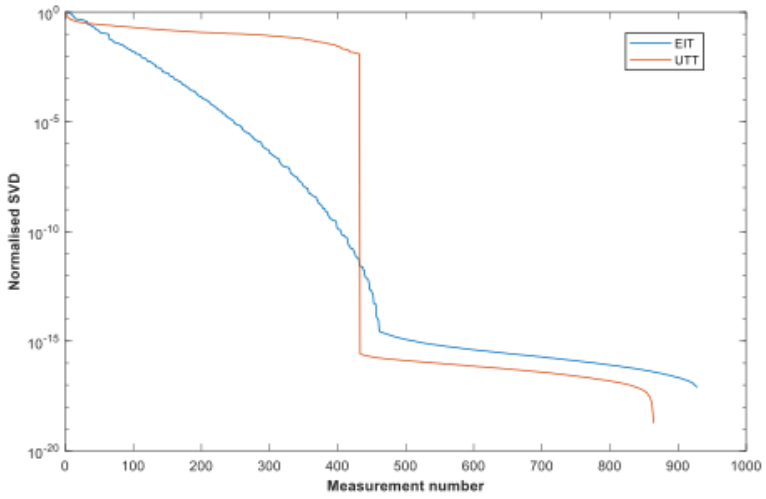

Figure 5-6: Singular value decomposition for EIT and UTT

A total variation algorithm is used for both UTT and EIT cases. In this work, the L_1-norm regularization term is introduced and the inverse problems are solved by the total variation (TV) algorithm [130]. The changes in conductivity and sound

speed using TV algorithm are:

$$\Delta\sigma = arg\min_{\Delta\sigma} \frac{1}{2}||S_C\Delta\sigma - \Delta\theta||^2 + \alpha||\nabla\Delta\sigma||_1 \tag{5.5}$$

$$\Delta x = arg\min_{\Delta x} \frac{1}{2}||S_U\Delta x - \Delta\tau||^2 + \beta||\nabla\Delta x||_1 \tag{5.6}$$

as introduced in section 3.3.4 where, α and β are the regularization parameters, ∇ is the gradient and $||\cdot||_1$ is the l_1-norm penalty term. A split Bregman based TV algorithm is used for both UTT and EIT [141].

5.3.4 Dual modality procedure

In water-dominated situation, EIT can be used for detecting non-conductive phase including both gas and oil, by solving the difference in voltage measurements. An image of conductivity distribution is reconstructed, as shown in Figure 5-7 top-left. Since the acoustic impedances varies in water and gas, but are similar in water and oil, the reconstructed image of UTT can be used for identifying gas phase like in Figure 5-7 top-right. To combine the information of these two reconstruction images, a water-dominated three-phase flow can be distinguished. These two procedures are independent, EIT and UTT can be performed at the same time or sequentially.

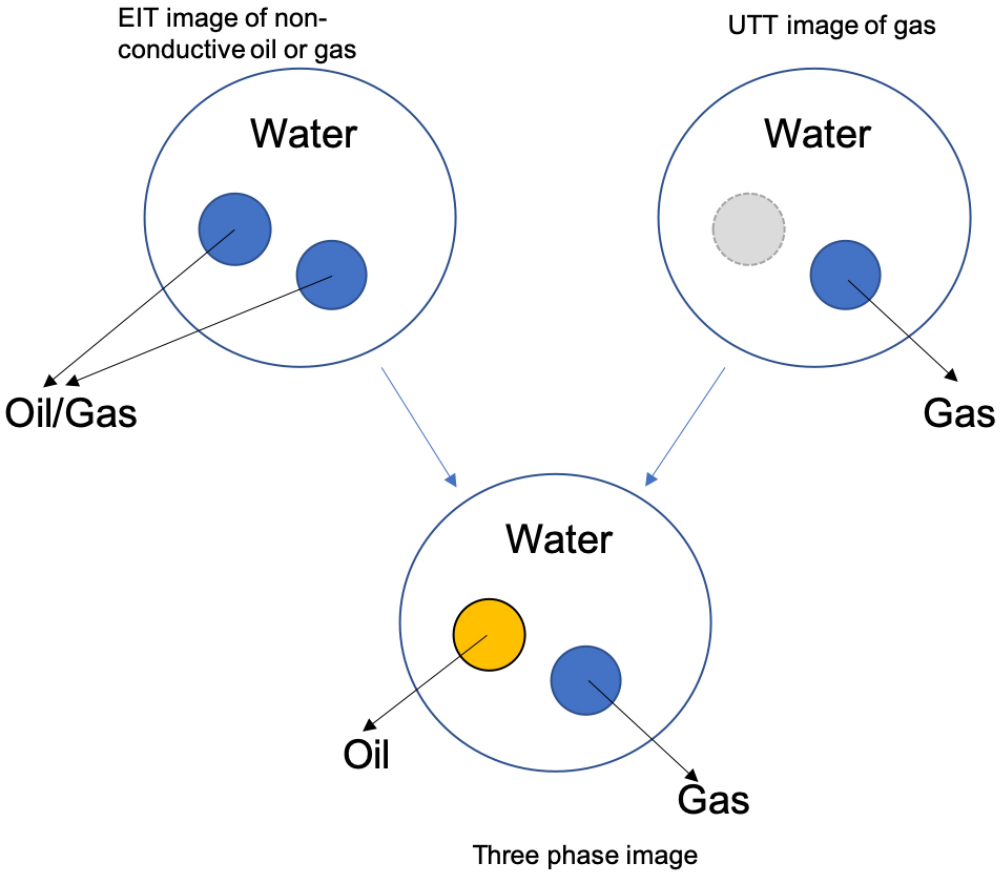

Figure 5-7: Sequence of three phase flow classification

The simulation results are presented in Table 5.3 using noise free and realist noise models. The conductivities and speed of sound of each phase are set as Table 1.1. A 7dB noise is added for EIT images and 15% mean value noise of differences is added for UTT images. Three different scenarios are created. As expected, non-conductive phases are clearly detected by EIT. Because of the high contrast in conductivities between water and oil/gas, noise has little effect on EIT results. However, noise makes significant impact on UTT images, due to the close sound speed between oil and water phase. The speed of sound in water and in oil are close, ideally, a shallow inclusion of oil phase should be found in all cases. But the reconstruction of oil phases can be easily affected when noise is introduced, which means the separation of oil from water can be difficult using UTT. Finally, the three-phase flow can be distinguished by combining these two sets of images.

Table 5.1: Simulation results for three-phase cases

		Case 1	Case 2	Case 3
		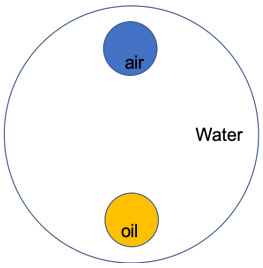	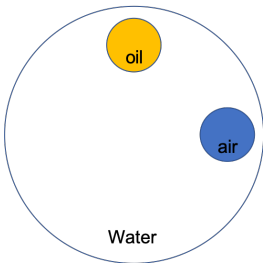	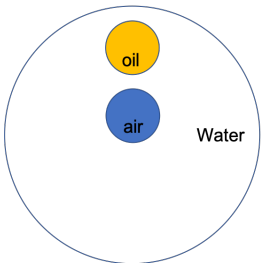
EIT	Noise free	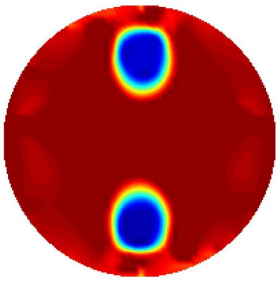	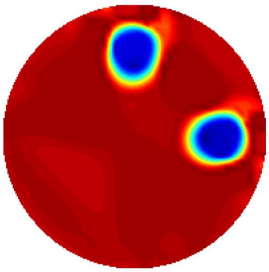	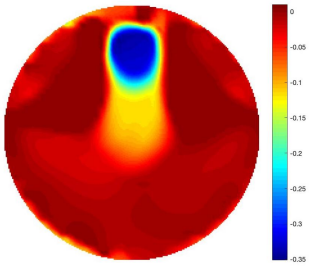
	With noise	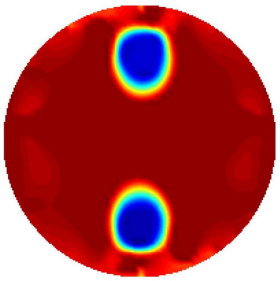	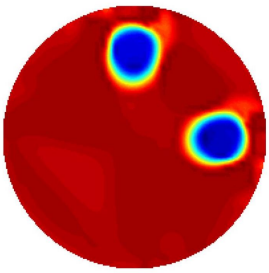	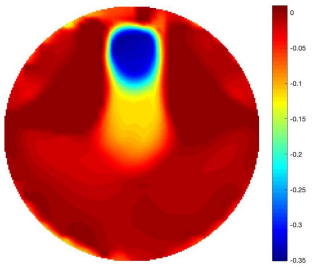
UTT	Noise free	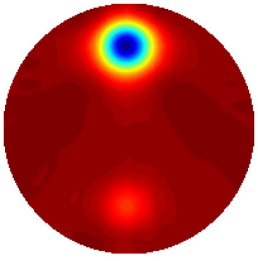	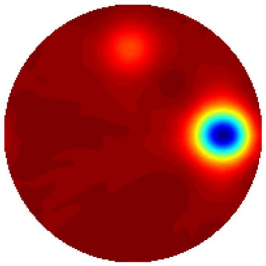	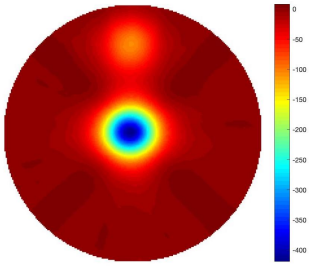
	With noise	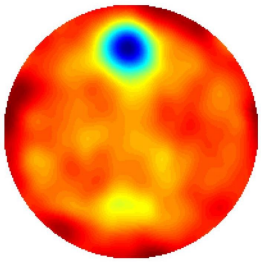	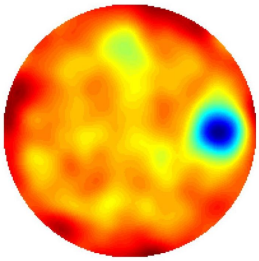	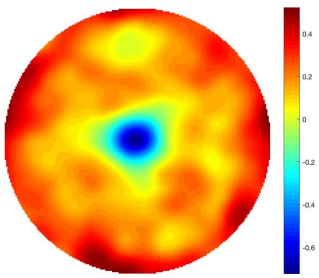
Classified	With noise	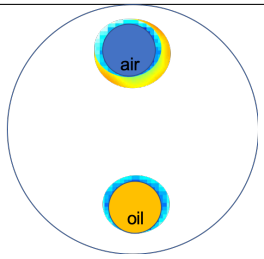	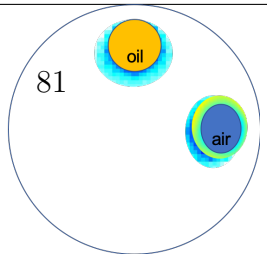	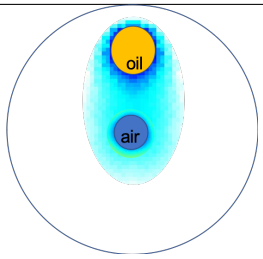

Data fusion

To achieve a robust three phase discrimination we developed a image fusion approach. Combining the information of the gas phase detection by UTT and the non-conductive phase detection by EIT, a three-phase image can be produced. An image fusion strategy is developed by using the following steps:

- i) In EIT reconstruction, there are totally 928 measurements of change in voltage due to 32 electrodes. The measurements are used in SB-TV to produce a 50×50 matrix, and this matrix is used to reconstruction a 50 by 50 pixels image with the value of each pixel matches the matrix. The value range of the image is depending on each case. And then, normalise each pixel value from -1 to 0, where -1 for non-conductive phase and 0 for the rest of domain.

- ii) Apply the same method to the UTT image where 864 measurements in each image, and the SB-TV is used to produce a 50 by 50 pixels image as well. After normalising the pixel values, -1 indicated for gas and everything else is 0 in UTT images.

- iii) Simply add two images together.

In the fusion image, if the sum of a pixel is 0 then it is the water phase in red, where the sum is -1 then it is the oil phase in green, and when the sum is -2 then it is the gas phase in blue. Table 5.2 shows the fusion images for all three cases, blue indicated gas phase and yellow to green indicated air phase as promised. As the experiments in this work are based on data from distinct phases, the above method works well, if a more inter-mixed phase is considered a more sophisticated strategy can be developed for this classification but following a similar approach. An Otsu threshold method was used for each sets of images [142] helping to produce image of EIT and UTT which includes -1 or 0 in their entries.

Table 5.2: Fusion images using proposed method for case 1 to 3

Case 1

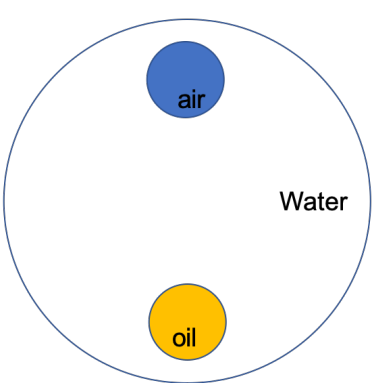

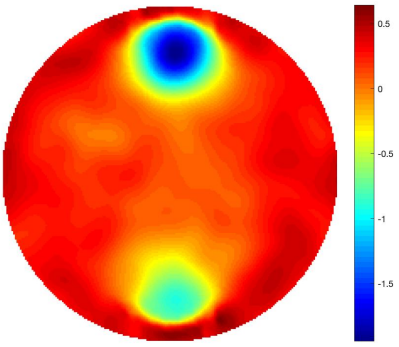

Case 2

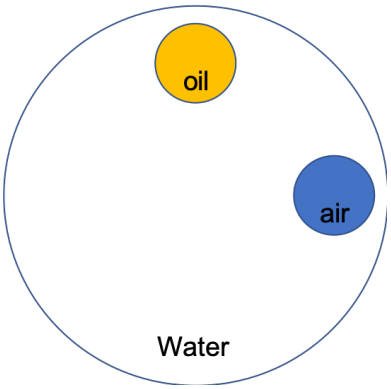

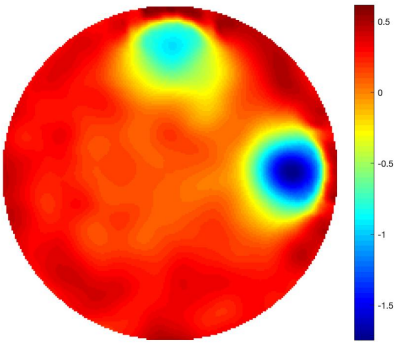

Case 3

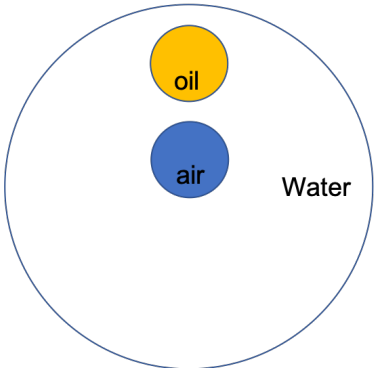

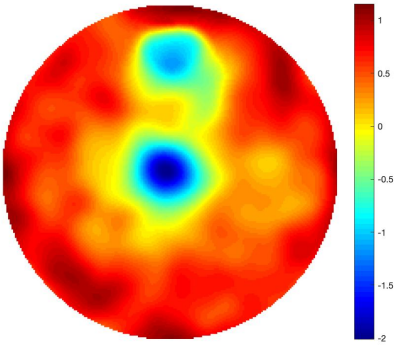

5.4 Experiments

5.4.1 Measurement system setup

The experimental system includes a combined sensor, which includes both the 32-electrode EIT sensor array and the 32-electrode UTT sensor array, and two separate measurement system (one is for EIT and the other is for UTT). The UTT array is vertically down below the EIT array. Basically, the UTT sensor system is previously made in the lab and I mounted the 32 electrodes for EIT system above the UTT sensors to form this dual-modality system. The EIT electrodes are made of copper strips and they are long enough for any water level, also can be easily connected to the measurement device. Figure 5-8 shows the experimental setup used in this study. Since we use EIT and UTT in separate plane it is possible to use 32 sensors. However, if we were to use them both in single plane then 16 channel for each would be more appropriate.

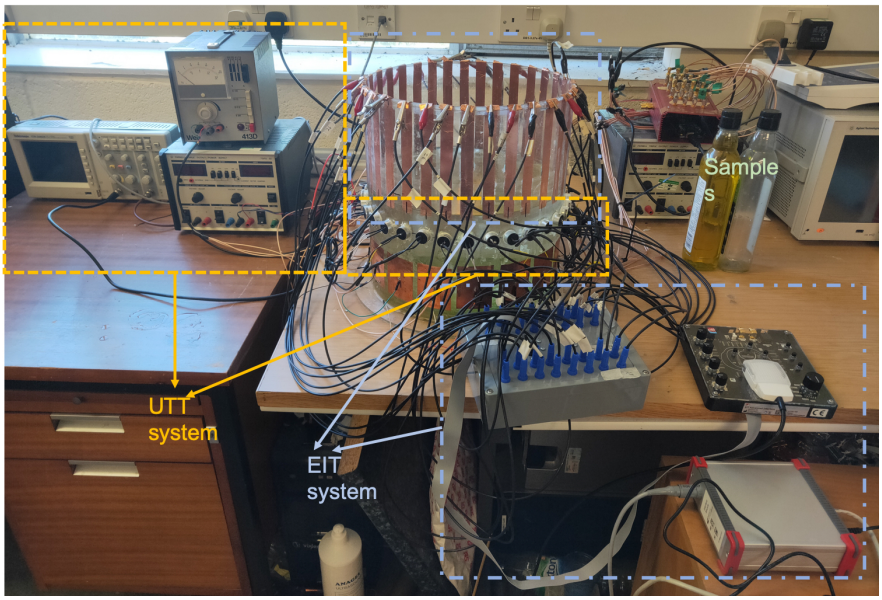

Figure 5-8: Experimental set up and EIT and UTT sensors and system

The UTT system includes a power supply, a self-designed control, calculation module and a computer. The power supply powers the control and calculation module. The control module controls the whole measurement process, realises the switching process for a whole measurement, generates and amplifies the excitation

signal and deals with the received signal to obtain TOF values. The computer implements image reconstruction and provides the final images.

The EIT measurement system used in this experiment is designed by SenTec AG [143]. It consists of a SensorBelt, a smart SensorBeltConnector and a power supply. The SensorBelt directly connects 32 sensors with the smart connector, while the smart connector controls all injection and measurement. The data is acquired and processed with SenTec EIT Monitor Software (STEM Software) [143], the interface of the STEM is shown and explained in Figure 5-9.

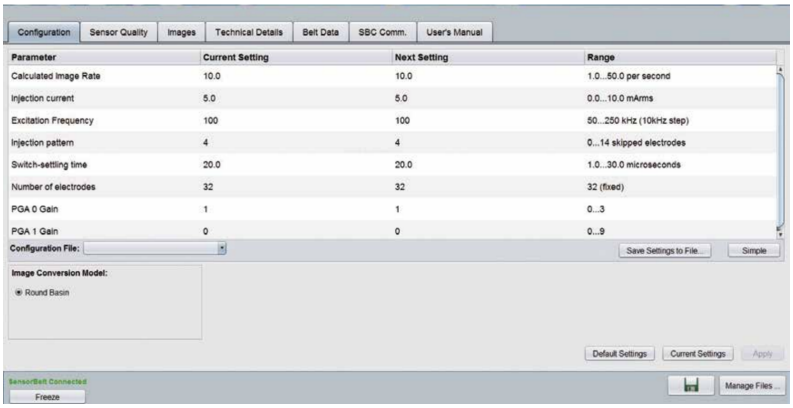

(a) Configuration: various operational parameters such as excitation frequency, injection pattern, injection current and image rate can be set here.

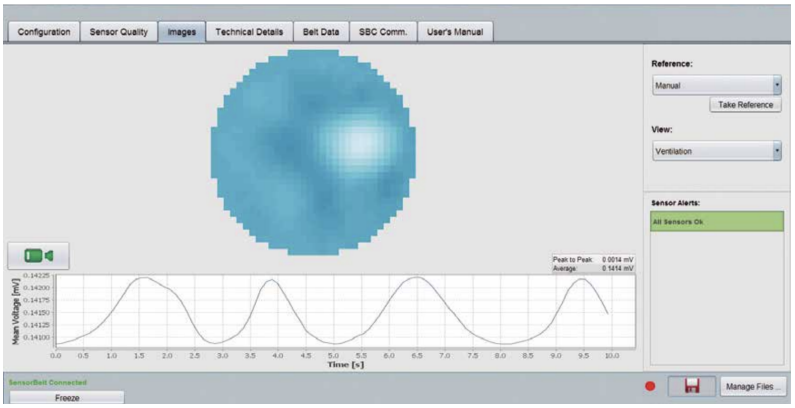

(b) Reconstructed image window: real-time reconstructed image is shown here and it can be recorded; on the bottom the mean voltages is displayed.

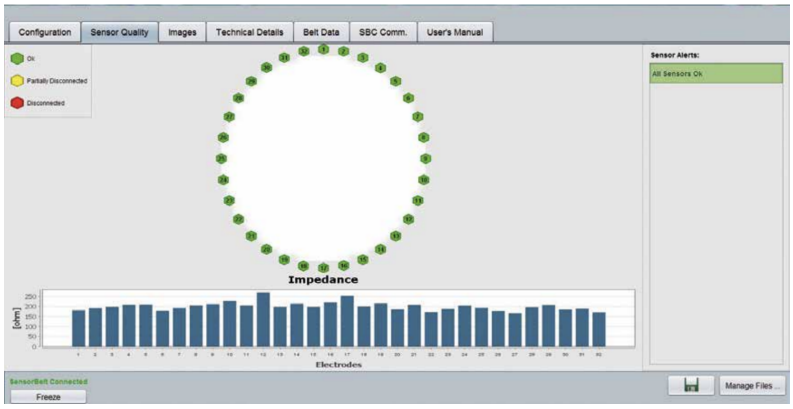

(c) Sensor quality: the connection states of each of the 32 electrodes is visualized in green (connected), yellow (partially connected) or red (disconnected), and also the contact impedance is displayed.

Figure 5-9: Screen shots of the STEM Software [143]

The inner and outer diameters of the tank were 280 mm and 300 mm. The excitation frequencies of EIT and UTT were 200 kHz and 200 kHz, respectively. One plastic bottle filled with olive oil used for representing oil phase and another empty bottle (air) in same size represented gas phase in all cases. In EIT, the only reliable imaging property is the electrical conductivity. A plastic bottle filled with olive oil can be represented as oil phase because they are all non-conductive. The same for air and gas. For UTT, TOF depends on density. The difference between speed of sound in water and speed of sound in oil is smaller than the difference between speed of sound in water and speed of sound in gas, as shown in Table 1.1. Therefore, the experimental set up can model a pipeline flow.

5.4.2 Results

Table 5.3 clearly presented reconstruction images in both EIT and UTT for 5 different scenarios. These 5 cases are designed to show the feasibility of EIT and UTT duel-modality performance in: a) oil and air phases are far away to each other and both near boundary; b) oil and air phases are close to each other and one of them near boundary; c) oil and air phases are at same distance from the boundary. EIT images present both oil and air phase in blue, the colour bar present relative conductivity from 0 to -1, where deep blue represents non-conductive. Meanwhile, UTT images clearly show the position and the size of the air phase. The colour from blue to red presents the relative speed sound in each phase from low to high correspondingly.

Table 5.3: Experimental imaging results of EIT and UTT for three-phase cases

	True cases	EIT images	UTT images	Characterisation images
1	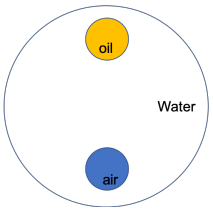	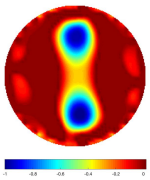	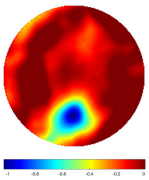	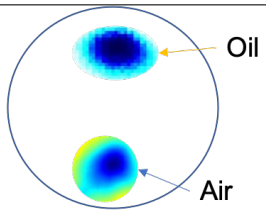
2	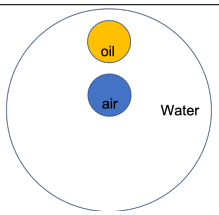	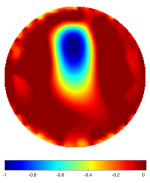	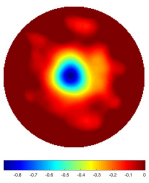	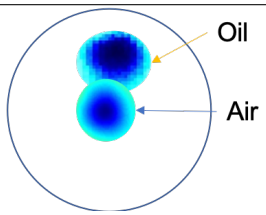
3	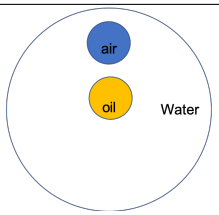	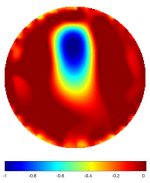	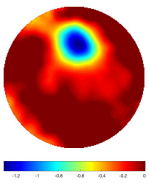	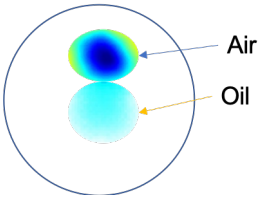
4	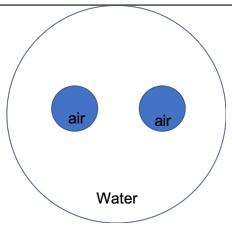	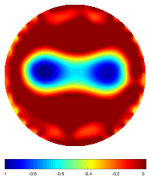	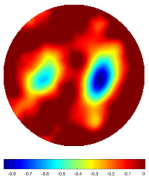	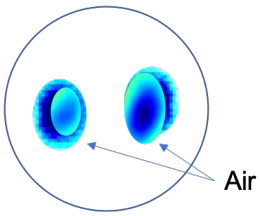
5	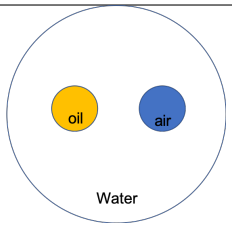	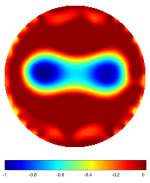	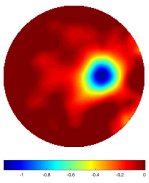	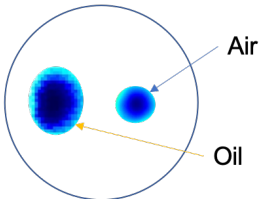

In previous research, EIT shows good performance and potential in flow industrial and other applications [144], [122]. Images obtained by EIT are generally good. In case 2 and 3, EIT images can clearly detect one phase near boundary and show in deep blue, but the other phase can still be seen in shallow blue and blurry. This is because EIT always has a high resolution near the boundary and decreasing forward centre. Therefore, in these cases, three-phase image can be

compromised by the limitation of EIT when oil/air phase is in the centre. Hence, non-conductive samples in the centre may not be imaged or separated, especially when they are very close.

UTT data is noisier than EIT in this work, this may because the speed of sound is sensitive, any pollution in the water can compromise the time measurement. Moreover, 32-transducer system increases the complexity in image reconstruction, but on the other hand, it provides high resolution in both systems. Referring to figure 5-6, the condition of UTT sensitivity matrix in reconstruction is slightly ill-posed compared to severely ill-posed EIT imaging. This makes EIT highly dependent to the image reconstruction and regularisation parameters. Additionally, the UTT has almost uniform sensitivity, but for EIT it is highly position dependent. This is shown clearly in cases 2 and 3, where simultaneous reconstruction of two inclusions next to each other with EIT is challenging. UTT is also slightly more robust in the central area and has some resolution degradation near to the boundary. EIT has better image resolution in the boundary area and less so in the central area. This gives UTT and EIT an additional synergy in terms of area of imaging.

The three-phase images using proposed image fusion strategy are shown in Table 5.4. Where three different colours values indicated three different phases, -2 represents gas phase in blue, -1 represents oil phase in green-yellow and 0 for background water phase in red. In case 1, 4 and 5, fusion images are clear represent three different phases as expected. They noise may not be eliminated, but the center of the samples are clearly imaged in correct position. However, fusion images fails in Case 3, this is mainly due to the limitation of the current EIT system, the samples in the centre are hard to be imaged clearly, and it is the oil sample which can not be seen in UTT image either. Hence, this exposes the limitation of this dual-modality as well, where the system may fail when the oil phase is in the centre area.

Table 5.4: Fusion images using proposed method for experimental studies

	True case	Fusion image
Case 1	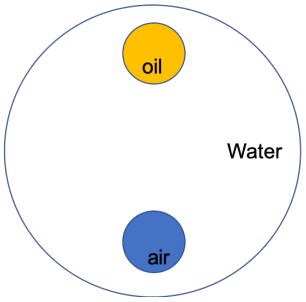	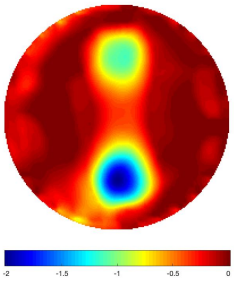
Case 2	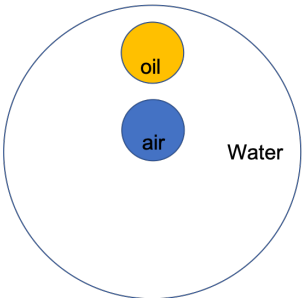	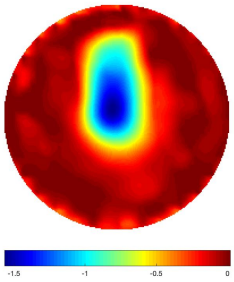
Case 3	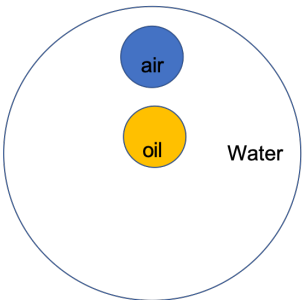	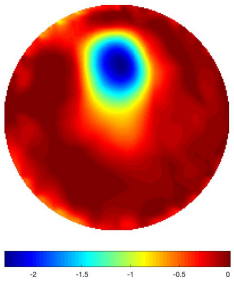
Case 4	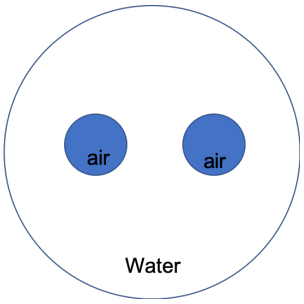	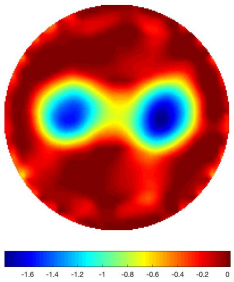
Case 5	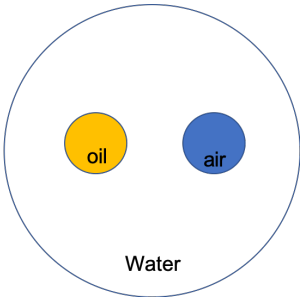	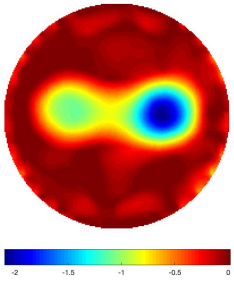

Overall, these results demonstrate successful outcome for three phase flow characterization when dealing with distinct phases of water oil and gas using EIT and UTT dual-modality system. Figures of merit are plotted, amplitude ration (AR), resolution (RES) and shape deformation (SD) was selected from GREIT image quality parameters as introduced in Section 3.4 [136] to evaluate the performance of the images. AR measures the ratio of image pixel amplitudes in the inclusion area to that in the reconstructed image as shown in Figure 5-10; RES measures the size of reconstructed inclusion as a fraction of size of entire imaging region in Figure 5-11 and SD in Figure 5-12 shows part of reconstructed images that does not fit in a circular shape. The smaller of these values means a better image. The performance of fusion images is generally better than EIT images in all cases but not good as UTT since the UTT has more uniform sensitivity matrix and less ill-posedness. In other words, this dual-modality not only to distinguish three-phase, but also enhanced EIT resolution.

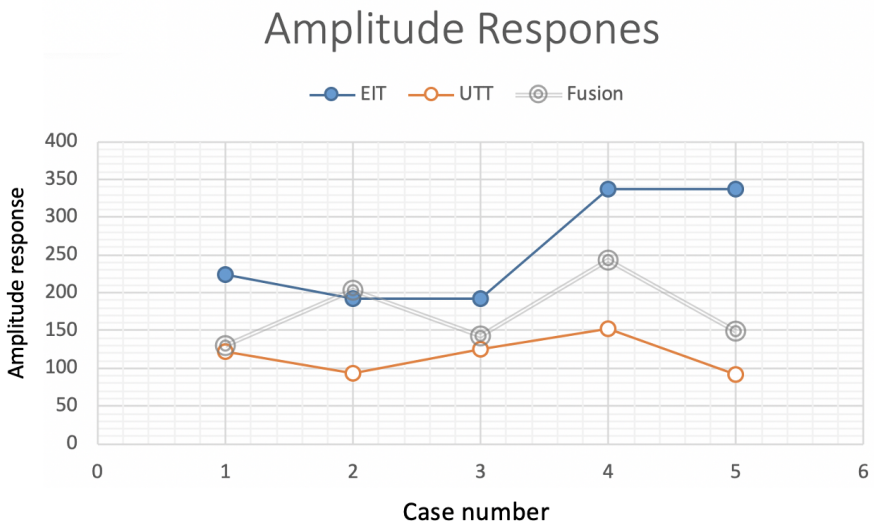

Figure 5-10: Amplitude response for case 1 to 5

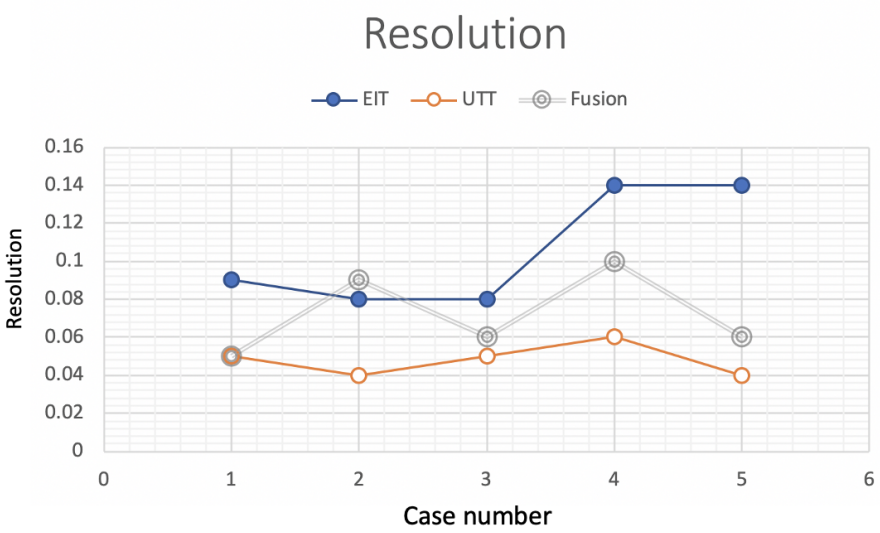

Figure 5-11: Resolution for case 1 to 5

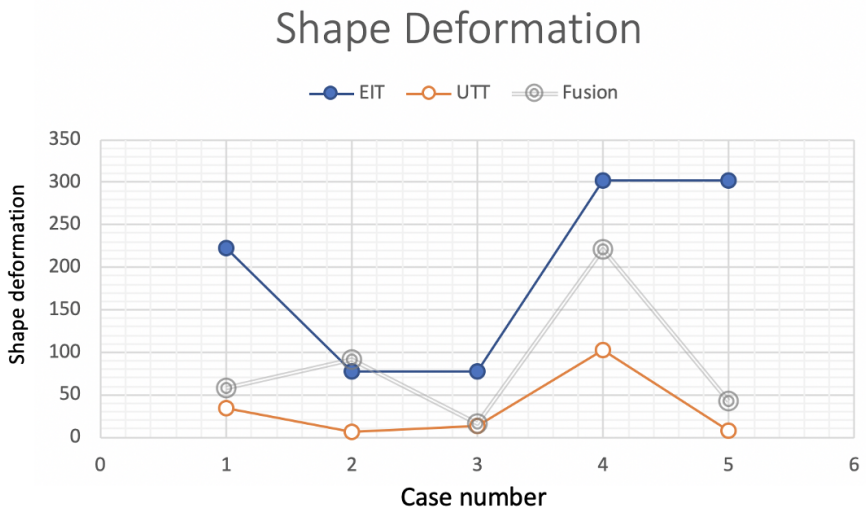

Figure 5-12: Shape deformation for case 1 to 5

5.5 Conclusion

This chapter introduced a novel three-phase material imaging and characterisation using a combined transmission mode ultrasound tomography and an electrical impedance tomography. EIT is used to identify non-conductive phase which either oil or gas phase and hence UTT is used to identify air phase. Several simulation studies and in lab experiments were established. And a image fusion method has developed to generate the three-phase image. The results demonstrate successful characterisation of these three-phase of oil, water and gas in water dominate cases, where providing the solution to the major challenge of three-phase in water background. Hence, three-phase images are produced using proposed image fusion method where three different colours indicate different three phases. For now, this work is only demonstrated in a static situation since it is a new combination and it is the fundamental work to see the capability of this dual-modality. This successful characterisation work of the system indicated it has the potential in imaging a flow in the future.

Chapter 6

Dynamic fabric EIT with deep learning

6.1 Introduction

EIT has been used as an imaging modality for monitoring in many fields of engineering. This is mainly because of the relatively low capital cost, non-invasive data collection and relatively good temporal resolution [145], [146]. Instead of the human body or other target, if a conductive material that will respond to local conductivity or permittivity changes is used, a pressure mapping imaging system or a touch sensing sensor can be created. Sense of touch is a major part of man's communication with their environment. Artificial skins can help robots to have the same sense of touch, especially for their social interactions. And also there is a need of extending the functionality of the skin to be dynamical where will enable the EIT based skin to work as an interface allowing social interaction with the robot. This Chapter presents a dynamical pressure mapping sensing using piezo-resistive fabric to represent aspects of the sense of touch. In past few years EIT is considered to be able offer a good alternative for artificial skin in particular for its ease of adaptation for large area skin compared to individual matrix based sensors. The EIT has also very good temporal performance in data collection allowing for monitoring of fast responses to touch stimulation, enabling a truly real time touch sensing. Electromechanical responses of a conductive

fabric can be exploited using EIT to create a low cost and large area touch sensing. Such electromechanical properties are often very complex, so to improve the imaging resolution and touch visibility, deep learning was used in addition to the state of the art spatio-temporal imaging algorithm. This section demonstrates a step towards an integrated seamless skin with large area sensing in dynamical settings, closer to natural human skin's behaviour. For the first time a dynamical touch sensing are studies by means of a spatio-temporal based EIT imaging on a conductive fabric. Various dynamic experiments has performed and improve image quality using deep learning for the first time. The experimental results demonstrated the successful results by a combined deep learning with dynamical EIT imaging results in single and multiple points of touch. This chapter is based on the published journal paper [49].

6.2 Measurement system and method

EIT aims to reconstruct image of a conductivity distribution inside the testing object. EIT systems measure boundary voltages according to constant, low frequency and multiple injection currents to reconstruct cross-sectional images of the conductivity distribution [147]. A typical fabric EIT system is shown in Figure 6-1. All the proposed EIT systems are based on the basic methodology which are: 1) the data collection of a set of independent transfer electrical impedance. 2) The stable solutions of forward and inverse problems in order to reconstruct images with high quality [50]. To reconstruct EIT images in general geometrical settings, all functions are required which are described in details: a system for measuring the surface geometry, a mesh generator to produce a mesh based on the surface information, code for computing the finite element approximation and an algorithm to solve the inverse problem. Also, tools to display the results and also to analyse the images are required [148].

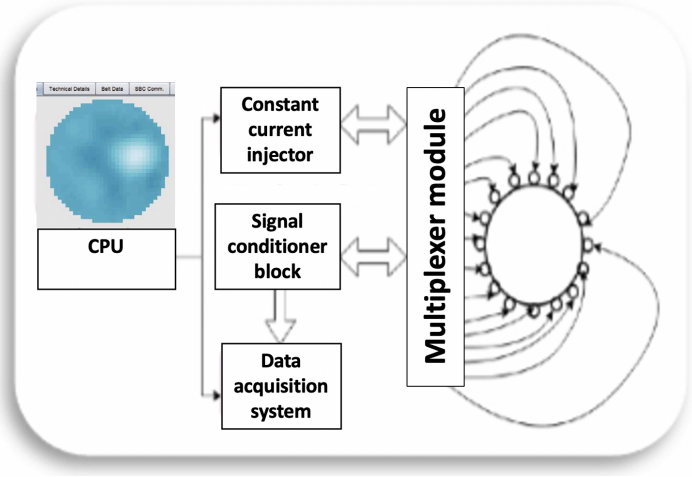

Figure 6-1: Typical fabric EIT system structure diagram

6.3 Experimental results

This work focuses on a Pressure Mapping Imaging based on EIT. The special sensor used is built up by a conductive fabric and a wooden circle frame with 16 electrodes on boundary as shwon in Figure 6-2. The conductive stretchable fabric LTT-SLPA used in the experiment was manufactured by Eeonyx Corp, made by stretchy nylon/spandex and coated with a long-lasting conductive formulation, which gives a tunable surface resistivity in the range of 10^4 to 10^7 ohm/sq.

Two of the electrodes are used to input a constant current into the conductive fabric, other electrodes will get an initial voltage reading. And then, pressuring the conductive fabric over the circular sensor area, electrodes on boundary will generate a new voltage reading. Using this new reading minus initial voltage reading to get voltage difference (ΔV). The voltage difference is used to image pressure map by MATLAB processing. We conducted several experiments and two sets of experiments are shown here for comparative study.

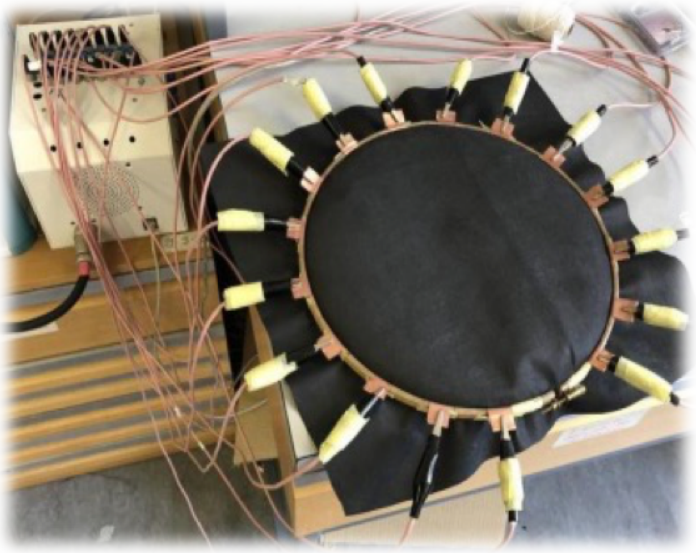

Figure 6-2: Dynamic fabric EIT sensor array

6.3.1 One-object test

In this test, one finger was used to apply the pressure on fabric over the circular fabric sensor area (as shown in figure 6-3a). The background data was collected first, and then apply force from first test point. Due to the lower frequency chosen 5 kHz. The pressure point was moving anticlockwise near boundary and moving towards center after one turn. In this case 439 sets of scan data were collected. Figure 6-3b shows 21 snap of reconstructed images for a single finger touch going anticlockwise and from frame 13 moving towards top left and then through the center.

(a)

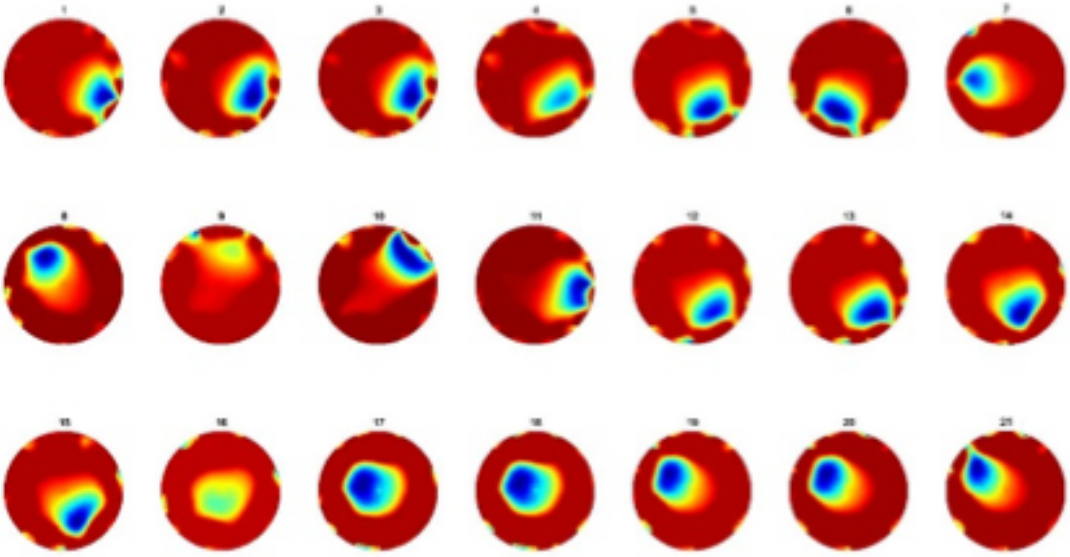

(b)

Figure 6-3: A single pressure point moving counter clockwise and then diagonally towards the center

6.3.2 Two-object test

In this experiment, the same approach as test one, two pressure points applied at the same time and moving clockwise. In this test, two fingers were used as a compare of last test in not only the inclusion numbers but also the size since two fingers can give larger contact area of pressure. In this case 273 sets of data were imaged. Figure 6-4 shows 21 snaps of reconstruction images that clockwise movement of two finger touch points.

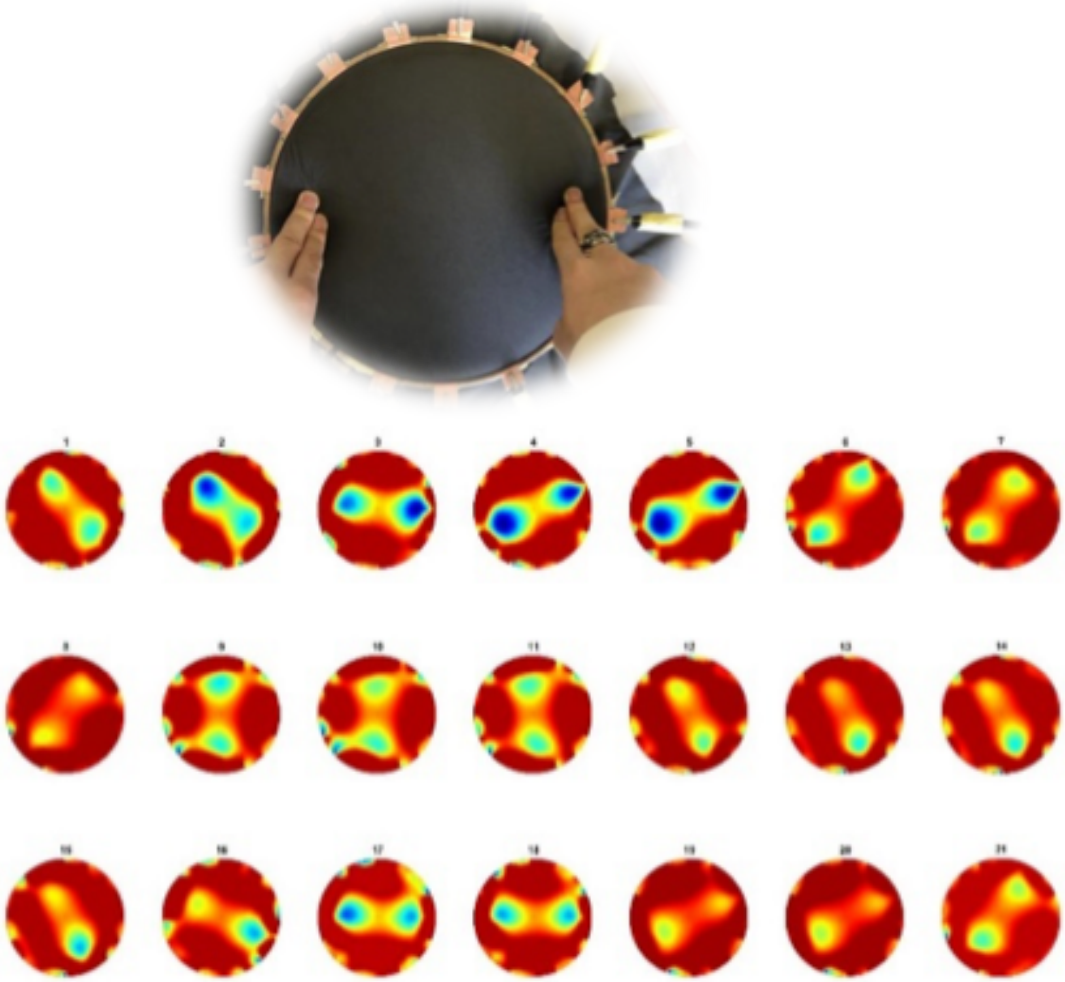

Figure 6-4: Double pressure points rotating clockwise

Temporal image reconstruction using state of the art TV algorithm performed very well, taking advantage of time correlation between frames of data. This includes ease of detection of pressure points in central area of fabric, which is always seen an issue for large area fabric EIT testing. Also, this dynamical image extends the functionality of fabric EIT as the robotic skin, which is the essential ability that allowing social interactions in robotic.

There are still some artefacts remaining in those images and if we revert to a single frame by frame reconstruction (not taking advantage of temporal correlations), then these noises are more severe. Next section aims to address these issues with

help from arterial intelligent.

6.4 Image processing – Deep learning

6.4.1 Deep convolutional neural network

Figure 6-5 shows a reconstructed image and a typical thersholding, the noise in the initial image has been reduced generally, but a systematic error around the boundary due to the electrode movement can not be eliminated so far.

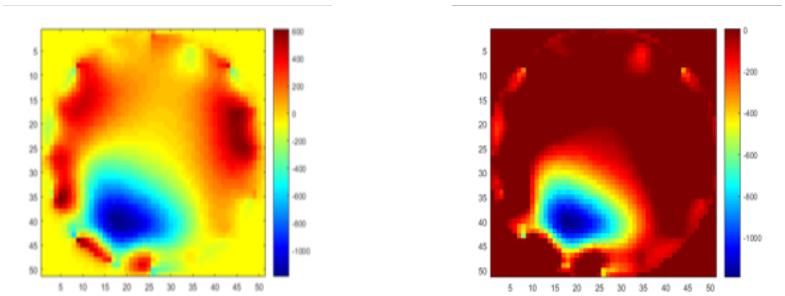

Figure 6-5: Passage from a raw EIT image (left) to a thresholded image (right)

The aim is to remove the electrodes artefacts which can be done with deep convolutional neural network. Deep learning has attracted much concern from the academic circles and industrial circles because of its powerful learning ability in recent years [149], [150], [151], [152]. Deep learning is effective at digging the abstracter and abstracter feature representation from original input data, and the representation achieves a favorable generalization ability and has overcome some problems considered difficult to solve in past artificial intelligence [153], [154], [155], [156]. In general, a neural network consists of an input layer, a set of hidden layers formed of neurons and an output layer. A neuron contains all input information x, where x is a vector, interact with weights w (learnable parameter). The result of weighted sum xw passes through an activation function f. The output of the neuron is thus $y = f(\sum x_i w_i)$.

In the case of a classical neural network, each neuron takes all values in previous layer as input like in Figure 6-6. This means for a network with an image as input and made up of approximately 10 to 20 layers, there will be millions of

weights to learn at the same time and the number of calculation is huge. In fabric EIT images, the size is modest and yet the number of calculations remains very important. Which convolutional neural network is rather good when treating images due to the lower calculation complexity by parameter sharing, neurons do not take into account of all pixels as input. And this type of calculations considers neighborhood in images [157].

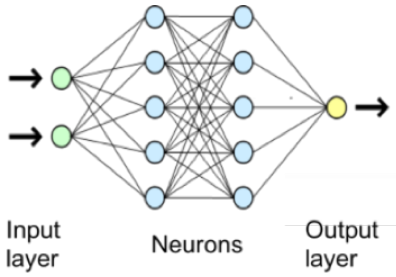

Figure 6-6: A regular 3-layer neural network

A learning base is created by an input of a set of noisy images and an output of all cleared images. The network is updated with the information through learning, which is modifying weights w until reaching the desired result, and then, a set of unreleased images can be sent to the network to improve visibility. The learning base has to be as robust as possible. In our case, the learning process can be explained as following steps:

i Feed the network with input, the input is a set of original images representing pressure point that travel all accessible areas of the fabric with a significant noise related to the electrodes.

ii Create the 'perfect' clean image. A example of this 'perfect' image is shown in Figure 6-7. A boundary suppression applied to remove electrode's noise, and large size of blobs were kept only values greater than 55% of the maximum amplitude since even a small pressure point can produce a large blob due to the deformation of the material. In additional, small blobs that less than 15 pixels of area was removed.

iii Feed the network with output, the output is a set of improved images that we want, in our case, is the 'perfect' images created in last step.

iv Let the network to train learnable weights w.

After the training finished, any set of noisy data can be feed in the network, and the output will be denoised images that learned with parameter weights w.

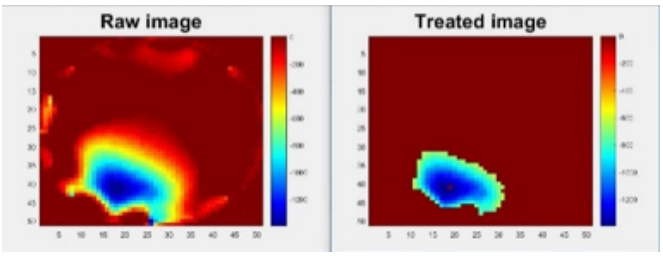

Figure 6-7: A set of raw and treated 'perfect' image.

In this image training, a U-net convolutional neural network implemented with Tensorflow (https://www.tensorflow.org/) is used, the structure of this network is shwon in Figure 6-8. This type of network is commonly used in biomedical image segmentation, also has good results during classification problems and image reconstruction [158].

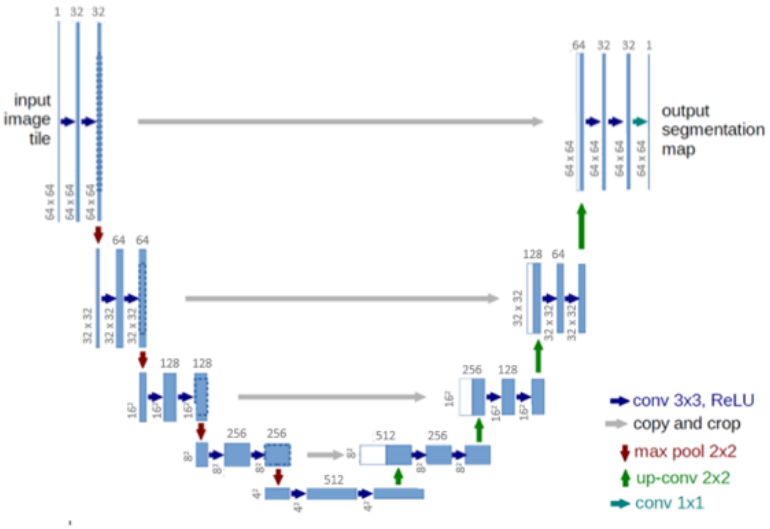

Figure 6-8: Structure of a convolutional neural network of U-net architecture

The training result of this U-net convolutional neural network can be evaluated by two approaches:

- With the formula of mean squared error: $MSE = E[(image - image_{`perfect'})^2]$, which indicates how noisy the data is.
- And simply by examining the final image, compare them with the raw images to see the clarity.

6.4.2 Result

Training 1

The one object (single pressure point) data set training from experiment one is composed of 439 pairs of images where one pair of image contains a raw image and the image wanted (the 'perfect' image), they are the input and the output of the training as described in last section. Once the training is done, which means the network has learned the parameter weights w, the next step is to send the new images set with noise artefacts into the neural network, and the output will be an image set hopefully improved. The proposed U-net network could be simplified to a smaller network as the overall task in this problem of 2D and time is less demanding than some other challenging problems U-net can deal with. But since we are using this existing U-net, the training time of our data set will be longer. To help understanding this training process, a flowchart is shown in Figure 6-9, and the training result is shown in Figure 6-10.

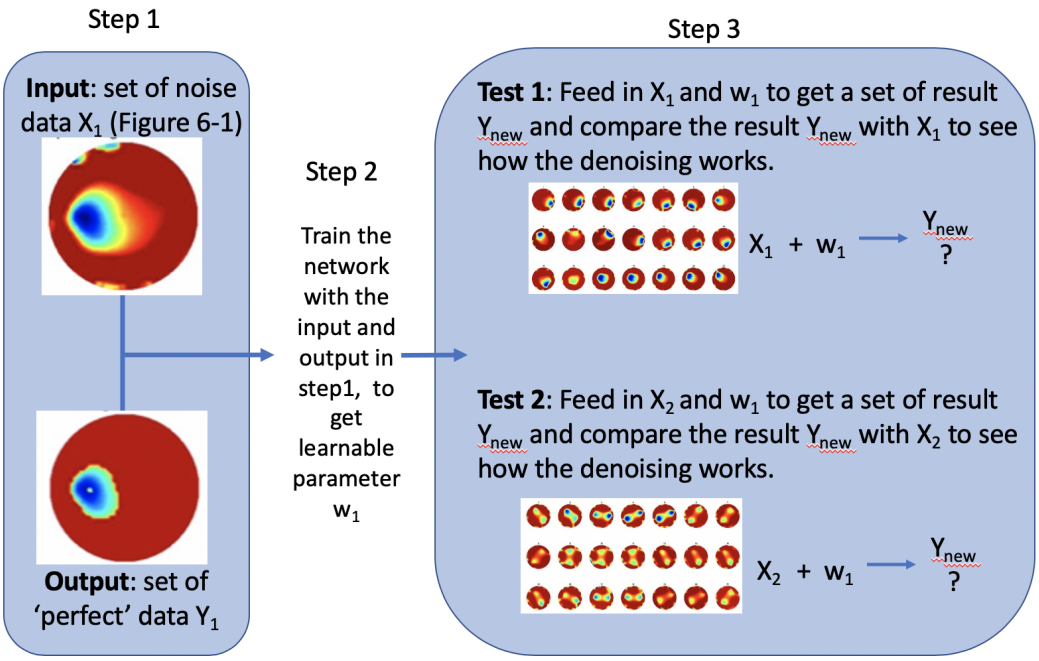

Figure 6-9: The flowchart of the training 1 process

The test of the network was done with the initial training data since almost each possible position is taken in this set, the set is exhaustive. Training results of X_1 are shown in Figure 6-10, electrodes noise is almost suppressed, the clarity of 21 corresponding frames in Figure 6-3b are greatly improved. The pressure points are clearly detected, and they are almost near 'perfect' images since the test data set is the same as the input of training set. And also the MSE of this test in Figure shows that the output (denoised) images are nearly 0, but not 0, which proofed that the test processing is not just simply copy the result in training.

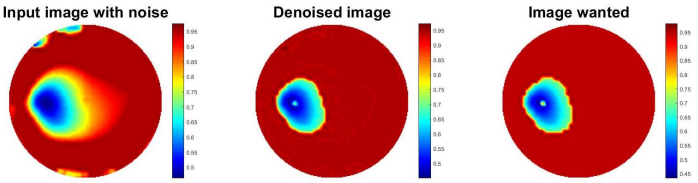

(a)

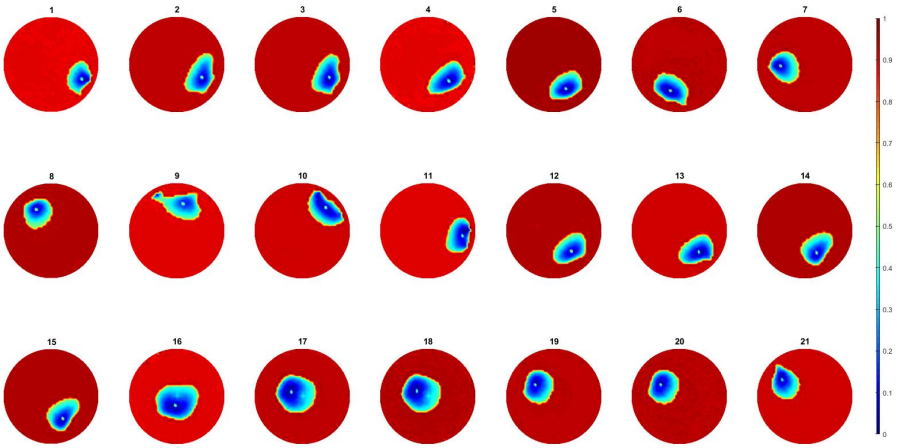

(b)

Figure 6-10: (a) One frame of single pressure point test and (b) 21 corresponding frames improved (Y_{new}) images when one object test (X_1) through the network trained with one object dataset (X_1 with w_1)

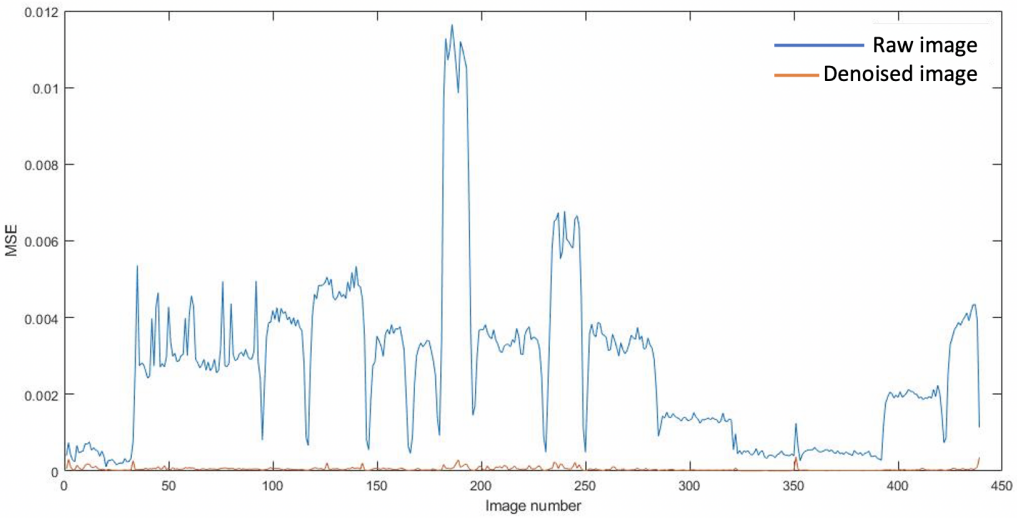

Figure 6-11: Comparison of MSE at the raw image in blue (before training X_1) and the denoised image in orange (after training Y_{new}) when the network is trained by one object dataset (X_1 with w_1)

Second test to check the robustness of the learning is to see how two objects images are improved through this training network, which input of this test is the images in Figure 6-4 from experiment two.

Results are shown in Figure 6-12, compare to the images before processing in Figure 6-4, pressure points are clearly detected, most noise caused by electrodes and fabric deformation are eliminated. Also to be noted that separation between objects is very well observed leading to better resolution. To evaluate how good the image has been denoised, a set of 'perfect' image also been produced for comparison. MSEs are calculated in Figure 6-13 where the input is the raw data of two objects images and the output is the two objects images that been denoised, the error of the output has been reduced by more than half.

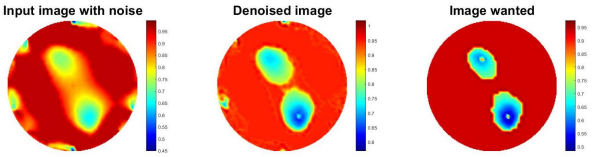

(a)

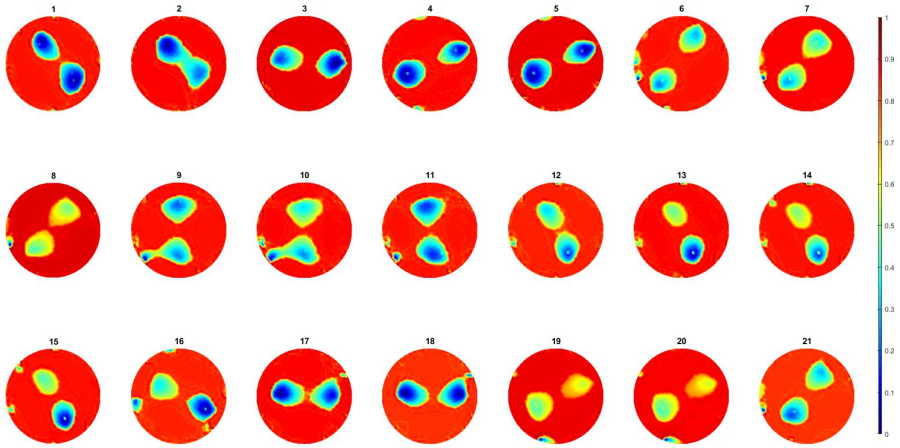

(b)

Figure 6-12: (a) One frame of two pressure points test and (b) 21 corresponding improved images (Y_{new}) obtained for two objects (X_2) passed through a one object trained network (X_1 with w_1)

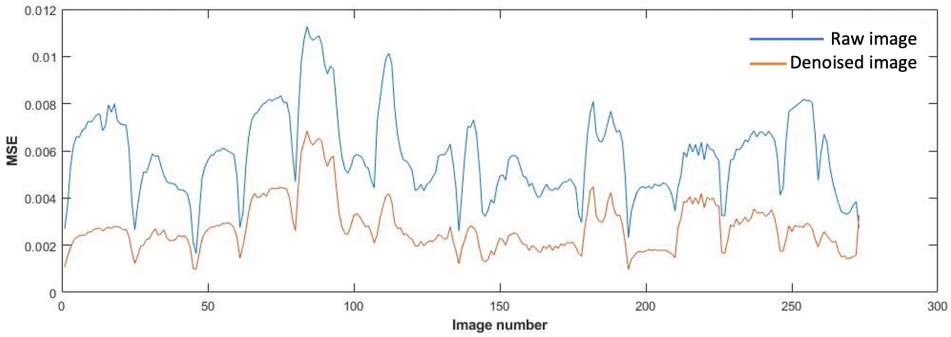

Figure 6-13: Comparison of MSE at the raw image in blue (before training X_2) and the denoised image in orange (after training Y_{new}) when the network is trained by one object dataset (X_1 with w_1)

Training 2

The other approach is to train the network with two objects images. A flowchart of how this training has been conducted is shown in Figure 6-14.

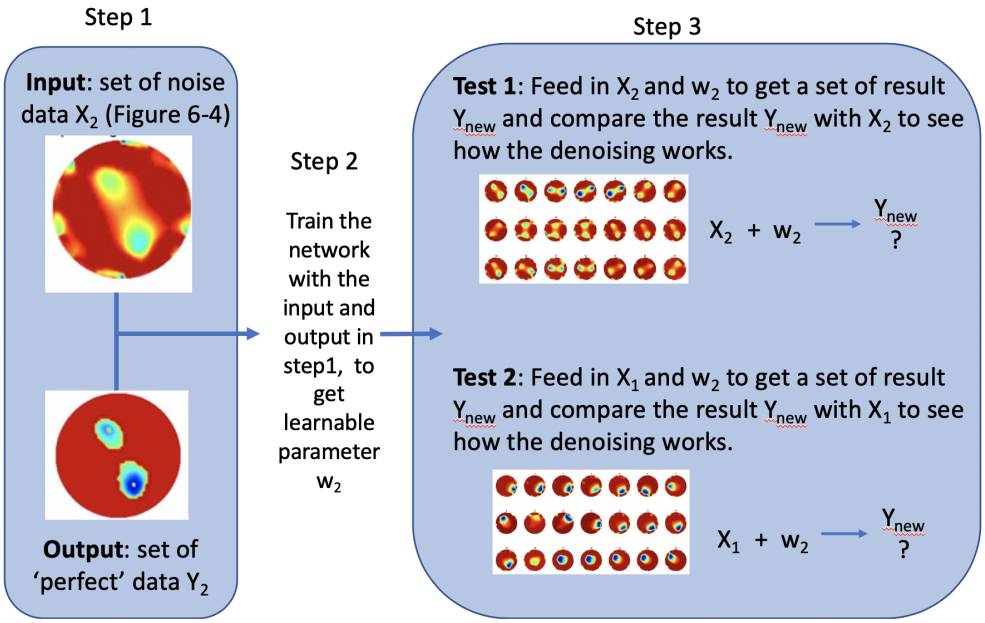

Figure 6-14: The flowchart of the training 2 process

In this experiment the dataset of training was using the second test set in last section, composed of 273 pairs of images, from two-object experiment. Once the training done the first test was to look at the improvement of image quality for two objects images.

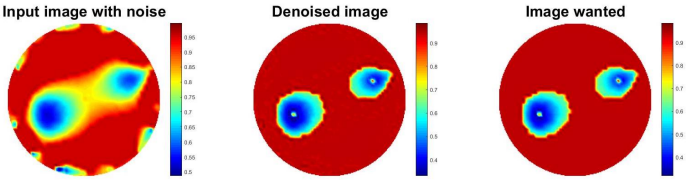

(a)

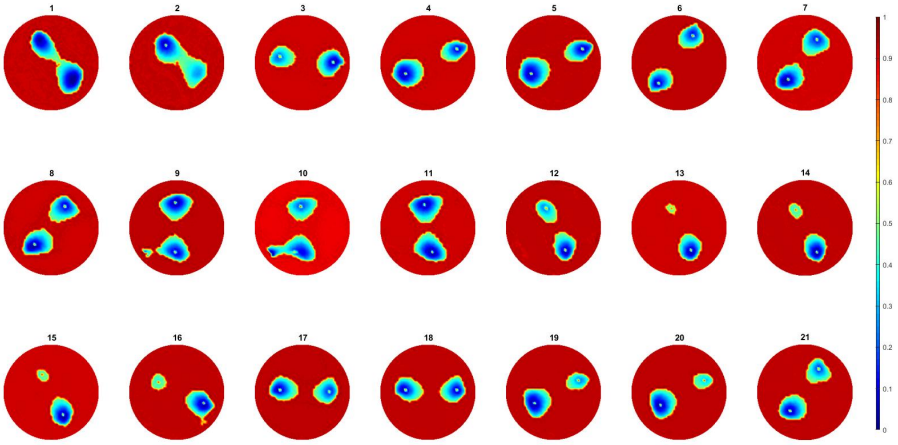

(b)

Figure 6-15: Improvement of two objects test (Y_{new}) for two objects raw images (X_2) passed through two objects trained network (X_2 with w_2)

Results are again really good, shown in Figure 6-15, electrodes noise is mostly removed and separation between objects is well done. The MSEs in Figure 6-16 in this test are almost 0 after about 30 frames since the test images X_2 are the same as training image X_2. Which is an interesting observation that can reflect the training network has learned learnable parameter w_2 in about first 40 frame.

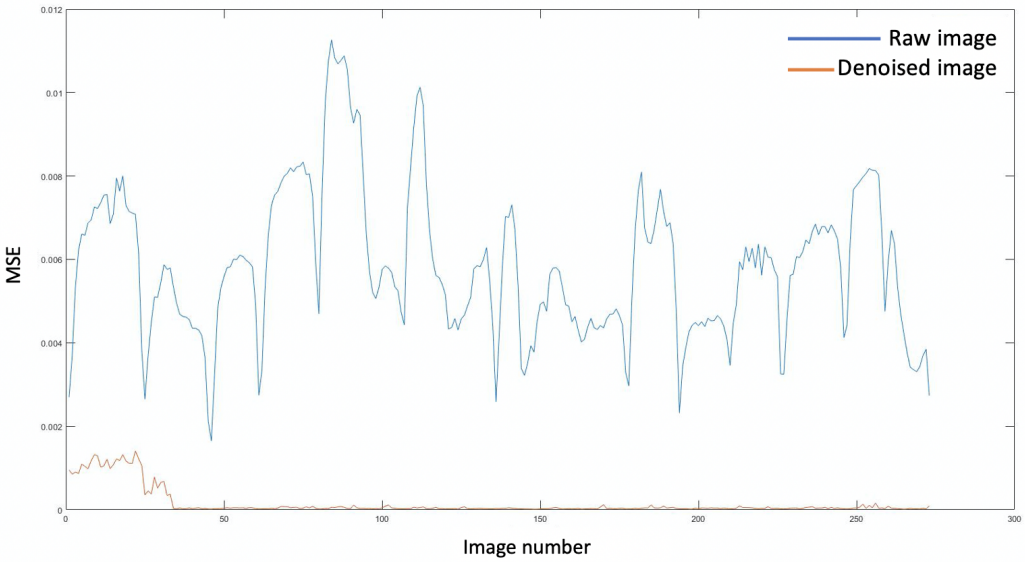

Figure 6-16: Comparison of MSE at the raw image of two objects in blue (before training X_2) and the denoised image in orange (after training Y_{new}) when the network is trained by two objects dataset (X_2 with w_2)

Since the test dataset was the same as training dataset in last experiment, the second experiment is using one object dataset of 439 pairs of images which is the same one as for the one object learning in *Training 1*.

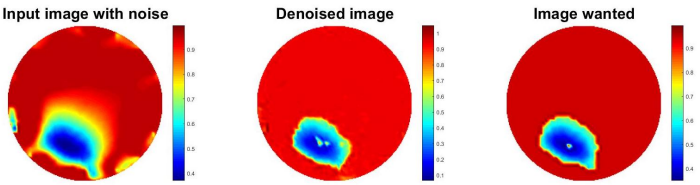

(a)

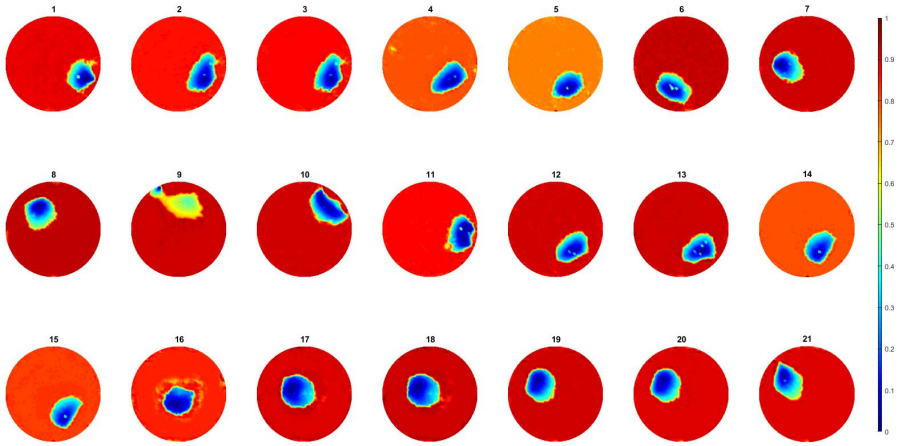

(b)

Figure 6-17: Improvement of two objects test (Y_{new}) for one objects raw images (X_1) passed through two objects trained network (X_2 with w_2)

This is an interesting observation where the neural net was used to train by using two pressure points data and tested against a single point experiment, the results were very good shown in Figure 6-17. Compare to the images in Figure 6-3b, there is a huge improvement in visibility, the amplitude and location of the pressure point is more specific, almost all error caused by electrodes movement are eliminated. The MSE of the output of one object testing is reduced as desired shown in Figure 6-18, the value of the error reducing compare to last training 1 in Figure 6-13 is less. The main reason of this is the MSE of the raw data of the one object images is already small, therefore, the amplitude of reduction in this test is relative small.

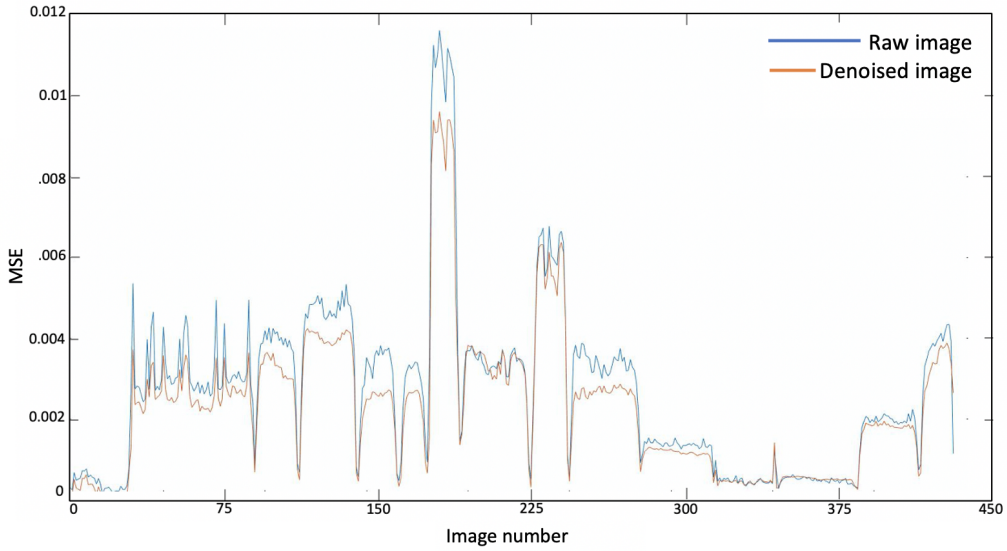

Figure 6-18: Comparison of MSE at the raw image of one object in blue (before training X_1) and the denoised image in orange (after training Y_{new}) when the network is trained by two objects dataset (X_2 with w_2)

A conductive fabric behaviour is complex in both resistive and reactive terms under and applied AC current, because of the capacitances produced by the interactions of the conductive yarns and air gaps. A stretchable conductive fabric shows an even more complex behaviour. Due to complex nature of this sensing the deep learning approach shown in this chapter actually does more than an image post processing, it overcome some of these model uncertainties that are extremely hard to physical model. More than that, some of the medical EIT application is suffering from the noise caused by electrode movement as well, such as moving chest during breathing. The result in deep learning denoise demonstrate that it can also apply to medical EIT to solve the similar problem.

6.5 Conclusion

An ideal material used in EIT system for artificial skin would be light-weight, have continuous and homogeneous conductivity, low-cost, local conductivity changes in response to touch or pressure and will not be affected by stretching. The fabric used in this study is conductive, the conductivity changes as it is stretched,

and it is light-weight and low-cost as wanted. This simplicity of sensor comes with some complex electromechanical behaviour which is not easy to model in forward model. In previous study, pressure or touch could be detected by fabric EIT system statically. The dynamic behaviour of the fabric EIT system were presented in this chapter, where the ST-TV reconstruction algorithm was used. The experimental shows the temporal performance in data collecting and generated a movie like pressure mapping at the same time. The hysteresis behaviour was shown during experiment, motivating future studies in time-related response of the fabric EIT system. There are still some major errors caused by electrode movement and other inevitable shape-shift of the fabric in reconstruction images. To overcome these problems, the deep learning is justified in this chapter. In training stage, the results of test data set are going through trained net-work (using independent data set) are impressive in error reduction for all cases shown here. The way to improve image visibility and reduce these errors through neural network is effective and has the advantage of being autonomous. And the training result shows the potential in applying to other medical applications such as lung imaging.

Chapter 7

Conclusion and Future work

7.1 Conclusion

The main purpose of this thesis is to expand the applications of EIT as widely as possible to express its value as a non-invasive, high temporal resolution and low-cost imaging technique. Each chapter raises a specific problem/application and presents the investigation procedure that has been conducted, the methodologies been applied, the experimental or simulation results obtained, the in-depth discussions and the valuable novel findings or conclusions.

The most important subject in the literature review chapters is the STTV algorithm which applied to dynamical fabric EIT in chapter 6 for the first time and enabled a movie like pressure mapping result. The historical background, hardware systems' development and the applications of EIT are reviewed in Chapter 2. Also, current development of multi-modalities which involves EIT is summarised and reviewed in this chapter. The applications of EIT/ECT are mainly contributed in process tomography for flow measuring and visualizing; the combination of EIT/CT is working in medical applications for improving image quality; and the applications of EIT with ultrasound are broadly applied in industry. The basic mathematical theory including Maxwell's equations, forward modelling, FEM, Jacobian and reconstruction algorithms are reviewed as well, simple mathematical derivations are conducted in Chapter 3.

Chapter 4 presents a complex EIT system of determining conductivity and permittivity distribution simultaneously, where the resistive and capacitive impedance are indicated from the real and imaginary part of voltage measurements. A complex-valued forward model, novel Jacobian matrix derivation and inverse solution are developed in the adjacent current excitation mode. The effects of changing conductivity, permittivity and excitation frequency to reconstructed images are presented in simulation studies, also a real case application simulation in three-phase material imaging implemented . However, the result shows that it is still difficult for complex EIT to generate both pure conductivity and permittivity distributions so far, the interaction of the conductivity and the permittivity of the ROI is complex which means this complex EIT for non-bio applications is critical at this point. Hence, the real case three-phase simulation fails to produce the three phase image that depends on different permittivity, leading to a need of new solution in such application.

Chapter 5 introduced a novel three-phase flow imaging and characterisation using a combined transmission mode ultrasound tomography using speed of sound and EIT for industrial application. EIT is used to identify non-conductive phase which either oil or gas phase and hence UTT is used to identify air phase. A image fusion method has developed to generate the three-phase image. This dual modality enables three-phase material imaging by providing complimentary information from each imaging system. The results demonstrate successful characterisation of these three-phase of oil, water and gas in water dominate cases and the three-phase images are produced using proposed fusion method.

Chapter 6 presents an EIT pressure mapping sensing using piezo-resistive fabric to represent aspects of the sense of touch. For the first time a dynamical touch sensing are studies by means of a spatio-temporal based EIT imaging on a conductive fabric. The conductivity of the fabric changes as it is stretched, and the fabric is light-weight and low-cast which can be a good alternative option for robotic skin. The experimental shows good results of temporal performance in data collecting and generated a movie like pressure mapping at the same time. This simplicity of sensor comes with some complex electromechanical behaviour which is not easy to model in forward model. Hence the use of the deep learning is implemented in this application for improving image quality. The results of

test data set are going through trained net-work (using independent data set) are impressive in error reduction for all cases. The way to improve image visibility and reduce these errors through neural network is effective and has the advantage of being autonomous, also has the potential of applying in similar applications.

7.2 Future work

In this thesis, there are three main applications proposed. Based on those findings as well as the limitations in each application, many potential future researches could be launched:

Complex EIT

As it has been mentioned in Chapter 4's conclusion, it is still difficult for complex EIT to generate both pure conductivity and permittivity distributions so far, which means this complex EIT is critical and needs further investigation.

EIT/UTT dual-modality

The current experimental study is based on static situation, to fully explore the potential of this EIT/UTT dual-modality, more practical experimental environment should be created. For example, to simulate a three-phase flow, the air-phase samples can be replaced by constantly injecting air bubbles and the oil-phase can be moved slowly during the experiment. Thus, a dynamical flow data can be collected and using proposed STTV algorithm to produce a movie like result. The fusion images produced by this dual-modality are limited when two samples are too close to each other, the cause of this problem is the limitation of the low resolution of the EIT. Therefore, further improvement of the image quality of the EIT should be launched. Also, the application of EIT/UTT dual-modality should not be limited in only applying for process tomography, other engineering field can be considered.

Fabric EIT with deep learning

At the current stage of the fabric EIT sensor, only the simplest mathematical model is considered and is assumed to be a linear problem between change in voltage measurement and conductivity. However, the structure of fabric material is complex, and thinking of reconstructing images due to pressure, it is required to calculate and linearise the problem more precisely and in more detail. If a more accurate model can be created in the future, the reconstructed image is expected to be of much better quality. Also, the hysteresis behaviour of the fabric EIT was shown during experiment, motivating future studies in time-related response of the system. At the deep learning stage, more data set can be collected and to test. And so far the training was based on individual frames, if the network could be improve to a spatio-temporal correlated, the training time could be reduced and a possible better denoise result.

Appendix A

Publications

X. Duan, S. Taurand, and M. Soleimani, "Artificial skin through super-sensing method and electrical impedance data from conductive fabric withaid of deep learning," *Scientific Reports*, vol. 9, no. 1, p. 8831, 2019

X. Duan P, Koulountzios and M. Soleimani, "Dual modality EIT-UTT for water dominate three-phase material imaging" *IEEE Access* vol. 8, no.1, pp. 14 523–14 530, 2020

Appendix B

Code for complex Jacobian

Perturbation based complex Jacobian is shown here:

```
Delta_c= 1e-7;
for i=1:1024
i
imgt=img;
imgt.elem_data([i])=sigma*(1+Delta_c)+sqrt(-1)*2*pi*f*epsi;
vi=fwd_solve(imgt);

Jrr=[Jrr,real(vi.meas-vh.meas)/(Delta_c)];
Jir=[Jir,imag(vi.meas-vh.meas)/(Delta_c)];

imgt.elem_data([i])=sigma+sqrt(-1)*2*pi*f*epsi;

imgtt=img;
imgtt.elem_data([i])=sigma+sqrt(-1)*(2*pi*f*(epsi+Delta_c));
vii=fwd_solve(imgtt);

Jri=[Jri,real(vii.meas-vh.meas)/(1*Delta_c*2*pi*f)];
Jii=[Jii,imag(vii.meas-vh.meas)/(1*Delta_c*2*pi*f)];

imgt.elem_data([i])=sigma+sqrt(-1)*2*pi*f*epsi;
end

J=[Jrr, Jri;Jir, Jii];
```

References

[1] H.-Y. Wei and M. Soleimani, "Electromagnetic tomography for medical and industrial applications: Challenges and opportunities [point of view]," *Proceedings of the IEEE*, vol. 101, no. 3, pp. 559–565, 2013.

[2] W. Petersson, "Om malmskande medelst elektricitet," vol. 2, no. 3, pp. 153–171, 1907.

[3] T. Dahlin, "The development of dc resistivity imaging techniques," *Computers & Geosciences*, vol. 27, no. 9, pp. 1019–1029, 2001.

[4] R. Avill, Y. Mangnall, N. Bird, B. Brown, A. Seagar, A. Johnson, N. Read, *et al.*, "Applied potential tomography: A new noninvasive technique for measuring gastric emptying," *Gastroenterology*, vol. 92, no. 4, pp. 1019–1026, 1987.

[5] D. C. Barber and B. H. Brown, "Applied potential tomography," *Journal of Physics E: Scientific Instruments*, vol. 17, no. 9, p. 723, 1984.

[6] E. Malone, M. Jehl, S. Arridge, T. Betcke, and D. Holder, "Stroke type differentiation using spectrally constrained multifrequency eit: Evaluation of feasibility in a realistic head model," *Physiological measurement*, vol. 35, no. 6, p. 1051, 2014.

[7] R. J. Halter, A. Hartov, S. P. Poplack, W. A. Wells, K. M. Rosenkranz, R. J. Barth, P. A. Kaufman, K. D. Paulsen, *et al.*, "Real-time electrical impedance variations in women with and without breast cancer," *IEEE transactions on medical imaging*, vol. 34, no. 1, pp. 38–48, 2014.

[8] M. S. Campisi, C. Barbre, A. Chola, G. Cunningham, V. Woods, and J. Viventi, "Breast cancer detection using high-density flexible electrode arrays and electrical impedance tomography," in *2014 36th Annual In-*

ternational Conference of the IEEE Engineering in Medicine and Biology Society, IEEE, 2014, pp. 1131–1134.

[9] M. Wang, "Impedance mapping of particulate multiphase flows," *Flow Measurement and Instrumentation*, vol. 16, no. 2-3, pp. 183–189, 2005.

[10] Q. Wang, J. Polansky, M. Wang, K. Wei, C. Qiu, A. Kenbar, and D. Millington, "Capability of dual-modality electrical tomography for gas-oil-water three-phase pipeline flow visualisation," *Flow Measurement and Instrumentation*, vol. 62, pp. 152–166, 2018.

[11] M. Wang, J. Jia, Y. Faraj, Q. Wang, C.-g. Xie, G. Oddie, K. Primrose, and C. Qiu, "A new visualisation and measurement technology for water continuous multiphase flows," *Flow Measurement and Instrumentation*, vol. 46, pp. 204–212, 2015.

[12] Y. Kato, T. Mukai, T. Hayakawa, and T. Shibata, "Tactile sensor without wire and sensing element in the tactile region based on eit method," in *Sensors, 2007 IEEE*, IEEE, 2007, pp. 792–795.

[13] A. Yao and M. Soleimani, "A pressure mapping imaging device based on electrical impedance tomography of conductive fabrics," *Sensor Review*, vol. 32, no. 4, pp. 310–317, 2012.

[14] A. Yao, C. L. Yang, J. K. Seo, and M. Soleimani, "Eit-based fabric pressure sensing," *Computational and mathematical methods in medicine*, vol. 2013, 2013.

[15] H. Jain, D. Isaacson, P. M. Edic, and J. C. Newell, "Electrical impedance tomography of complex conductivity distributions with noncircular boundary," *IEEE transactions on biomedical engineering*, vol. 44, no. 11, pp. 1051–1060, 1997.

[16] C. N. Herrera, M. F. Vallejo, J. L. Mueller, and R. G. Lima, "Direct 2-d reconstructions of conductivity and permittivity from eit data on a human chest," *IEEE transactions on medical imaging*, vol. 34, no. 1, pp. 267–274, 2014.

[17] L. F. Fuks, M. Cheney, D. Isaacson, D. G. Gisser, and J. Newell, "Detection and imaging of electric conductivity and permittivity at low frequency," *IEEE Transactions on Biomedical Engineering*, vol. 38, no. 11, pp. 1106–1110, 1991.

[18] Z. Zhu and Y. Wang, "Simultaneous reconstruction of conductivity and permittivity in electrical impedance tomography," in *2019 Chinese Control And Decision Conference (CCDC)*, IEEE, 2019, pp. 3211–3215.

[19] C. Yang, A. Mohammed, Y. Mohamadou, T. Oh, and M. Soleimani, "Complex conductivity reconstruction in multiple frequency electrical impedance tomography for fabric-based pressure sensor," *Sensor Review*, 2015.

[20] R. Thorn, G. A. Johansen, and B. T. Hjertaker, "Three-phase flow measurement in the petroleum industry," *Measurement Science and Technology*, vol. 24, no. 1, p. 012 003, 2012.

[21] S. Corneliussen, J.-p. Couput, E. Dahl, E. Dykesteen, K.-E. Frøysa, E. Malde, H. Moestue, P. O. Moksnes, L. Scheers, and H. Tunheim, "Handbook of multiphase flow metering," 2005.

[22] K. E. Kee, "A study of flow patterns and surface wetting in gas-oil-water flow," PhD thesis, Ohio University, 2014.

[23] G. Hewitt, "Three-phase gas–liquid–liquid flows in the steady and transient states," *Nuclear engineering and design*, vol. 235, no. 10-12, pp. 1303–1316, 2005.

[24] M. Açikgöz, F. Franca, and R. Lahey Jr, "An experimental study of three-phase flow regimes," *International Journal of Multiphase Flow*, vol. 18, no. 3, pp. 327–336, 1992.

[25] A. Serapião and A. C. Bannwart, "Knowledge discovery for classification of three-phase vertical flow patterns of heavy oil from pressure drop and flow rate data," *Journal of Petroleum Engineering*, vol. 2013, 2013.

[26] E. C. Donaldson, G. V. Chilingarian, and T. F. Yen, *Enhanced oil recovery, II: Processes and operations*. Elsevier, 1989.

[27] K. K. Patel, M. Mehta, and T. R. Singh, "Application of homotopy analysis method in one-dimensional instability phenomenon arising in inclined porous media," *American Journal of Applied Mathematics and Statistics*, vol. 2, no. 3, pp. 106–114, 2014.

[28] C. Qiu, B. Hoyle, and F. Podd, "Engineering and application of a dual-modality process tomography system," *Flow Measurement and Instrumentation*, vol. 18, no. 5-6, pp. 247–254, 2007.

[29] S. Yue, T. Wu, J. Pan, and H. Wang, "Fuzzy clustering based et image fusion," *Information Fusion*, vol. 14, no. 4, pp. 487–497, 2013.

[30] J. Sun and W. Yang, "A dual-modality electrical tomography sensor for measurement of gas–oil–water stratified flows," *Measurement*, vol. 66, pp. 150–160, 2015.

[31] M. Zhang, L. Ma, and M. Soleimani, "Dual modality ect–mit multi-phase flow imaging," *Flow Measurement and Instrumentation*, vol. 46, pp. 240–254, 2015.

[32] B. Hjertaker, R. Maad, and G. Johansen, "Dual-mode capacitance and gamma-ray tomography using the landweber reconstruction algorithm," *Measurement Science and Technology*, vol. 22, no. 10, p. 104 002, 2011.

[33] M. Soleimani, "Electrical impedance tomography imaging using a priori ultrasound data," *Biomedical engineering online*, vol. 5, no. 1, p. 8, 2006.

[34] F. M. Yunus, R. A. Rahim, S. Aw, N. N. Ayob, C. L. Goh, and M. Pusppanathan, "Simulation study of electrode size in air-bubble detection for dual-mode integrated electrical resistance and ultrasonic transmission tomography," *Powder Technology*, vol. 256, pp. 224–232, 2014.

[35] C. Tan, Y. Yuan, X. Dong, and F. Dong, "Oil–water two-phase flow measurement with combined ultrasonic transducer and electrical sensors," *Measurement Science and Technology*, vol. 27, no. 12, p. 125 307, 2016.

[36] D. Silvera-Tawil, D. Rye, M. Soleimani, and M. Velonaki, "Electrical impedance tomography for artificial sensitive robotic skin: A review," *IEEE Sensors Journal*, vol. 15, no. 4, pp. 2001–2016, 2015.

[37] K. Weiß and H. Worn, "The working principle of resistive tactile sensor cells," in *Mechatronics and Automation, 2005 IEEE International Conference*, IEEE, vol. 1, 2005, pp. 471–476.

[38] T. V. Papakostas, J. Lima, and M. Lowe, "A large area force sensor for smart skin applications," in *Sensors, 2002. Proceedings of IEEE*, IEEE, vol. 2, 2002, pp. 1620–1624.

[39] R. S. Dahiya, G. Metta, M. Valle, and G. Sandini, "Tactile sensing—from humans to humanoids," *IEEE transactions on robotics*, vol. 26, no. 1, pp. 1–20, 2010.

[40] B. Choi, S. Lee, H. R. Choi, and S. Kang, "Development of anthropomorphic robot hand with tactile sensor: Skku hand ii," in *Intelligent Robots and Systems, 2006 IEEE/RSJ International Conference on*, IEEE, 2006, pp. 3779–3784.

[41] A. Schmitz, P. Maiolino, M. Maggiali, L. Natale, G. Cannata, and G. Metta, "Methods and technologies for the implementation of large-scale robot tactile sensors," *IEEE Transactions on Robotics*, vol. 27, no. 3, pp. 389–400, 2011.

[42] Y. Ohmura, Y. Kuniyoshi, and A. Nagakubo, "Conformable and scalable tactile sensor skin for curved surfaces," in *Robotics and Automation, 2006. ICRA 2006. Proceedings 2006 IEEE International Conference on*, IEEE, 2006, pp. 1348–1353.

[43] E. M. Reimer and L. Danisch, *Pressure sensor based on illumination of a deformable integrating cavity*, US Patent 5,917,180, Jun. 1999.

[44] P. S. Girão, P. M. P. Ramos, O. Postolache, and J. M. D. Pereira, "Tactile sensors for robotic applications," *Measurement*, vol. 46, no. 3, pp. 1257–1271, 2013.

[45] Alirezaei, Hassan and Nagakubo, Akihiko and Kuniyoshi, Yasuo, "A tactile distribution sensor which enables stable measurement under high and dynamic stretch," in *2009 IEEE Symposium on 3D User Interfaces*, IEEE, 2009, 87–93.

[46] Nagakubo, Akihiko and Alirezaei, Hassan and Kuniyoshi, Yasuo, "A deformable and deformation sensitive tactile distribution sensor," in *2007 IEEE International Conference on Robotics and Biomimetics (ROBIO)*, IEEE, 2007, 1301–1308.

[47] D. Barber and B. Brown, "Recent developments in applied potential tomography-apt," in *Information processing in medical imaging*, Springer, 1986, pp. 106–121.

[48] X. Duan, P. Koulountzios, and M. Soleimani, "Dual modality eit-utt for water dominate three-phase material imaging," *IEEE Access*, vol. 8, no. 1, pp. 14 523–14 530, 2020.

[49] X. Duan, S. Taurand, and M. Soleimani, "Artificial skin through super-sensing method and electrical impedance data from conductive fabric with aid of deep learning," *Scientific Reports*, vol. 9, no. 1, p. 8831, 2019.

[50] B. H. Brown, "Electrical impedance tomography (eit): A review," *Journal of medical engineering & technology*, vol. 27, no. 3, pp. 97–108, 2003.

[51] R. P. Henderson and J. G. Webster, "An impedance camera for spatially specific measurements of the thorax," *IEEE Transactions on Biomedical Engineering*, no. 3, pp. 250–254, 1978.

[52] B. H. Brown and A. D. Seagar, "The sheffield data collection system," *Clinical Physics and Physiological Measurement*, vol. 8, no. 4A, p. 91, 1987.

[53] B. Brown, D. Barber, W. Wang, L. Lu, A. Leathard, R. Smallwood, A. Hampshire, R. Mackay, and K. Hatzigalanis, "Multi-frequency imaging and modelling of respiratory related electrical impedance changes," *Physiological measurement*, vol. 15, no. 2A, A1, 1994.

[54] R. Bayford, Y. Hanquan, K. Boone, and D. Holder, "Experimental validation of a novel reconstruction algorithm for electrical impedance tomography based on backprojection of lagrange multipliers," *Physiological measurement*, vol. 16, no. 3A, A237, 1995.

[55] M. Cheney, D. Isaacson, J. C. Newell, S. Simske, and J. Goble, "Noser: An algorithm for solving the inverse conductivity problem," *International Journal of Imaging systems and technology*, vol. 2, no. 2, pp. 66–75, 1990.

[56] E. J. Woo and J. G. Webster, "Finite element method and reconstruction algorithms in electrical impedance tomography," *Annals of Biomedical Engineering*, vol. 19, no. 2, pp. 228–229, 1991.

[57] A. Hampshire, R. Smallwood, B. Brown, and R. Primhak, "Multifrequency and parametric eit images of neonatal lungs," *Physiological measurement*, vol. 16, no. 3A, A175, 1995.

[58] R. J. Yerworth, R. Bayford, B. Brown, P. Milnes, M. Conway, and D. S. Holder, "Electrical impedance tomography spectroscopy (eits) for human head imaging," *Physiological measurement*, vol. 24, no. 2, p. 477, 2003.

[59] A. Baxter, Y. Mangnall, E. Loj, B. Brown, D. Barber, A. Johnson, and N. Read, "Evaluation of applied potential tomography as a new non-invasive gastric secretion test.," *Gut*, vol. 29, no. 12, pp. 1730–1735, 1988.

[60] S. Nour, Y. Mangnall, J. Dickson, R. Pearse, and A. Johnson, "Measurement of gastric emptying in infants with pyloric stenosis using applied potential tomography.," *Archives of disease in childhood*, vol. 68, no. 4, pp. 484–486, 1993.

[61] R. Erol, R. Smallwood, B. Brown, P. Cherian, and K. Bardhan, "Detecting oesophageal-related changes using electrical impedance tomography," *Physiological measurement*, vol. 16, no. 3A, A143, 1995.

[62] J. Newell, D. G. Gisser, and D. Isaacson, "An electric current tomograph," *IEEE Transactions on Biomedical Engineering*, vol. 35, no. 10, pp. 828–833, 1988.

[63] J. Campbell, N. Harris, F. Zhang, B. Brown, and A. Morice, "Clinical applications of electrical impedance tomography in the monitoring of changes in intrathoracic fluid volumes," *Physiological measurement*, vol. 15, no. 2A, A217, 1994.

[64] B. Eyuboglu, B. Brown, D. Barber, and A. Seager, "Localisation of cardiac related impedance changes in the thorax," *Clinical Physics and Physiological Measurement*, vol. 8, no. 4A, p. 167, 1987.

[65] F. McArdle, B. Brown, and A. Angel, "Imaging cardiosynchronous impedance changes in the adult head," *Clinical and physiological applications of electrical impedance tomography*, vol. 20, pp. 177–184, 1993.

[66] A. Dijkstra, B. Brown, A. Leathard, N. Harris, D. Barber, and D. Edbrooke, "Review clinical applications of electrical impedance tomography," *Journal of medical engineering & technology*, vol. 17, no. 3, pp. 89–98, 1993.

[67] G. A. Ybarra, Q. H. Liu, G. Ye, K. H. Lim, J.-H. Lee, W. T. Joines, and R. T. George, "Breast imaging using electrical impedance tomography (eit)," *Emerging Technology in Breast Imaging and Mammography, American Scientific Publishers*, pp. 1–16, 2007.

[68] J. Jossinet, "Variability of impedivity in normal and pathological breast tissue," *Medical and biological engineering and computing*, vol. 34, no. 5, pp. 346–350, 1996.

[69] K. Boone, D. Barber, and B. Brown, "Imaging with electricity: Report of the european concerted action on impedance tomography," *Journal of medical engineering & technology*, vol. 21, no. 6, pp. 201–232, 1997.

[70] R. H. Bayford, "Bioimpedance tomography (electrical impedance tomography)," *Annu. Rev. Biomed. Eng.*, vol. 8, pp. 63–91, 2006.

[71] A. McEwan, G. Cusick, and D. Holder, "A review of errors in multi-frequency eit instrumentation," *Physiological measurement*, vol. 28, no. 7, S197, 2007.

[72] A. Wilson, P. Milnes, A. Waterworth, R. Smallwood, and B. Brown, "Mk3. 5: A modular, multi-frequency successor to the mk3a eis/eit system," *Physiological Measurement*, vol. 22, no. 1, p. 49, 2001.

[73] D. Holder, C. GONZÁLEZ-CORREA, T. Tidswell, A. Gibson, G. Cusick, and R. Bayford, "Assessment and calibration of a low-frequency system for electrical impedance tomography (eit), optimized for use in imaging brain function in ambulant human subjects," *Annals of the New York Academy of Sciences*, vol. 873, no. 1, pp. 512–519, 1999.

[74] R. J. Yerworth, R. Bayford, G. Cusick, M. Conway, and D. S. Holder, "Design and performance of the uclh mark 1b 64 channel electrical impedance tomography (eit) system, optimized for imaging brain function," *Physiological measurement*, vol. 23, no. 1, p. 149, 2002.

[75] A. McEwan, A. Romsauerova, R. Yerworth, L. Horesh, R. Bayford, and D. Holder, "Design and calibration of a compact multi-frequency eit system for acute stroke imaging," *Physiological measurement*, vol. 27, no. 5, S199, 2006.

[76] T. I. Oh, E. J. Woo, and D. Holder, "Multi-frequency eit system with radially symmetric architecture: Khu mark1," *Physiological measurement*, vol. 28, no. 7, S183, 2007.

[77] T. I. Oh, H. Wi, D. Y. Kim, P. J. Yoo, and E. J. Woo, "A fully parallel multi-frequency eit system with flexible electrode configuration: Khu mark2," *Physiological measurement*, vol. 32, no. 7, p. 835, 2011.

[78] W. Wang, B. Brown, and D. Barber, "Performance of the sheffield mk3a multi-frequency system for electrical impedance tomography," in *IEE Colloquium on Innovations in Instrumentation for Electrical Tomography*, IET, 1995, pp. 10–1.

[79] F. Lidgey, Q. Zhu, C. McLeod, and W. Breckon, "Electrode current determination from programmable voltage sources," *Clinical Physics and Physiological Measurement*, vol. 13, no. A, p. 43, 1992.

[80] Q. Zhu, C. McLeod, C. Denyer, F. Lidgey, and W. Lionheart, "Development of a real-time adaptive current tomograph," *Physiological measurement*, vol. 15, no. 2A, A37, 1994.

[81] X. Yue and C. McLeod, "Fpga design and implementation for eit data acquisition," *Physiological measurement*, vol. 29, no. 10, p. 1233, 2008.

[82] R. Halter, A. Hartov, and K. D. Paulsen, "Design and implementation of a high frequency electrical impedance tomography system," *Physiological measurement*, vol. 25, no. 1, p. 379, 2004.

[83] R. J. Halter, A. Hartov, and K. D. Paulsen, "A broadband high-frequency electrical impedance tomography system for breast imaging," *IEEE Transactions on biomedical engineering*, vol. 55, no. 2, pp. 650–659, 2008.

[84] R. D. Cook, G. J. Saulnier, D. G. Gisser, J. C. Goble, J. Newell, and D. Isaacson, "Act3: A high-speed, high-precision electrical impedance tomograph," *IEEE Transactions on Biomedical Engineering*, vol. 41, no. 8, pp. 713–722, 1994.

[85] N. Liu, "Act4: A high-precision, multi-frequency electrical impedance tomograph," PhD thesis, Rensselaer Polytechnic Institute, 2007.

[86] D. Holder, *Clinical and physiological applications of electrical impedance tomography*. CRC Press, 1993.

[87] A. Borsic, R. Halter, Y. Wan, A. Hartov, and K. Paulsen, "Electrical impedance tomography reconstruction for three-dimensional imaging of the prostate," *Physiological measurement*, vol. 31, no. 8, S1, 2010.

[88] T. E. Kerner, K. D. Paulsen, A. Hartov, S. K. Soho, and S. P. Poplack, "Electrical impedance spectroscopy of the breast: Clinical imaging results in 26 subjects," *IEEE transactions on medical imaging*, vol. 21, no. 6, pp. 638–645, 2002.

[89] R. Li, J. Gao, Y. Li, J. Wu, Z. Zhao, and Y. Liu, "Preliminary study of assessing bladder urinary volume using electrical impedance tomography," *Journal of Medical and Biological Engineering*, vol. 36, no. 1, pp. 71–79, 2016.

[90] K. Y. Aristovich, B. C. Packham, H. Koo, G. S. dos Santos, A. McEvoy, and D. S. Holder, "Imaging fast electrical activity in the brain with electrical impedance tomography," *NeuroImage*, vol. 124, pp. 204–213, 2016.

[91] M. Wang, W. Yin, and N. Holliday, "A highly adaptive electrical impedance sensing system for flow measurement," *Measurement Science and Technology*, vol. 13, no. 12, p. 1884, 2002.

[92] H. Tapp, A. Peyton, E. Kemsley, and R. Wilson, "Chemical engineering applications of electrical process tomography," *Sensors and Actuators B: Chemical*, vol. 92, no. 1-2, pp. 17–24, 2003.

[93] A. Cataldo, R. Persico, G. Leucci, E. De Benedetto, G. Cannazza, L. Matera, and L. De Giorgi, "Time domain reflectometry, ground penetrating radar and electrical resistivity tomography: A comparative analysis of alternative approaches for leak detection in underground pipes," *Ndt & E International*, vol. 62, pp. 14–28, 2014.

[94] J. Jordana, M. Gasulla, and R. Pallàs-Areny, "Electrical resistance tomography to detect leaks from buried pipes," *Measurement Science and Technology*, vol. 12, no. 8, p. 1061, 2001.

[95] J. Hoła, Z. Matkowski, K. Schabowicz, J. Sikora, K. Nita, and S. Wójtowicz, "Identification of moisture content in brick walls by means of impedance tomography," *COMPEL-The international journal for computation and mathematics in electrical and electronic engineering*, vol. 31, no. 6, pp. 1774–1792, 2012.

[96] T. Rymarczyk, G. Kłosowski, and E. Kozłowski, "A non-destructive system based on electrical tomography and machine learning to analyze the moisture of buildings," *Sensors*, vol. 18, no. 7, p. 2285, 2018.

[97] T.-C. Hou, K. J. Loh, and J. P. Lynch, "Spatial conductivity mapping of carbon nanotube composite thin films by electrical impedance tomography for sensing applications," *Nanotechnology*, vol. 18, no. 31, p. 315 501, 2007.

[98] T. A. York, "Status of electrical tomography in industrial applications," in *Process Imaging for Automatic Control*, International Society for Optics and Photonics, vol. 4188, 2001, pp. 175–190.

[99] Z. Ren and W. Yang, "3d positioning for revision total hip replacement surgery by dual-modality tomography," in *2015 IEEE International Conference on Imaging Systems and Techniques (IST)*, IEEE, 2015, pp. 1–6.

[100] T. Pengpan, C. Mitchell, and M. Soleimani, "A dual modality of cone beam ct and electrical impedance tomography for lung imaging," in *Journal of Physics: Conference Series*, IOP Publishing, vol. 224, 2010, p. 012 026.

[101] T. Pengpen and M. Soleimani, "Motion-compensated cone beam ct using a conjugate gradient least squares algorithm and eit imaging motion data,"

[102] X. Chen, J. Li, and H. Wang, "Eit imaging fused with ct slice," in *2012 IEEE International Conference on Imaging Systems and Techniques Proceedings*, IEEE, 2012, pp. 234–238.

[103] K. Krishnan, J. Liu, and K. Kohli, "Assessment of eit/ct fusion imaging using a biological phantom," 2014.

[104] B. Schullcke, B. Gong, S. Krueger-Ziolek, M. Soleimani, U. Mueller-Lisse, and K. Moeller, "Structural-functional lung imaging using a combined ct-eit and a discrete cosine transformation reconstruction method," *Scientific reports*, vol. 6, p. 25 951, 2016.

[105] G. Steiner, M. Soleimani, H. Dehghani, D. Watzenig, and F. Podd, "Tomographic image reconstruction from dual modality ultrasound and electrical impedance data," in *13th International Conference on Electrical Bioimpedance and the 8th Conference on Electrical Impedance Tomography*, Springer, 2007, pp. 288–291.

[106] G. Steiner, M. Soleimani, and D. Watzenig, "A bio-electromechanical imaging technique with combined electrical impedance and ultrasound tomography," *Physiological measurement*, vol. 29, no. 6, S63, 2008.

[107] S. Teniou and M. Meribout, "A multimodal image reconstruction method using ultrasonic waves and electrical resistance tomography," *IEEE Transactions on Image Processing*, vol. 24, no. 11, pp. 3512–3521, 2015.

[108] K. Ain, D. Kurniadi, S. Suprijanto, and O. Santoso, "Dual modality electrical impedance and ultrasound reflection tomography to improve image quality," *Journal of Electrical Bioimpedance*, vol. 8, no. 1, pp. 3–10, 2017.

[109] G. Liang, S. Ren, and F. Dong, "An augmented lagrangian trust region method for inclusion boundary reconstruction using ultrasound/electrical dual-modality tomography," *Measurement Science and Technology*, vol. 29, no. 7, p. 074 008, 2018.

[110] G. Liang, S. Ren, S. Zhao, and F. Dong, "A lagrange-newton method for eit/ut dual-modality image reconstruction," *Sensors*, vol. 19, no. 9, p. 1966, 2019.

[111] F. R. M. Yunus, N. A. N. Azlan, N. M. N. Ayob, M. J. Pusppanathan, M. F. Jumaah, C. Goh, R. A. Rahim, A. Ahmad, Y. M. Yunus, and H. A. Rahim, "Simulation study of bubble detection using dual-mode electrical resistance and ultrasonic transmission tomography for two-phase liquid and gas," *Sensors & Transducers*, vol. 150, no. 3, p. 97, 2013.

[112] C. Xu, X. Dong, X. Shi, F. Fu, W. Shuai, R. Liu, and F. You, "Comparison of drive patterns for single current source eit in computational phantom," in *2008 2nd International Conference on Bioinformatics and Biomedical Engineering*, IEEE, 2008, pp. 1500–1503.

[113] R. Harikumar, R. Prabu, and S. Raghavan, "Electrical impedance tomography (eit) and its medical applications: A review," *Int. J. Soft Comput. Eng*, vol. 3, no. 4, pp. 193–198, 2013.

[114] N. Avis and D. Barber, "Image reconstruction using non-adjacent drive configurations (electric impedance tomography)," *Physiological measurement*, vol. 15, no. 2A, A153, 1994.

[115] M. Cheney, D. Isaacson, and J. C. Newell, "Electrical impedance tomography," *SIAM review*, vol. 41, no. 1, pp. 85–101, 1999.

[116] P. J. Vauhkonen, M. Vauhkonen, T. Savolainen, and J. P. Kaipio, "Three-dimensional electrical impedance tomography based on the complete electrode model," *IEEE Transactions on Biomedical Engineering*, vol. 46, no. 9, pp. 1150–1160, 1999.

[117] E. Somersalo, M. Cheney, and D. Isaacson, "Existence and uniqueness for electrode models for electric current computed tomography," *SIAM Journal on Applied Mathematics*, vol. 52, no. 4, pp. 1023–1040, 1992.

[118] W. Lionheart, N. Polydorides, and A. Borsic, "The reconstruction problem," *Electrical impedance tomography: methods, history and applications*, vol. 750309520, pp. 3–64, 2005.

[119] M. Vauhkonen, W. R. Lionheart, L. M. Heikkinen, P. J. Vauhkonen, and J. P. Kaipio, "A matlab package for the eidors project to reconstruct two-dimensional eit images," *Physiological measurement*, vol. 22, no. 1, p. 107, 2001.

[120] B. Brandstatter, "Jacobian calculation for electrical impedance tomography based on the reciprocity principle," *IEEE transactions on magnetics*, vol. 39, no. 3, pp. 1309–1312, 2003.

[121] N. Polydorides and W. R. Lionheart, "A matlab toolkit for three-dimensional electrical impedance tomography: A contribution to the electrical impedance and diffuse optical reconstruction software project," *Measurement science and technology*, vol. 13, no. 12, p. 1871, 2002.

[122] D. Holder, *Electrical impedance tomography: methods, history and applications*. CRC Press, 2004.

[123] F. Santosa and M. Vogelius, "A backprojection algorithm for electrical impedance imaging," *SIAM Journal on Applied Mathematics*, vol. 50, no. 1, pp. 216–243, 1990.

[124] B. Sun, S. Yue, Z. Cui, and H. Wang, "A new linear back projection algorithm to electrical tomography based on measuring data decomposition," *Measurement Science and Technology*, vol. 26, no. 12, p. 125 402, 2015.

[125] M. Vauhkonen, D. Vadasz, P. A. Karjalainen, E. Somersalo, and J. P. Kaipio, "Tikhonov regularization and prior information in electrical impedance tomography," *IEEE transactions on medical imaging*, vol. 17, no. 2, pp. 285–293, 1998.

[126] W. Yang and L. Peng, "Image reconstruction algorithms for electrical capacitance tomography," *Measurement science and technology*, vol. 14, no. 1, R1, 2002.

[127] L. I. Rudin, S. Osher, and E. Fatemi, "Nonlinear total variation based noise removal algorithms," *Physica D: nonlinear phenomena*, vol. 60, no. 1-4, pp. 259–268, 1992.

[128] C. R. Vogel, *Computational methods for inverse problems*. Siam, 2002, vol. 23.

[129] Z. Zhou, G. S. dos Santos, T. Dowrick, J. Avery, Z. Sun, H. Xu, and D. S. Holder, "Comparison of total variation algorithms for electrical impedance tomography," *Physiological measurement*, vol. 36, no. 6, p. 1193, 2015.

[130] T. Goldstein and S. Osher, "The split bregman method for l1-regularized problems," *SIAM journal on imaging sciences*, vol. 2, no. 2, pp. 323–343, 2009.

[131] B. Chen, J. Abascal, and M. Soleimani, "Electrical resistance tomography for visualization of moving objects using a spatiotemporal total variation regularization algorithm," *Sensors*, vol. 18, no. 6, p. 1704, 2018.

[132] B. Chen, J. F. Abascal, and M. Soleimani, "Extended joint sparsity reconstruction for spatial and temporal ert imaging," *Sensors*, vol. 18, no. 11, p. 4014, 2018.

[133] P. Montesinos, J. F. P. Abascal, L. Cussó, J. J. Vaquero, and M. Desco, "Application of the compressed sensing technique to self-gated cardiac cine sequences in small animals," *Magnetic resonance in medicine*, vol. 72, no. 2, pp. 369–380, 2014.

[134] L. He, T.-C. Chang, S. Osher, T. Fang, and P. Speier, "Mr image reconstruction from undersampled data by using the iterative refinement procedure," in *PAMM: Proceedings in Applied Mathematics and Mechanics*, Wiley Online Library, vol. 7, 2007, pp. 1 011 207–1 011 208.

[135] Y. Wang, J. Yang, W. Yin, and Y. Zhang, "A new alternating minimization algorithm for total variation image reconstruction," *SIAM Journal on Imaging Sciences*, vol. 1, no. 3, pp. 248–272, 2008.

[136] A. Adler, J. H. Arnold, R. Bayford, A. Borsic, B. Brown, P. Dixon, T. J. Faes, I. Frerichs, H. Gagnon, Y. Gärber, *et al.*, "Greit: A unified approach to 2d linear eit reconstruction of lung images," *Physiological measurement*, vol. 30, no. 6, S35, 2009.

[137] S. Guillemet-Fritsch, T. Lebey, M. Boulos, and B. Durand, "Dielectric properties of cacu3ti4o12 based multiphased ceramics," *Journal of the European Ceramic Society*, vol. 26, no. 7, pp. 1245–1257, 2006.

[138] P. Koulountzios, T. Rymarczyk, and M. Soleimani, "A quantitative ultrasonic travel-time tomography to investigate liquid elaborations in industrial processes," *Sensors*, vol. 19, no. 23, p. 5117, 2019.

[139] R. A. Rahim, M. F. Rahiman, K. Chan, and S. Nawawi, "Non-invasive imaging of liquid/gas flow using ultrasonic transmission-mode tomography," *Sensors and Actuators A: Physical*, vol. 135, no. 2, pp. 337–345, 2007.

[140] P. Koulountzios, T. Rymarczyk, and M. Soleimani, "Ultrasonic tomography for automated material inspection in liquid masses," in *9th World Congress in industrial process tomography, WCIPT9, Sep 2018*, 2018.

[141] F. Li, J. F. Abascal, M. Desco, and M. Soleimani, "Total variation regularization with split bregman-based method in magnetic induction tomography using experimental data," *IEEE Sensors Journal*, vol. 17, no. 4, pp. 976–985, 2016.

[142] N. Otsu, "A threshold selection method from gray-level histograms," *IEEE transactions on systems, man, and cybernetics*, vol. 9, no. 1, pp. 62–66, 1979.

[143] *Sentec eit pioneer set*, `http://www.swisstom.com/en/products/pioneer-set`, Accessed: 01/05/2019.

[144] L. Heikkinen, J. Kourunen, T. Savolainen, P. Vauhkonen, J. Kaipio, and M. Vauhkonen, "Real time three-dimensional electrical impedance tomography applied in multiphase flow imaging," *Measurement Science and Technology*, vol. 17, no. 8, p. 2083, 2006.

[145] R. W. Smith, I. L. Freeston, and B. H. Brown, "A real-time electrical impedance tomography system for clinical use-design and preliminary results," *IEEE Transactions on Biomedical Engineering*, vol. 42, no. 2, pp. 133–140, 1995.

[146] K. Kim, S. Kang, M. Kim, S. Kim, Y. Lee, and M. Vauhkonen, "Dynamic electrical impedance tomography with known internal structures," *Inverse Problems in Engineering*, vol. 11, no. 1, pp. 1–19, 2003.

[147] P. C. Hansen, "Analysis of discrete ill-posed problems by means of the l-curve," *SIAM review*, vol. 34, no. 4, pp. 561–580, 1992.

[148] A. Borsic, B. M. Graham, A. Adler, and W. R. Lionheart, "In vivo impedance imaging with total variation regularization," *IEEE transactions on medical imaging*, vol. 29, no. 1, pp. 44–54, 2010.

[149] Z. Miao, K. M. Gaynor, J. Wang, Z. Liu, O. Muellerklein, M. S. Norouzzadeh, A. McInturff, R. C. Bowie, R. Nathan, X. Y. Stella, *et al.*, "Insights and approaches using deep learning to classify wildlife," *Scientific reports*, vol. 9, no. 1, pp. 1–9, 2019.

[150] H. H. Do, P. Prasad, A. Maag, and A. Alsadoon, "Deep learning for aspect-based sentiment analysis: A comparative review," *Expert Systems with Applications*, vol. 118, pp. 272–299, 2019.

[151] K. Park, J. Kim, and J. Lee, "Visual field prediction using recurrent neural network," *Scientific reports*, vol. 9, no. 1, pp. 1–12, 2019.

[152] G. H. Lushington, "Breaking the discovery impasse (part 1): A case for deep learning," *Combinatorial chemistry & high throughput screening*, vol. 21, no. 1, pp. 3–4, 2018.

[153] M. Li, S. Lian, F. Wang, Y. Zhou, B. Chen, L. Guan, and Y. Wu, "Prediction model of organic molecular absorption energies based on deep learning trained by chaos-enhanced accelerated evolutionary algorithm," *Scientific reports*, vol. 9, no. 1, pp. 1–9, 2019.

[154] R. Miao, L.-Y. Xia, H.-H. Chen, H.-H. Huang, and Y. Liang, "Improved classification of blood-brain-barrier drugs using deep learning," *Scientific reports*, vol. 9, no. 1, pp. 1–11, 2019.

[155] N.-Q.-K. Le, Q.-T. Ho, and Y.-Y. Ou, "Incorporating deep learning with convolutional neural networks and position specific scoring matrices for identifying electron transport proteins," *Journal of Computational Chemistry*, vol. 38, no. 23, pp. 2000–2006, 2017.

[156] L. Wang, H.-F. Wang, S.-R. Liu, X. Yan, and K.-J. Song, "Predicting protein-protein interactions from matrix-based protein sequence using convolution neural network and feature-selective rotation forest," *Scientific reports*, vol. 9, no. 1, pp. 1–12, 2019.

[157] K. H. Jin, M. T. McCann, E. Froustey, and M. Unser, "Deep convolutional neural network for inverse problems in imaging," *IEEE Transactions on Image Processing*, vol. 26, no. 9, pp. 4509–4522, 2017.

[158] O. Ronneberger, P. Fischer, and T. Brox, "U-net: Convolutional networks for biomedical image segmentation," in *International Conference on Medical image computing and computer-assisted intervention*, Springer, 2015, pp. 234–241.